GROWTH AND CHARACTERIZATION OF Y-BA-CU-O HIGH-T_c SUPERCONDUCTOR THIN FILMS

Thesis by

Jorge A. Kittl

In Partial Fulfillment of the Requirements
for the Degree of
Doctor of Philosophy

California Institute of Technology
Pasadena, California

1991
(submitted May 8, 1991)

to my parents,
my wife, Ale,
and my daughter, Ana.

Acknowledgements

I would like to express my sincere gratitude to my advisor, Professor William L. Johnson, for his continuous support and encouragement.

I am especially grateful to Simon C. W. Nieh for his friendship and valuable collaboration in this work.

I would like to acknowledge the collaboration of Bruce M. Clemens, Carol M. Garland, David S. Lee and Bart Stevens, who contributed to the successful completion of this thesis.

I would like to thank Yoshi Abe, Channing Ahn, Pam Albertson, Gang Bai, Concetto Geremia, Louis Johnson, Elzbieta Kolawa, and Cho-Jen Tsai, who contributed in different ways to this work.

This research was supported by the National Science Foundation, Materials Research Groups, Grant DMR-8811795; the Hughes Research Laboratories, Malibu, California; and a gift from the Ford Motor Company through the Ford Aerospace Division. Part of my financial support was provided by the California Institute of Technology, the ARCS foundation, and by IBM, through fellowships. I am grateful to Carol Mastin for her collaboration with respect to financial aid.

Finally, my recognition and gratitude to my family: my parents, my wife, Alejandra, and my daughter, Ana. Through their continuous support and encouragement, they made this work possible. To them I dedicate this thesis.

Abstract

Two types of growth processes of Y-Ba-Cu-O thin films were investigated: three step processes involving post deposition high temperature anneals, and *in situ* growth processes. Films were deposited by sequential ion beam sputtering from elemental Y, Ba and Cu targets, and characterized by x-ray diffraction, transmission and scanning electron microscopy, energy dispersive x-ray analysis, Rutherford backscattering spectrometry, and low temperature resistivity measurements. In the three step process, multilayers of ~60 Å periodicity were deposited on (001) $SrTiO_3$, annealed in oxygen at 850-900°C, and subsequently at 400-500°C, to obtain the superconducting $YBa_2Cu_3O_{7-\delta}$ phase. The films were epitaxial, predominantly single phase $YBa_2Cu_3O_{7-\delta}$, with different orientations. The nucleation and growth of Y-Ba-Cu-O films deposited on (001) $SrTiO_3$ by magnetron sputtering from separate Y, BaF_2 and Cu sources and grown by a three step process, was investigated by transmission electron microscopy. The *in situ* growth of $YBa_2Cu_3O_{7-\delta}$ films by sequential ion beam sputtering was investigated. The films were deposited following the stacking sequence of $YBa_2Cu_3O_{7-\delta}$, with the individual layer thicknesses nominally equal to one monolayer, at temperatures between 550 and 750°C. O_2 was supplied during growth. Epitaxial, c-axis oriented $YBa_2Cu_3O_{7-\delta}$ films were obtained on MgO and $SrTiO_3$. The correlations between deposition parameters, and structural and electrical properties were investigated. The films had expanded c-axis lattice parameters. The superconducting transition temperatures decreased with the enlargement of the c-lattice parameter. The deposition temperature was the main parameter controlling the lattice expansion. This was later interpreted in terms of the thermally activated dissociation of O_2 at the film surface. We proposed that the expansion of the c-lattice parameter was a consequence of kinetic limitations to the incorporation of oxygen into the films during growth. This led to a consistent description of the results obtained in this work, and results reported in the literature for other *in situ* growth techniques. The films also presented inhomogeneous lattice distortions along the c-direction, that were larger for films with large lattice parameters. The superconducting transitions were broader for films with large inhomogeneous strains. The microstructure of films grown on several substrates (SrTiO3, MgO, SiO_2/Si) under different growth conditions was investigated.

Table of Contents

List of Figures

List of Tables

Chapter 1: Introduction and Background

1.1 Introduction

In April 1986, J.G. Berdnorz and K.A. Muller presented evidence of "possible high Tc superconductivity in the Ba-La-Cu-O system" [Berdnorz and Muller, 1986], and triggered one of the more active scientific research efforts of the decade. An indicator of the overwhelming interest generated by this discovery, was the amount of papers and assistants, and the length of the high-Tc superconductivity sessions in the APS (American Physical Society) and MRS (Materials Research Society) meetings held during 1986 and 1987.

A considerable research effort was directed towards the synthesis of thin films of the high-Tc superconductors, due to their potential applications in electronic devices. A whole set of issues were found centered on the materials aspects, that are crucial to the success of technological applications of the new materials in thin film form. The presence of defect structures that affect the superconducting properties of the films, some of which were not observed in bulk samples, is a fundamental problem that needed to be addressed. Understanding the nature of these defect structures, and learning how to control them, is a necessary step for the successful technological application of thin film high-Tc superconductors. These were the motivations of the present thesis, in which the synthesis of thin films of high-Tc superconductors, the characterization of the defect structures contained in the films, and their relation to superconducting properties, was investigated.

Superconductivity in oxides had been known for nearly 25 years. Superconductivity in TiO and NbO (Tc ~ 1K) [Hulm et al., 1965], and in the perovskite $SrTiO_{3-x}$ (Tc ~ 0.7 K) [Schooley et al., 1964], was discovered in 1964. Superconductivity in oxides with high transition temperatures was found in the spinel phase $LiTi_2O_4$ (Tc ~ 13 K) [Johnston et al., 1973], and in the perovskite-like phase $BaPb_{1-x}Bi_xO_3$ (Tc ~ 13 K) [Sleight et al., 1975]. However, throughout most of their history, these oxide superconductors were merely considered as scientific curiosities. There were always intermetallic compounds with higher transition temperatures, which were considered the materials of choice for technological applications. The discovery of Berdnorz and Muller changed the picture dramatically: the newly discovered superconductor had the highest Tc of any material known at the time. Superconductivity in $La_xSr_{2-x}CuO_4$ with Tc ~ 40 K was reported by several groups [Uchida et al., 1987; Chu et al., 1987; Cava et al., 1987a; Tarascon et al., 1987]. A significant discovery was the superconductor $YBa_2Cu_3O_{7-\delta}$ (the "123" compound), with a critical temperature (Tc ~ 95 K) above the liquefaction temperature of nitrogen [Wu et al., 1987; Cava et al., 1987b]. The existence of a whole class of materials with high transition temperatures became evident, and other systems were investigated. Critical temperatures above 100 K were found in Bismuth and in Thallium based compounds, all of which contained Cu-O planes, and had layered structures.

The "123" phase ($YBa_2Cu_3O_{7-\delta}$) has a layered structure. The unit cell can be pictured as a stacking of three oxygen deficient, perovskite-like cells (Fig. 1). The superconducting and structural properties of this material depend strongly on the oxygen content [Jorgensen et al., 1990; Cava et al., 1990]. For $0 < \delta < 0.2$, the structure is orthorhombic (Fig. 1a), with a Tc ~ 90 K. As oxygen is removed from the structure, the lattice parameters change, the Tc drops, and the oxygen ordering changes. Neutron diffraction studies, show that oxygen is removed from chain sites only (O1 in Fig. 1) [Jorgensen et al., 1987]. This process is reversible, and oxygen can be incorporated or removed easily from the structure at temperatures above 400°C, by simply changing the oxygen partial pressure. For $0.35 < \delta < 0.5$, the Tc has a plateau at approximately 60 K, and the orthorhombicity is smaller than in the fully oxygenated samples. For $\delta > 0.6$, the structure is tetragonal (Fig. 1b), there is disorder in the oxygen sublattices in the basal plane of the unit cell, and the samples are not superconducting. In Fig. 2 we show the lattice parameters, and the superconducting transition temperature, as functions of the oxygen content for $YBa_2Cu_3O_{7-\delta}$. The powder x-ray diffraction data corresponding to the orthorhombic phase is given in table I. The oxygen pressure-temperature diagram of this system was also a subject of intense research. The "123" structure was shown to be thermodynamically unstable at high temperatures and low oxygen pressures [Bormann and Nolting, 1989]. In Fig. 3 we show the features of

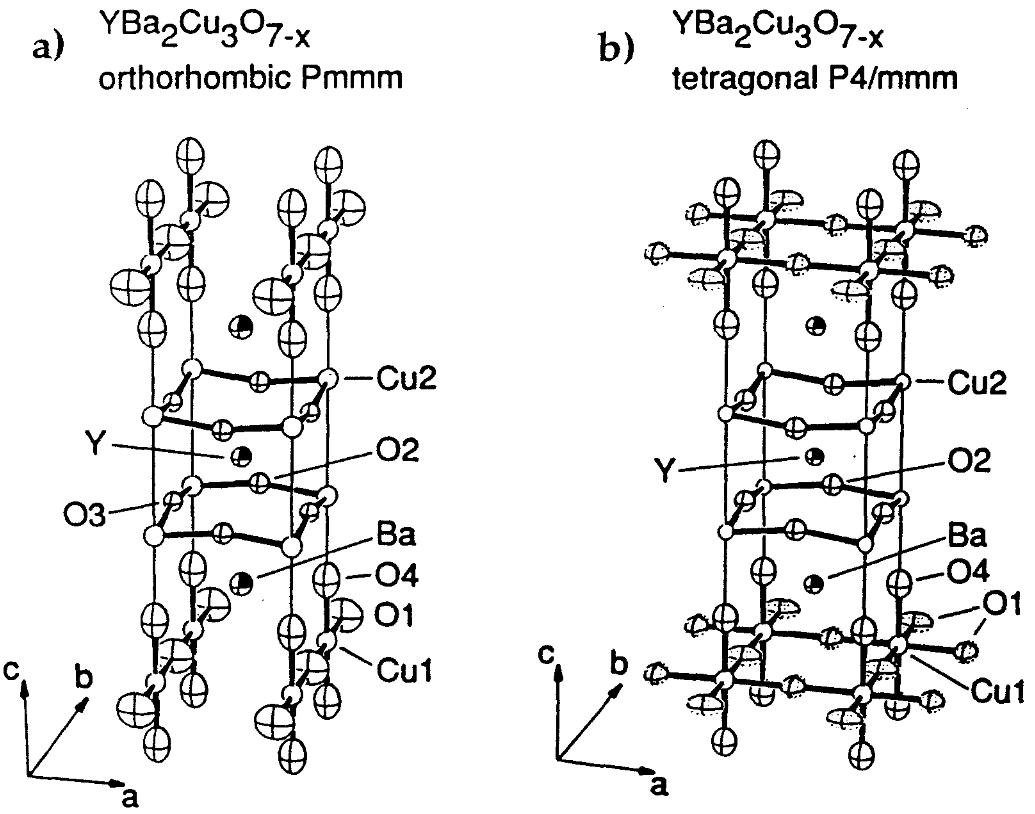

Fig. 1. Orthorhombic (a) and tetragonal (b) structures of $YBa_2Cu_3O_{7-\delta}$. (After Jorgensen et al., 1987).

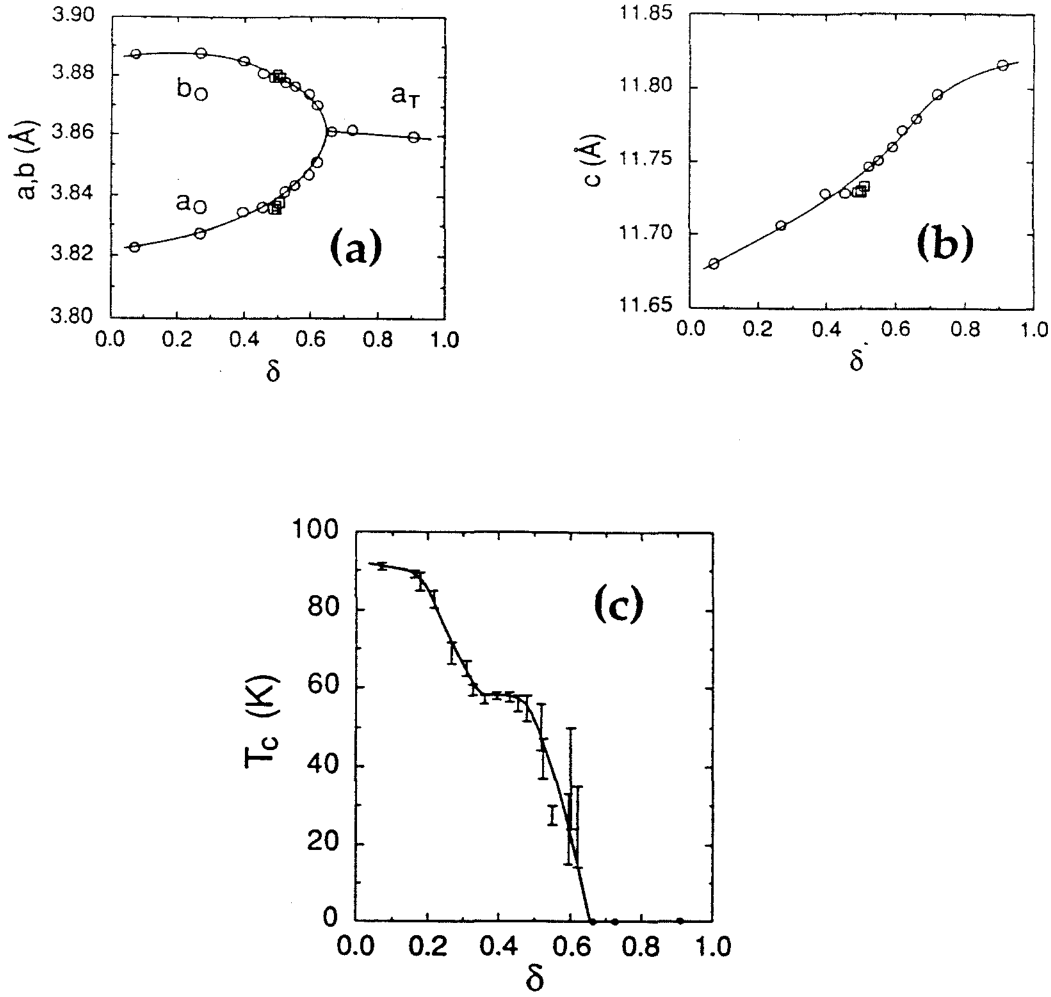

Fig. 2. Dependence on oxygen content δ, of (a) lattice parameters, a_o and b_o in the orthorhombic phase, and a_T in the tetragonal phase, (b) c-axis lattice parameter, and (c) superconducting transition temperature, of $YBa_2Cu_3O_{7-\delta}$. (After Jorgensen et al., 1990).

Table I. Powder x-ray diffraction data of $YBa_2Cu_3O_{6.9}$. Orthorhombic unit cell, a=3.8218 Å, b=3.8913 Å, c=11.677 Å (After Cava et al., 1987).

h	*k*	*l*	d (Å)	I/I_o (%)
0	0	2	5.844	2
0	0	3	3.893	11
1	0	0	3.822	3
0	1	2	3.235	3
1	0	2	3.198	5
0	1	3	2.750	60
1	0	3	2.726	100
1	1	0		
1	1	1	2.653	2
1	1	2	2.469	3
0	0	5	2.336	11
1	0	4	2.321	3
1	1	3	2.232	13
0	2	0	1.946	23
0	0	6		
2	0	0	1.911	10
1	1	5	1.775	3
0	1	6	1.741	2
0	2	3		
1	0	6	1.734	2
1	2	0		
2	0	3	1.716	2
2	1	0		
1	2	1		
1	2	2	1.662	1
1	2	3	1.584	24
1	1	6		
2	1	3	1.569	11

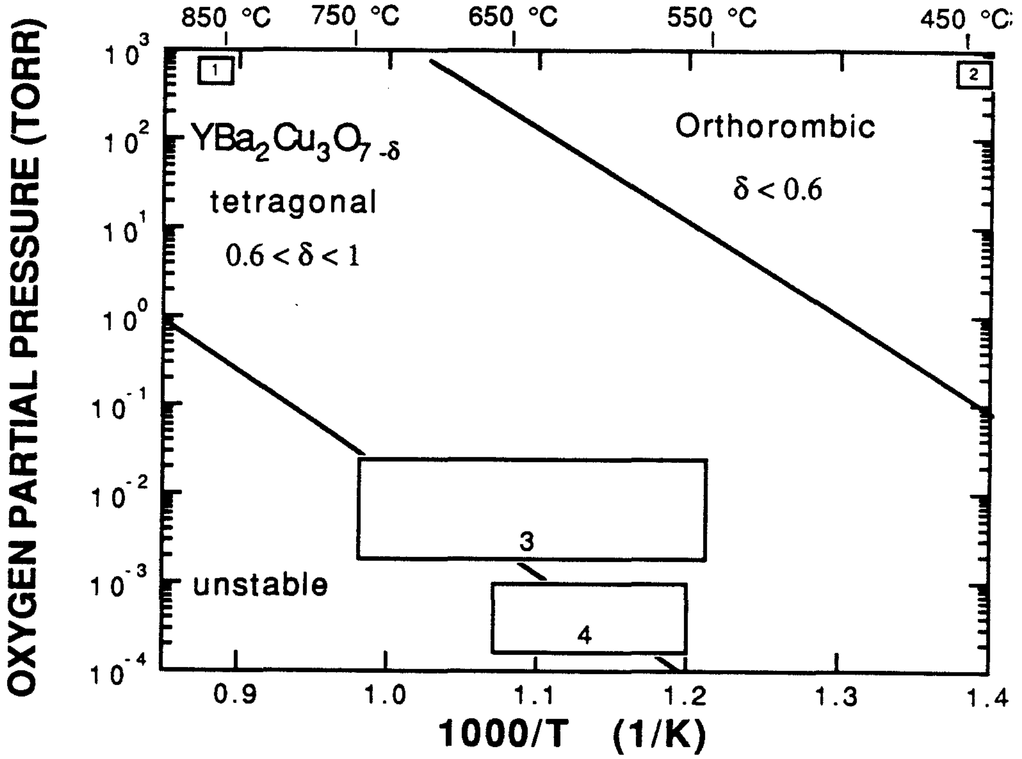

Fig. 3. Oxygen Pressure--Temperature phase diagram of $YBa_2Cu_3O_{7-\delta}$, showing the stability line [Beyers and Ahn, 1991] and the boundary between the orthorhombic and tetragonal phases [Jorgensen et al., 1990]. The regions corresponding to processing conditions used in this work are indicated: (1) growth of $YBa_2Cu_3O_{7-\delta}$ in three step process, (2) low temperature oxygen anneal in three step process, (3) *in situ* growth of $YBa_2Cu_3O_{7-\delta}$ under enhanced local O_2 pressure, (4) *in situ* growth of $YBa_2Cu_3O_{7-\delta}$ under controlled background O_2 pressure.

this diagram that are relevant to the growth of thin films. The stability line corresponds to the data of Beyers and Ahn [Beyers and Ahn, 1991], and the orthorhombic to tetragonal transition line to the data of Jorgensen et al. [Jorgensen et al., 1990]. The "123" compound is not the only superconducting phase in the Y-Ba-Cu-O system. As is common for high-Tc superconductors, there is a related structure (differs from "123" by an alteration in the stacking sequence), that exhibits superconductivity: $YBa_2Cu_4O_8$ (the "248" phase) [Marshall et al., 1988]. The unit cell of the "248" phase can be thought of as a stacking of two "123" unit cells, with an extra Cu-O layer in between.

The synthesis of thin films of the high-Tc superconductors was a field of intense research, due to their many potential applications in electronic devices. Most of the efforts were focused on the "123" compound. The synthesis of "123" superconducting films was reported by several groups [Chaudhari et al., 1987; Oh et al., 1987; Webb et al., 1987; Char et al., 1987; Dijkkamp et al., 1987]. These techniques used a high temperature post-deposition anneal step to grow the superconducting phase. A short overview of this early work can be found in Physics Today [Hammond, 1988].

There are currently two groups of techniques that are used to grow high-Tc superconducting films:

a) Three step processes,

b) *In situ* growth processes.

In the three step processes, a film with the correct metal stoichiometry is deposited at low substrate temperatures, resulting generally in an amorphous structure. Oxygen can be supplied during deposition, but is not essential. The film is then annealed typically for 1/2 to 1 hour in 1 atm of oxygen, at a temperature between 850 and 900°C, to grow the crystalline phase. As shown in Fig. 3, the films are tetragonal at these processing conditions. To obtain a superconducting film, further oxygen has to be incorporated into the structure. This is typically done by annealing the film in 1 atm of oxygen for 1/2 hour at ~ 400-450°C. The high processing temperature involved in three step processes, restricts the types of substrates that can be used. Typical substrates used in three step processes are $SrTiO_3$ and $LaAlO_3$, which are also well lattice-matched to the "123" structure, allowing epitaxial growth.

In the second type of processes, the *in situ* growth techniques, the crystalline "123" structure is grown as the film is deposited. The substrate temperatures during deposition ranges typically from 550 to 800°C, and the oxygen pressures from 10^{-4} to 10^{-1} Torr (Fig. 3). The films obtained have the tetragonal, oxygen deficient structure. A second step is needed to increase the oxygen content of the films. This is done either *in situ*, by increasing the oxygen pressure in the deposition chamber during cool-down, or in a *ex situ* low temperature anneal in oxygen (typically 1/2 hour at 400°C in 1 atm of oxygen).

1.2 Superconductivity and Material Properties

Although superconductivity was discovered in 1911 [Onnes, 1911], the understanding of its microscopic mechanism was only achieved in 1957 with the BCS theory [Bardeen et al., 1957]. The full development of the microscopic theory resulted in the demonstration of the phonon-mediated electron pairing mechanism as responsible for the superconducting properties in conventional superconductors [Eliashberg, 1960; Mc Millan and Rowell, 1965]. However, the discovery of the high-Tc superconductors promoted the investigation of alternative mechanisms for superconductivity, mainly because their high transition temperatures are difficult to account for in the frame of the conventional theories. The microscopic origin of superconductivity in the new materials is not yet fully understood. However, many of the aspects of superconductors that are important for technological applications, are well described, both for high-Tc and for conventional superconductors, by the phenomenological Ginzburg-Landau theory [Ginzburg and Landau, 1950]. This theory is particularly successful in describing the properties of superconductors under spatially non uniform fields, including non linear effects in fields that are strong enough to change the superconducting carrier density. The Meissner effect, the existence of two classes of superconducting materials (classified according to their response to external magnetic fields): the type I and the type II superconductors, etc., are correctly predicted by this theory [Tinkham, 1975]. Detailed descriptions of the phenomenological aspects of superconductors, the microscopic and the Ginzburg-Landau theories of superconductivity, their consequences, and their applications to numerous problems in superconductivity can be found in the literature [Tinkham, 1975; Schrieffer, 1964]. Here, we are mainly concerned with some aspects of how the materials properties (such as the presence of defect structures), may affect the superconducting properties of a superconductor. A review of this topic can be found in the literature [Johnson, 1983].

In the Ginzburg-Landau theory, the properties of a superconductor are described by a macroscopic, pseudo-wave function $\Psi(\mathbf{r})$, which is introduced as a complex order parameter in the context of the Landau theory of phase transitions. The local density of superconducting electron pairs, $n_s(r)$, is given by $|\Psi(\mathbf{r})|^2$. The theory proposes an expansion of the free energy density in powers of $|\Psi(\mathbf{r})|^2$ and $|\nabla\Psi(\mathbf{r})|^2$. The integral of this free energy density over the volume of the superconductor is minimized by applying a variational principle, to obtain a pair of coupled differential equations for $\Psi(\mathbf{r})$ and the vector potential $\mathbf{A}(\mathbf{r})$ ($\mathbf{A}(\mathbf{r})$ is the vector potential as conventionally defined in electromagnetism, with $\nabla\times A = \mathbf{B}$, where $\mathbf{B}$ is the magnetic field). The Ginzburg-Landau differential equations can be written

$$\alpha\Psi + \beta|\Psi|^2\Psi + \frac{1}{2m^*}\left(\frac{h}{2\pi i}\nabla - \frac{e^*}{c}\mathbf{A}\right)^2\Psi = 0 \tag{1.2.1}$$

$$J_s = \frac{e^*}{4\pi m^* i}\left(\Psi^*\nabla\Psi - \Psi\nabla\Psi^*\right) - \frac{e^{*2}}{m^* c}\Psi^*\Psi\,\mathbf{A} \quad , \tag{1.2.2}$$

where $\mathbf{J}_s$ is the superfluid current or supercurrent; α and β are coefficients introduced phenomenologically, that depend on the temperature (and are specific of a given material); m* and e* are the mass and charge of the superconducting carriers (electron pairs), *h* is Planck's constant, and *c* is the speed of light. An important result that is deduced from these equations is the spatial scale of variations of the order parameter, given by the temperature dependent coherent length

$$\xi(T) = \xi\left(\frac{Tc - T}{Tc}\right)^{-1/2} \quad , \tag{1.2.3}$$

where $\xi = 0.74\,\xi_o$ in the clean limit (when scattering of electrons in the normal state is weak, as in a pure metal), ξ_o is the coherence length of the electron pairs (size of the electron pairs); $\xi = 0.85\,(\xi_o\, l\,)^{1/2}$ in the dirty limit (when scattering of electrons in the normal state is strong, as in disordered alloys), and l is the electron mean free path.

A fundamental issue in the high-Tc superconductors is their short coherence lengths. In $YBa_2Cu_3O_{7-\delta}$, the coherence lengths are $\xi_o \sim 4.3$ Å along the c-direction, and $\xi_o \sim 31$ Å in the a-b plane [Dinger et al., 1987]. The characteristic length of variation of the density of superconducting carriers is as a consequence on the order of 10 Å. This means that the superconducting properties of these materials are very sensitive to defects, even in such short length scales. The defect structures play a fundamental roll in determining the superconducting properties of $YBa_2Cu_3O_{7-\delta}$.

As described in the previous section, oxygen vacancies in the chain sites affect strongly the superconducting transition temperature of $YBa_2Cu_3O_{7-\delta}$, mainly by altering the carrier density in the Cu-O planes [Cava et al., 1990]. The presence of point defects, stacking faults, strains, second phases, grain boundaries, etc., affect the properties of a superconductor in different ways. The presence of defect structures may lower the Tc, broaden the superconducting transition, but may also result in higher critical current densities (current density above which the sample is not longer superconducting), by acting as pinning centers.

The transport properties of $YBa_2Cu_3O_{7-\delta}$ are degraded at grain boundaries. The critical current across a grain boundary decreases for increasing misorientation angle of the grain boundary [Dimos et al., 1988]. The grain boundaries exhibit weak link behavior, and have been used as junctions in superconducting quantum interference devices (SQUID) [Gross et al., 1990]. These results show that the grain structure of a superconductor is a key issue, since it strongly affects the transport properties. This is particularly important in thin films, in which percolation is more difficult than in bulk samples.

The grain structure of a film is strongly influenced by the substrate on which the film is grown. When a crystalline phase in the film grows from an amorphous matrix, the substrate catalyses the nucleation of the crystalline phase, if the free energy of the crystal-substrate interface is lower than that of the crystal-glass interface [Haasen, 1986]. In this case, nucleation at the film-substrate interface may dominate over nucleation in the bulk of the film. If the crystalline phase nucleates and grows as the film is deposited, different types of growth modes are possible; such as two dimensional layer by layer growth, three dimensional island growth, and Stranski-Krastanov growth (island on top of a few layers of two dimensional growth mode) [Jesser and van der Merwe, 1989]. In equilibrium, the type of growth mode is determined by the relation between the film-substrate interfacial free energy, and the film and substrate surface free energies. An important issue in the nucleation of a crystalline film on a crystalline substrate is the possibility of atomic matching across the interface. The substrate-crystal (film) interfacial free energy, plays an important roll in determining the orientation relation of crystals that nucleate at the film-substrate interface [Doherty, 1983]. When a crystalline film is grown on a single crystal substrate, the grains that nucleate at the film-substrate interface may have specific orientations for which the interfacial energy is low. We are interested in the interface between two different phases (heterophase interfaces), that have different structures (heterostructure interfaces). The interfacial free energy between two crystals depends on crystal structure, orientation, lattice mismatch, surface chemistry, etc. As a first approach, we consider a geometrical model, that proposes that the interfacial free energy between two crystals have minima at relative orientations in which the extensions of the lattices corresponding to both crystals have a high density of coincidence or near coincidence sites (Near coincidence site lattice theory) [Bishop and Chalmers, 1968; Balluffi et al., 1982]. This leads to the concept of lattice mismatch between two structures, for a given orientation relation. The sites of near coincidence, form a lattice, which is slightly different for the two structures. The lattice mismatch parameters, are the percentage differences between the lattice parameters of the near coincidence site lattices of the two crystals. Qualitatively, the orientation relations that have a high density of near coincidence sites and low lattice mismatch, have low interfacial free energies. Crystalline grains in the film tend to nucleate at the film-substrate interface with these special orientations. These simple geometrical considerations cannot account for all the types of orientation relations observed in epitaxial films. For example, in the case of the Nishiyama-Wasserman [Nishiyama, 1934; Wasserman, 1933] and the Kurdjumov-Sachs [Kurdjumov and Sachs, 1930] orientations between (111) f.c.c. and (110) b.c.c. film-substrate pairs, the matching corresponds to rows of atoms rather than to sites on a lattice [van der Merwe, 1982]. Moreover, the crystallographic texture of a film may be developed after the initial nucleation stage, during recrystallization or grain growth [Thompson, 1985].

In this work we will use the term "epitaxial", with the meaning that is commonly used in the literature of high-Tc superconducting thin films, i.e., defining an epitaxial thin film as one in which the grains in the film have special orientation relations with respect to the substrate. An important concept related to the structure of the interface between an epitaxial film and the substrate, is the one of structural coherence across the interface [Gleiter, 1983]. When there is a small lattice mismatch between two structures, it might be energetically favorable to strain one or both of them so that there is a perfect coincidence of lattice planes across the interface. The two structures may adjust to have the same lattice parameters in the plane parallel to the interface. This is the case of a perfectly coherent interface. This would result in a low interfacial free energy, however, at the cost of increasing the volume free energy of the bulk of the crystals. The change in the volume free energy due to coherency strains, increases with the thickness of the corresponding crystal. For this reason, in the case of a thin film deposited in a thick substrate, the film rather than the substrate may be strained. There are other ways of accommodating the misfit between substrate and film, such as relaxing the misfit strains by introducing misfit dislocations at the interface [Jesser and van der Merwe, 1989], resulting in a semi-coherent interface. In equilibrium, the structure of the interface, and the strain fields are such that the total free energy is minimized. Several models have been developed to describe the configurations of the interface and strain fields [Dregia et al., 1987; Jesser and van der Merwe, 1989]. In general, a transition from a coherent (strained) configuration to a semi-coherent configuration is predicted, by this models, at a critical thickness. More generally, the kinetic barriers to the relaxation of the misfit strain, have to be considered when determining the critical thickness [Jesser and van der Merwe, 1989].

There are other type of substrate induced strains, besides the coherency strains described. Crystalline films are generally grown at elevated substrate temperatures. The values of other growth variables may also differ from their values at normal conditions (room temperature, atmospheric pressure). When the sample is taken to normal conditions, there are changes in the lattice parameters of both the film and the substrate due to thermal expansion, etc. If the coefficients of linear thermal expansion are different for the substrate and film, there may be strains introduced during cool down.

In the case of $YBa_2Cu_3O_{7-\delta}$, the lattice parameters depend on the temperature and on the partial pressure of oxygen. The change in lattice parameters between two points in the temperature-oxygen pressure diagram has two contributions: one given by the thermal expansion coefficient, and one given by the change in oxygen content. The dependence of the lattice parameters on the oxygen content is given in Fig. 2. The oxygen content at different oxygen pressure-temperature conditions can be estimated for some cases from the data in Fig. 3. The coefficients of linear thermal expansion of $YBa_2Cu_3O_{7-\delta}$ along the different directions are given in table II, together with those of MgO and $SrTiO_3$. In table III, we give estimated values of the lattice parameters of $YBa_2Cu_3O_{7-\delta}$, $SrTiO_3$, and MgO at several processing conditions. The lattice mismatch at the growth conditions is the relevant quantity in determining the issues of epitaxy and orientation relations between film and substrate.

Table II. Coefficients of linear thermal expansion of $YBa_2Cu_3O_7$ [Jorgensen et al., 1987], $SrTiO_3$ [Brown et al., 1990], and MgO [Gray, 1963].

Phase		$10^6\alpha = \frac{10^6}{l}\frac{\Delta l}{\Delta T}$ (1/°C)
$YBa_2Cu_3O_7$	c-direction	21
	a-direction	11
$SrTiO_3$		11
MgO	0°C	9.8
	200°C	12.7
	400°C	13.7
	600°C	14.2

Table III. Lattice parameters of $YBa_2Cu_3O_{7-\delta}$, $SrTiO_3$, and MgO, at several temperatures and oxygen pressures.

T (°C)	P_{O_2}(Torr)	$YBa_2Cu_3O_{7-\delta}$			$SrTiO_3$	MgO
		a (Å)	b (Å)	c (Å)	a (Å)	a (Å)
25	760	3.82	3.89	11.68	3.905	4.203
600	760	3.855	3.918	11.83	3.930	4.24
600	4×10^{-4}	3.88	3.88	11.98		
700	8×10^{-3}	3.885	3.885	12.00	3.934	
800	760	3.90	3.90	11.94	3.938	4.25

1.3 Summary

In this work, we investigated the synthesis of Y-Ba-Cu-O thin films, and characterized their structural and superconducting properties by various techniques.

We investigated the growth of $YBa_2Cu_3O_{7-\delta}$ thin films by a sequential ion beam sputtering technique. We studied both a three step process and an *in situ* process. The motivation to develop a sequential deposition technique resides in the naturally layered structure of all the high-Tc superconductors, and in the possibility of synthesizing artificially layered structures. The ion beam sputtering technique allows an excellent control of the layer thicknesses due to the stability of the broad-beam ion sources, and the independence between the plasma generation process (inside the ion-source) and the sputtering process. We have demonstrated the growth of superconducting "123" films by the three step process and by *in situ* growth. We investigated the correlations between the deposition and processing parameters, and the structural and electrical properties of the films. The composition of the films was determined by Rutherford backscattering spectrometry and energy dispersive x-ray analysis. X-ray diffraction was used for phase identification, in the determination of crystal orientation, in the determination of lattice parameters, and in the analysis of inhomogeneous strains. Transmission electron microscopy was used to study the microstructure of the films, the issue of epitaxy, the substrate-film orientation relations, the presence of precipitates of second phases, and the presence of extended defects such as stacking faults. Scanning electron microscopy and optical microscopy were used to study the surface morphologies of the films. The superconducting properties were studied by low temperature resistivity measurements.

We also characterized films grown by magnetron sputtering at Hughes Research Laboratories. We studied the nucleation and growth of the $YBa_2Cu_3O_{7-\delta}$ ("123") and $YBa_2Cu_4O_8$ ("248") phases by transmission electron microscopy. The films were deposited from separate Y, BaF_2 and Cu targets, and grown by a three step process. The presence of fluorine in the as deposited films stabilized the $YBa_2Cu_4O_8$ phase. We found that the "248" was the first phase to nucleate epitaxially at the film-substrate interface, and that it nucleated with c-axis orientation (c-axis normal to the substrate surface). We found that the films had "123" grains with c-axis normal to the substrate surface and c-axis in plane epitaxial orientations. We observed very rough film surface morphologies, and suggested that this was a consequence of the anisotropy of crystal growth rate. The growth rate is slower along the c-direction, so that c-axis oriented grains tend to be flat and thin, in contrast to grains with the c-axis in-plane, that grow fast in the direction normal to the substrate, and protrude from the film surface. We also observed the presence of a reacted layer at the film-substrate interface, which we attributed to the high processing temperature involved.

We developed an in situ growth technique in which the c-axis orientation is favored, by depositing the film following the stacking sequence of the "123" phase with the individual layer thicknesses nominally equal to one monolayer. Films were grown on (001) $SrTiO_3$, (001) MgO and SiO_2/Si substrates. We showed the advantages of this type of process with respect to the three step process. The samples exhibited sharp substrate-film interfaces, due to the low processing temperatures. The films were predominantly c-axis oriented, and had smoother surfaces than the films grown by three step processes. X-ray analysis showed that the films contained both homogeneous and inhomogeneous strains along the c-direction, which were correlated to the superconducting transition properties (Tc and width). The films had expanded c-axis lattice parameters, and the transition temperatures decreased with the enlargement of the c-lattice parameter. This phenomenon was shown to be of a different nature than the c-lattice expansion and decrease in Tc associated with chain-site oxygen vacancies. We found that under the conditions investigated, the growth temperature was the main parameter controlling the c-axis lattice expansion. An analysis of these results, and those obtained for other *in situ* growth techniques, suggested that the expansion of the c-axis lattice parameter is caused by kinetic limitations to the incorporation of oxygen to the film during growth.

We investigated the microstructure of the films by transmission electron microscopy, and determined that films grown on single crystal MgO and $SrTiO_3$ substrates were epitaxial. We investigated the orientation relations between "123" grains and the substrate. In all the cases of epitaxial films studied in this work, the interfaces were semi-coherent. The films were relaxed, having a different in-plane lattice parameter than the substrate. This was inferred from the observation of Moire patterns in plan-view transmission electron microscopy .

We also analyzed films grown *in situ* by magnetron sputtering at Hughes Research Laboratories. The films had expanded c-axis lattice parameters. The oxygen content was investigated by Rutherford backscattering spectrometry, using the oxygen resonance to enhance the sensitivity of the measurement. The presence of point defects, in particular the chemical order in the Y and Ba sublattices, was studied by rocking curve x-ray analysis.

In Chapter 2 the different experimental techniques used in this work are introduced, and the sequential ion beam sputtering deposition process is described. In Chapters 3 and 4 we present the results obtained by three step processes and *in situ* growth processes respectively.

Chapter 2: Experimental Setup and Techniques

2.1 UHV Ion Beam Sputtering and X-Ray Diffraction System

The deposition and x-ray characterization of films described in this work was carried out in an Ultra High Vacuum system (Fig. 4). The system consists of three chambers: a deposition chamber, a loading chamber and an x-ray chamber. Three pumps are used to achieve the vacuum environment: a roughing pump, a turbomolecular pump and a He closed-cycle cryogenic pump. The roughing pump and the turbomolecular pump are connected to all the chambers, and the cryogenic pump inlet is connected to the deposition chamber. A system of valves allows the isolation of the different chambers and pumping lines. Three gauges are used to monitor the pressure in the system: two ion gauges, one in the deposition chamber and one in the x-ray chamber, and a thermistor gauge in the loading chamber. The deposition chamber is in the form of a hemisphere with a 6 inch radius. The pumping speed of the cryogenic pump is 1500 l/s. Typical base pressures are 5×10^{-9} Torr in the deposition chamber and 1×10^{-7} Torr in the x-ray chamber.

Samples and targets are mounted in holders that can be transferred among the different chambers by means of two transfer arms. The use of a loading chamber allows the introduction or removal of targets and

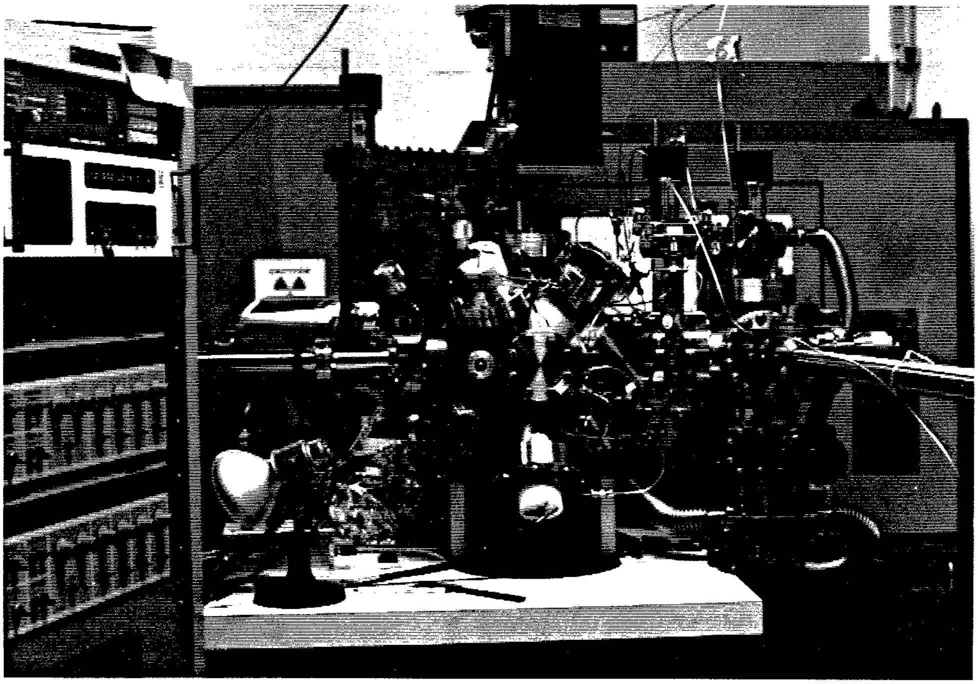

Fig. 4. Picture of the UHV ion beam sputtering and x-ray diffraction system.

samples from the system without breaking the vacuum in the deposition and x-ray chambers.

The x-ray chamber is integrated to a Siemens D500 diffractometer allowing the x-ray analysis of samples in a vacuum environment. A Be window is used to allow the x-ray beam in and out of the vacuum chamber. Further description of the x-ray diffractometer is given in section 2.5.

The films are grown in the deposition chamber by sequential ion-beam sputtering, using Kaufman type broad beam ion sources. A brief description of the Kaufman type ion source is given in section 2.2, an overview of the concepts involved in physical sputtering deposition is given in section 2.3, and a description of the configuration of the deposition chamber and implementation of the sequential deposition process is given in section 2.4.

2.2 Broad Beam Ion Sources

In this work, Kaufman type broad beam ion sources were used for sputtering and for ion assisted deposition. Detailed descriptions of this type of ion sources and their applications can be found in the literature

[Kaufman, 1974, 1978, 1984; Kaufman and Robinson, 1982a; Kaufman et al., 1982b; Harper et al. 1981, 1982]. Here, only a brief description of the processes involved in the operation of a broad beam ion source is given, and illustrated in Fig. 5.

Neutral atoms or molecules of the working gas (Ar or O_2 in this work) are introduced to the discharge chamber of the ion source through the gas inlet. These neutrals undergo collisions with energetic electrons emitted by the cathode (thermionic emitter), producing positive ions. As a consequence, a plasma is produced in the discharge chamber, constituted by ions, energetic electrons and low energy background electrons. In ion sources that use double grid optics, ions from the plasma reach the holes in the screen grid and go through them forming beamlets. These beamlets are accelerated by the negative accelerator grid, and go through the holes in it without striking the grid due to the alignment of the holes of the screen and accelerator grids. The sum of these individual beamlets constitutes the broad ion beam.

The anode is held at a positive potential with respect to ground, V_b. The walls of the discharge chamber are held at the anode potential or floating, and the screen grid is floating. The plasma in the discharge chamber is approximately (within 1-5 eV) at anode potential. Since the targets are at ground potential, the beam energy is given by the anode potential, and is typically in the range of 100 to 1500 eV. The accelerator grid is negatively biased with respect to ground, by the accelerator

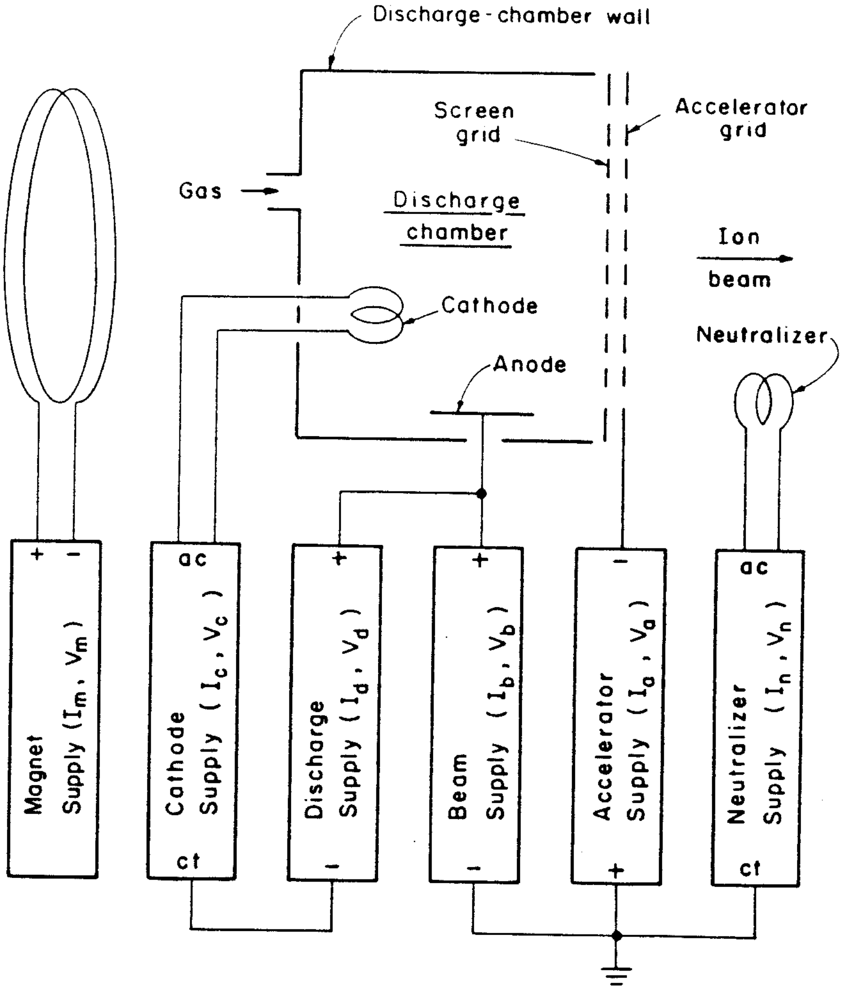

Fig. 5. Typical broad beam ion source with power supplies. (After Kaufman, 1984).

potential, V_a, typically ~ 150 V, to prevent electrons at ground potential outside the ion source from penetrating into the discharge chamber (since this electron flow would impede an accurate determination of the ion beam current). As the beam leaves the ion source, it is neutralized by electrons from an electron source at ground potential. This could be a neutralizer filament (thermionic emitter), or simply secondary electrons from a conducting target. Electrons and ions do not recombine in the beam but flow independently. The typical variation of potential through the double grid optics is indicated in Fig. 6.

The cathode is held at a negative potential with respect to the anode, the discharge potential, V_d, typically ~ 40 V. The discharge potential determines the energy of the ionizing electrons. This energy has to be smaller than the addition of the first and second ionization potentials of the working gas, to prevent double ionization (since this would result in a beam with particles at two energies: $e \times V_b$ and $2e \times V_b$). For Ar, the first ionization potential is 15.8 eV and the second ionization potential is 27.6 eV, so that the discharge potential has to be kept below 43.4 eV. In small ion-sources, (1-3 cm), multiple-step ionization processes are negligible, since the mean free path for an ion between collisions with energetic electrons is substantially larger than the discharge chamber dimensions.

As mentioned above, thermionic emitters are used for the cathode and sometimes for the neutralizing functions. Alternating current supplies are used to heat up the filaments. The cathode heating current, I_c,

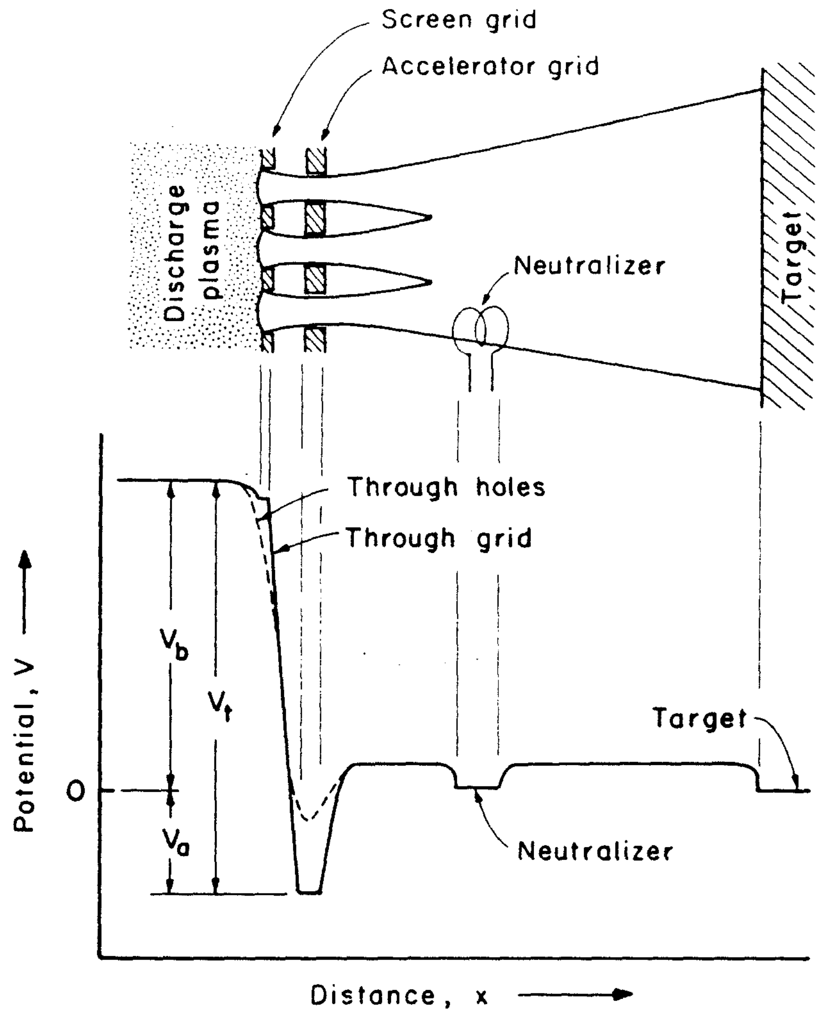

Fig. 6. Variation of potential through ion optics. (After Kaufman, 1984).

is a very sensitive control of the ion beam current. It determines the cathode filament temperature, which in turn controls the emission of ionizing electrons, determining as a consequence the density of ions in the plasma at a given operating pressure. A good thermionic emitter material has a high melting point and a low work function. A typical choice is tungsten. For oxidizing working gases, a reasonable choice is thoria-coated iridium, in which the thoria-coating provides the low work function and iridium the high melting point [Guarnieri et al., 1988]. This combination is very stable in oxygen. This turns out to be important in the present application since oxygen is frequently present in the carrier gas.

To improve the efficiency of the ionizing electrons, a magnetic field is used to confine the energetic electrons and prevent them from reaching the anode or other discharge chamber surfaces. Low energy electrons provide the main contribution to the discharge current flow into the anode.

The ion beam current is given approximately by the beam power supply current, I_b, which includes all the charge flow from the discharge chamber. Part of this current, however, may correspond to ions striking the accelerator grid, which do not contribute to the ion beam. These ions contribute to the accelerator grid current, I_a, which also has contributions from charge-exchange low energy ions outside the ion-source, which are accelerated towards the grid. This results in an uncertainty in determining the exact value of the ion beam current. Under normal operating conditions, however, the accelerator grid current is only a small fraction of the ion beam current.

To understand the current capacity of double grid optics, the Poisson equation is solved for the ideal case of two parallel planes, obtaining Child's Law:

$$j = (4\varepsilon_0 / 9)\,(2q/m)^{1/2}\, V^{3/2} / l^2, \qquad (2.2.1)$$

where q/m is the charge to mass ratio of the accelerated particles, j is the maximum current density between the planes, ε_0 is the permittivity of free space, V is the potential difference between the planes, and l the separation between planes. In double-grid optics, V is given by (V_b+V_a), and l is given by the distance from the edge of a screen grid bar to the center of the corresponding hole in the accelerator grid. The total current capacity is proportional to the total open area of the grids.

At low energies, the current capacity of double grid optics falls as $V^{3/2}$, becoming very low at energies bellow 100 eV. At these energies, higher currents are obtained with single grid optics. In this type of optics, there is no screen grid, and l is given by the thickness of the plasma sheath next to the accelerator grid. The accelerator grid impingement is higher than in double grid optics. This limits the energies at which single grid optics can be used, since higher energies would result in excessive heating of the grid and sputtering of the grid material. In single grid optics, neutralization of the beam can be achieved by secondary electrons from the grid, if the grid is floating.

In double grid optics, focusing or collimation of the beam is easily achieved by specific designs involving the relative positions of the holes in the screen and accelerator grids. In single grid optics the beam is generally divergent.

2.3 Sputtering

When a surface is bombarded by energetic particles, it is eroded and material from the surface is ejected. This process is known as "sputtering." Other processes are also present when energetic particles bombard a surface, such as backscattering as well as trapping and reemission of incident particles, desorption of surface layers, emission of electrons and photons, and changes in the surface structure and topography. The mechanisms and characterization of the sputtering process and its dependence on parameters such as incident particle mass, energy and angle, target composition, etc., have been studied in detail. Reviews on this topic can be found in the literature [Behrisch, 1981; Maissel, 1970; Wehner, 1970]. Here, only a brief account of the main characteristics of sputtering is given.

The sputtering process can be characterized by the sputtering yield, Y, defined as the number of atoms removed from the surface of a solid per incident particle:

$$Y = \frac{\text{atoms removed}}{\text{incident particle}} . \tag{2.3.1}$$

A more detailed characterization of the sputtering process is obtained by considering the differential sputtering yields. In these, the ejected particles are distinguished by their mass, charge, excitation state, energy and angle of ejection. As an example, the total yield is given by the contributions from ejected particles with different masses, M_1, and charges, q_1:

$$Y = \sum_{M_1,q_1} Y_{M_1,q_1} . \tag{2.3.2}$$

When considering the angular distribution of the ejected particles, the differential yield of particles ejected into a solid angle $d\,^2\Omega_1$, at an exit angle (θ_1 , ϕ_1), is given by:

$$\frac{\partial^2 Y}{\partial^2 \Omega_1}(\theta_1,\phi_1) = \frac{\text{atoms ejected into } d^2\Omega_1}{\text{incident particle}} , \tag{2.3.3}$$

and considering the energy of the ejected particles E_1, the corresponding differential sputtering yield is given by:

$$\frac{\partial Y}{\partial E_1}(E_1) = \frac{\text{atoms removed with energies in } (E_1, E_1 + dE_1)}{\text{incident particle}} \; . \tag{2.3.4}$$

In general, an incoming particle will collide transfering energy to atoms in the target. When the energy transferred to an atom is higher than the binding energy, a recoil atom is generated. These recoil atoms in turn collide against other atoms in the target transfering energy to them. The elastic collision processes are the most important. Roughly speaking, when an atom in the vicinity of the target surface has a translational kinetic energy component normal to the surface larger than the surface binding energy, the atom is sputtered.

There are qualitatively three different situations:

a) The single knockon regime in which recoil atoms from ion-target atom collisions receive sufficient energy to be sputtered but not to generate a collision cascade.

b) The linear cascade regime in which recoil cascades are generated, but in which the density of moving atoms in the cascade is much lower than the density of atoms in the target.

c) The spike regime in which the density of atoms in the cascade is so high that in a certain volume (the spike volume), most of the atoms are in motion.

The sputtering conditions used in the present work (Ar^+ ions at energies between 180 eV and 1 keV) correspond to the linear collision cascade regime or the thermal spike regime.

Under these conditions, the distribution of sputtered particles follows roughly a cosine law :

$$\frac{\partial^2 Y}{\partial^2 \Omega_1} \sim \cos \theta_1 , \tag{2.3.5}$$

where θ_1 is the angle between the direction of ejection of the particle and the target normal.

The majority of the sputtered particles are neutral atoms ($\geq 95\%$), with an energy distribution centered roughly around the surface binding energy of the target U_o, which is typically ~ 1-10 eV.

The sputtering yield depends on the angle of incidence of the projectile θ_o, increasing from normal to grazing incidence until a maximum at typically ~ 80°, and falling down as θ_o approaches 90°. The sputtering yield also depends on the incident ion mass, and energy (E_o). No sputtering occurs at energies below a threshold energy E_{th}, which is simply related to the surface binding energy. The sputtering yield increases with energy up to a maximum (> 1 keV). At higher energies, the yield decreases due to the longer ranges of the ions in the target, which results in cascades developing too deep inside the material. Other factors that determine the sputtering yield are the substrate material, crystal structure and surface morphology. In single crystals, the yield depends on the crystal orientation, and channeling effects are observed. The yield does not depend strongly on the target temperature, up to nearly the melting point. When sputtering in a reactive environment, the sputtering yield is affected by the formation of layers of reacted material at the target surface. As examples of the order of magnitude of sputtering yields, the yield for Ar^+ ions incident on a Cu target is 1 at E_0=200 eV, and 3 at E_0=1 keV.

2.4 Growth of Y-Ba-Cu-O Thin Films: Sequential Deposition Process

The configuration of the deposition chamber is illustrated in Fig. 7. Two ion sources are used: a sputtering ion source and a substrate-bombardment ion source. The substrate-bombardment ion source is used in ion assisted deposition, or for substrate cleaning. Both ion sources are Kaufman type, and have 3 cm diameter extraction optics.

The sputtering ion source has double grid optics which produce a collimated beam. The distance between the sputtering ion source and the target is 6.5 cm. An aperture situated in front of the source at 2.5 cm is used

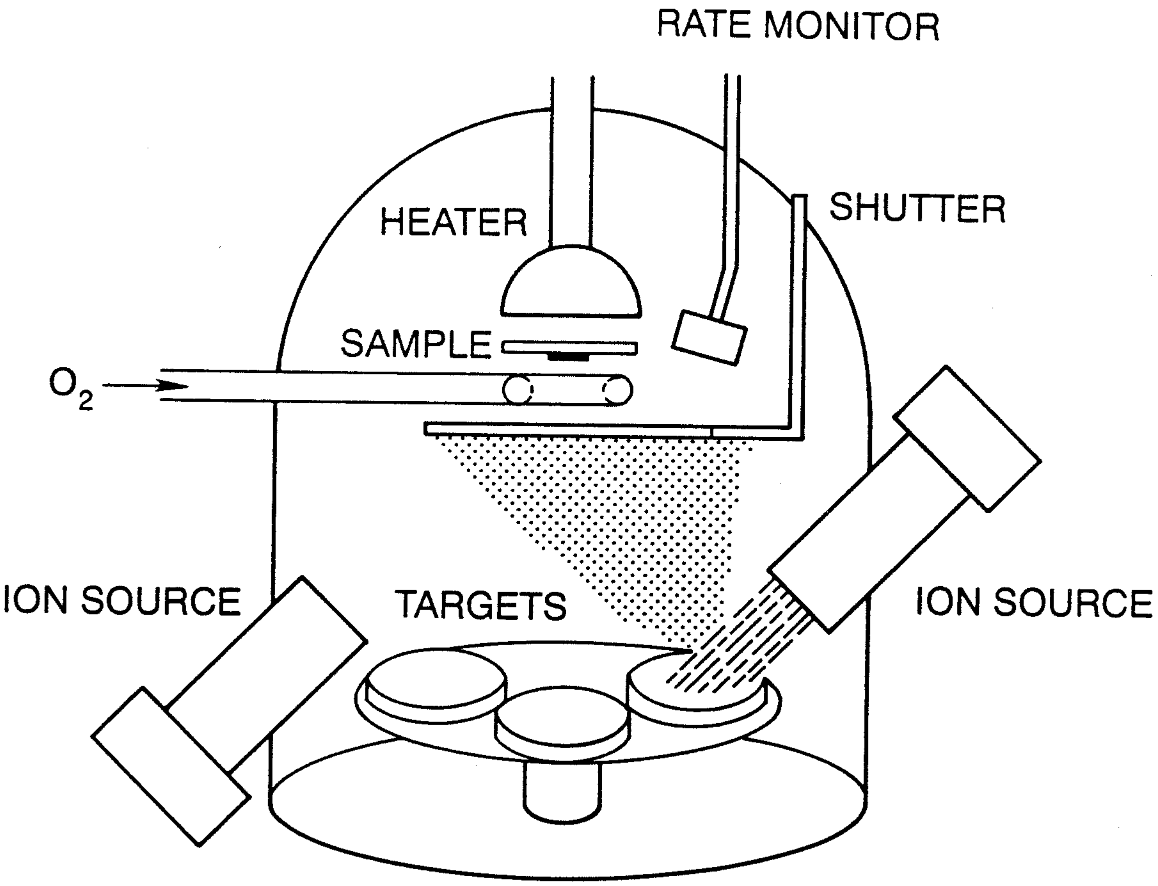

Fig. 7. Schematic drawing of the deposition chamber.

to restrict the beam and reduce the amount of stray ions, to ensure that only target material is sputtered. The aperture is made of Cu, and designed to produce a circular, 3 cm diameter bombardment area on the target. A knife edge geometry is used for the aperture, to avoid forward sputtering of the aperture material.

The sputtering targets are placed in a carousel. The carousel holds up to four 2 inch diameter targets. Target selection is servo-controlled through the use of a stepping motor that rotates the carousel. The targets are mounted on Cu transfer-holders which can be transferred under vacuum to the other chambers of the UHV system using two transfer arms. The carousel has divisions which prevent material sputtered from one target to contaminate the other targets. The angle of incidence of the ion beam for horizontally mounted targets is 45°. In some cases, Cu wedges were used as spacers between the holders and targets, resulting in angles of incidence of the ion beam closer to the target surface normal. These spacers were used to increase the region of the substrate stage that is exposed to the substrate-bombardment ion beam, which is partially blocked by the carousel.

A quartz tungsten-halogen lamp was chosen as substrate heater, in order to have substrate heating compatible with the transfer mechanism and with an oxygen environment. The substrate is clamped on a small Cu plate (0.8 cm × 0.8 cm × 0.08 cm), which is mounted on a 2 inch diameter transfer-holder. The transfer-holder has a 1 inch diameter hole in the middle to allow radiation heating of the Cu plate from the back. The Cu plate is thermally isolated from the holder by quartz spacers. The sample is electrically connected to the transfer-holder by the clamps. The heater is a quartz-halogen 150 watt lamp, with a gold-coated quartz parabolic infrared reflector, which produces focused illumination. The focal point is situated at 1.9 cm from the base of the lamp. The Cu plate is situated closer to the lamp, at 1.4 cm, resulting in a more uniform illumination. The temperature of the Cu plate was measured using a chromel-alumel thermocouple as a function of the power dissipated by the lamp. This was done for several heating power settings. The fourth power of the absolute temperatures measured was plotted as a function of the heating power, obtaining a good linear correlation (Fig. 8). This is a consequence of the Stefan-Boltzman law that states that the power radiated by a black body is proportional to the fourth power of its absolute temperature [Morse, 1969]. In a vacuum environment (and particularly in the case of our experiment in which the Cu plate was thermally isolated by quartz spacers), heat is transmitted mainly by radiation. In thermal equilibrium, the power radiated by the body is equal to the power that it absorbs. In the case of the Cu plate in our experiments, the power absorbed is proportional to the power dissipated by the lamp. This accounts for the correlation observed between the fourth power of the temperature of the Cu plate and the heating power. This allowed extrapolations and interpolations of the temperature calibration to other power settings. Cu plate temperatures up to 850°C were obtained. For $SrTiO_3$ and MgO substrates, the temperature at the surface of the substrate was estimated by optical pyrometry to

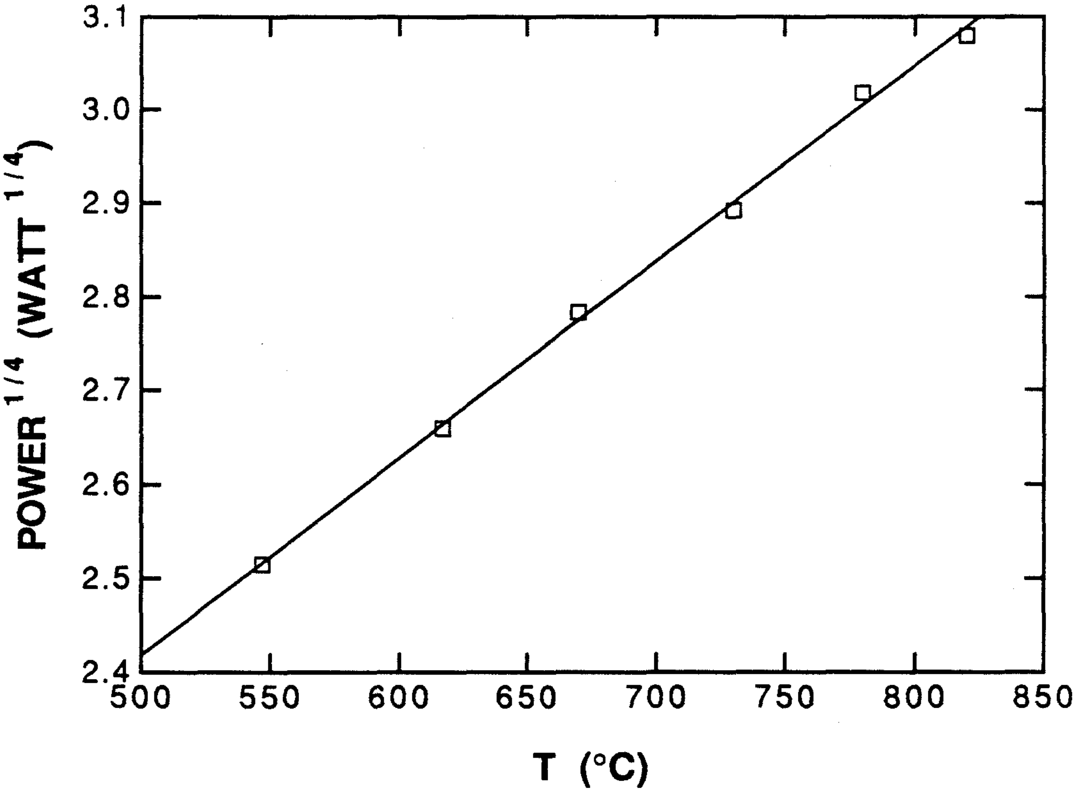

Fig. 8. Relation between heating power and temperature of the Cu plate on which the samples were mounted.

be ~ 100°C lower than the Cu plate temperature, at a Cu plate temperature of 800°C. For some experiments in which films were grown on substrates thinned for transmission electron microscopy, the temperature was measured by optical pyrometry. A calibration of temperature as a function of the heating power was done, obtaining in this case as well, a Stefan-Boltzman type of correlation.

The substrate stage can be rotated continuously during deposition to improve the lateral uniformity of the films. Electrical connections to the stage are done through sliding contacts to avoid tangling of the cables. The substrate stage has vertical motion as well. The typical target-substrate distance during deposition is ~ 10 cm, and the sputtering angle at this position for the center of the substrate stage is ~20° (measured from the normal to the target surface) for a horizontally mounted target.

The substrate-bombardment source was used with single grid optics, to obtain higher currents at low beam energies. The distance from the source to the substrate is typically 22 cm, and the angle of incidence of the ion beam is approximately 35°. The beam divergence is approximately 30°.

The layer thicknesses are controlled by a shuttering mechanism actuated by a solenoid valve. The shutter moves horizontally, approximately 2 cm below the substrate stage. Layer thicknesses are measured by a quartz crystal thickness monitor. For layer thicknesses in the monolayer range, the closing of the shutter is determined by a preset time. The appropriate deposition time for each layer, in this case, is obtained from a thickness measurement done on the whole film after growth. The stability of the Kaufman type ion source is essential for achieving a good layer thickness control.

The sequential deposition process is fully automated, and the stacking sequence can be programmed arbitrarily. The program allows to choose for each layer the sputtering target, the opening and closing of the shutter, and the sputtering ion source current and energy. In Fig. 9, a typical sequential deposition process is illustrated. As shown in Fig. 9, for each layer there are several subdivisions of the process. This allows, for example, the use of a pre-sputtering stage to clean the target before the deposition of each layer. The closing of the shutter is determined either by a preset time or a preset thickness as measured by the quartz crystal monitor.

The Y-Ba-Cu-O films were grown by sputtering from elemental Y (99.9%), Ba (99.9%) and Cu (99.999%) targets, using an Ar^+ ion beam. Ultra high purity Ar (99.999%) was used as the working gas for the sputtering ion source. Since Ba reacts strongly with oxygen, the Ba target was kept under vacuum for the duration of this work. Several ways of supplying oxygen to the samples during growth were used, including an O_2^+ beam and molecular oxygen. In both cases, ultra high purity oxygen (99.999%) was used. All gases introduced to the deposition chamber during growth

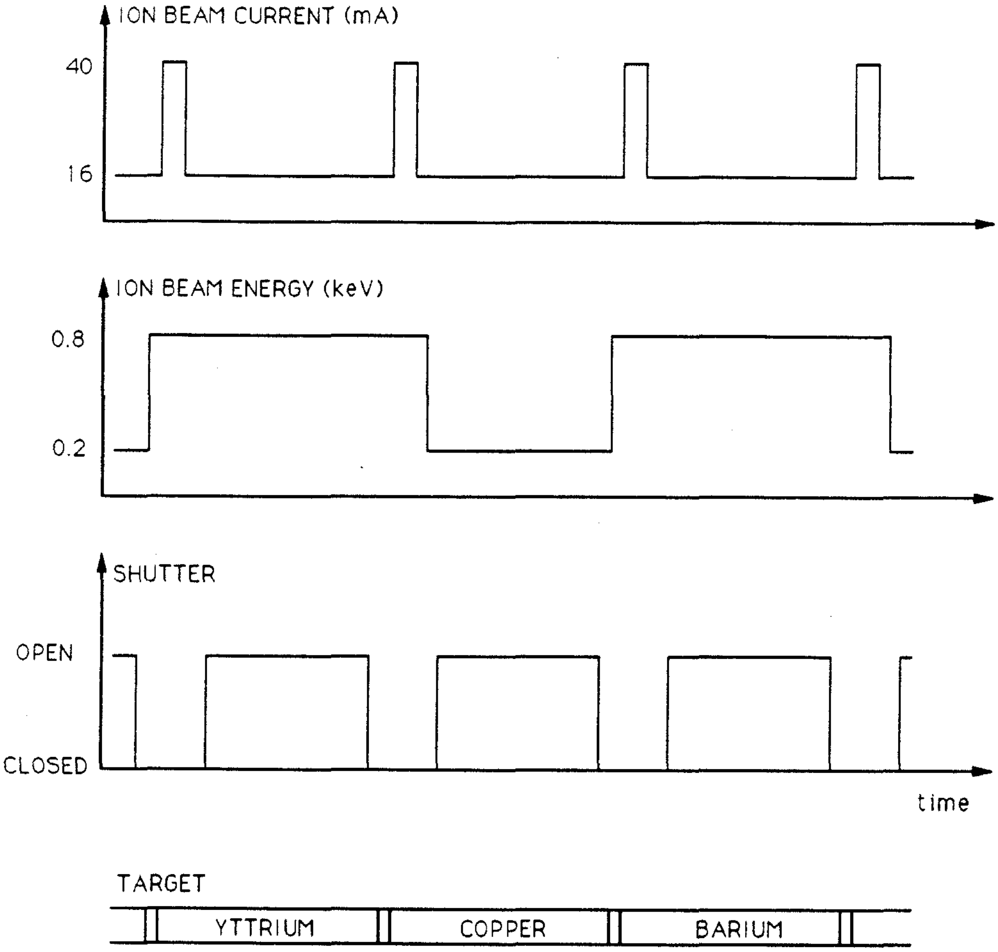

Fig. 9. Example of sequential deposition process. The pulses of high ion beam current shown in this example are used to sputter-clean the targets before the deposition of each layer.

(Ar and O_2), were circulated through a liquid-nitrogen trap. The flows were controlled by fine-metering needle valves.

The substrate-bombardment source was used to produce the O_2^+ beam. Both tungsten and thoria-coated iridium were used as cathode filaments, obtaining typical lifetimes of 2 hours and 15 hours respectively. The tungsten filaments were 0.25 mm diameter wires, 5 cm long. To obtain similar emission characteristics with thoria-coated iridium, three ribbons of 0.002 inch × 0.027 inch × 2.5 inch (available commercially as ion-gauge filaments) were connected in series.

Films were also grown with molecular oxygen, introduced to the deposition chamber via feedthroughs. In some cases, the O_2 outlet was located away from the sample in order to study film growth under a controlled background pressure of oxygen (corresponding to region (4) in Fig. 3). In most cases, the O_2 outlet was located in the vicinity of the sample (at 1.5 cm) to enhance the local partial pressure of oxygen (region (3) in Fig. 3). Two types of geometries were used in this case, as shown in Fig. 10. In one case, a single outlet was situated at the end of a cylindrical tube. In the other case, four outlets were situated in a ring-shaped tube, to produce a more uniform oxygen flux at the sample. The O_2 feedthroughs were mounted on precision alignment motion ports, so that they could be moved away from the vicinity of the sample stage when samples were transferred in or out of the deposition chamber. The position of the ring or tube was, in consequence, adjustable.

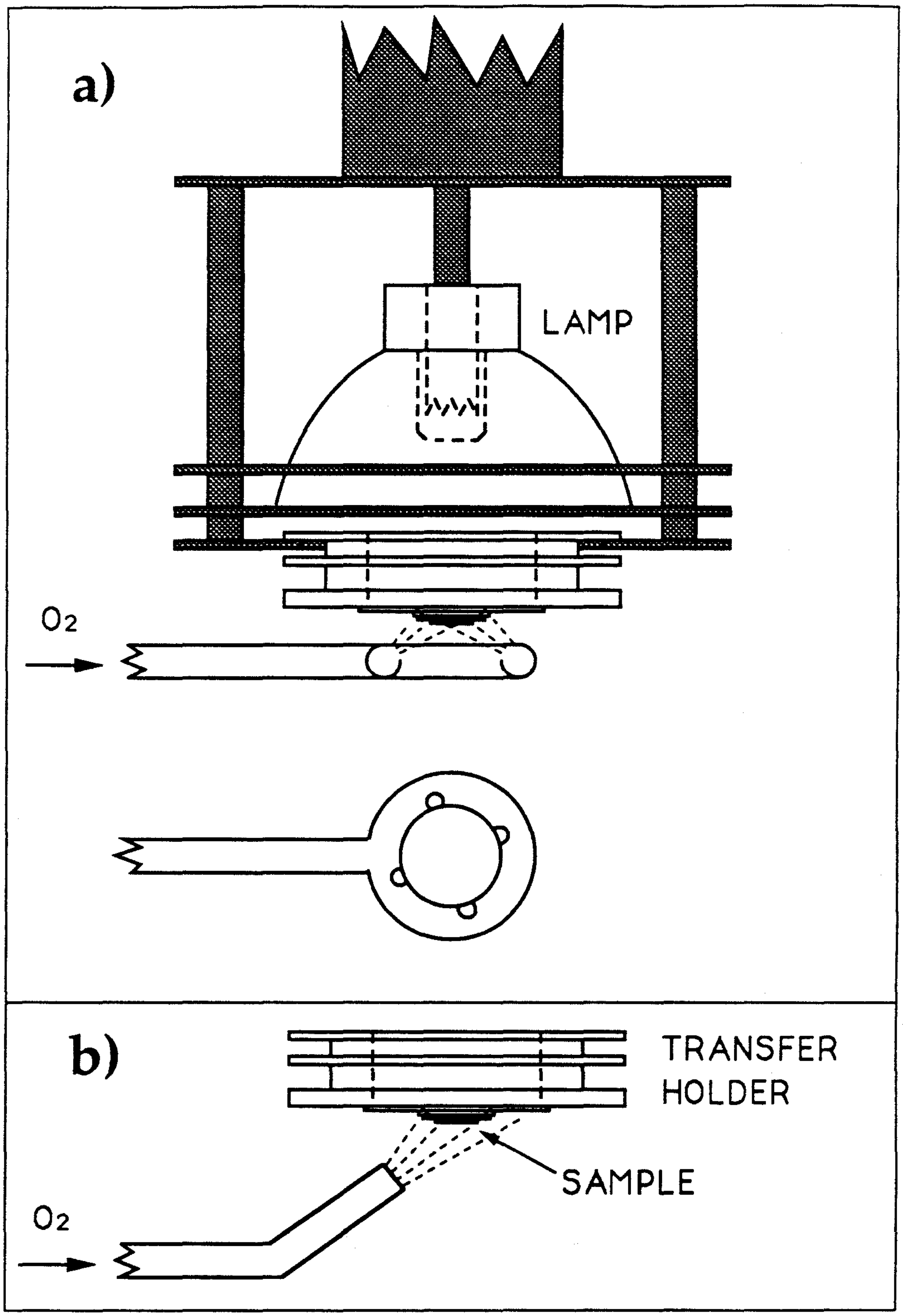

Fig. 10. Sample stage (a), and configurations of oxygen supply used to enhance the local oxygen pressure at the sample during *in situ* growth: (a) ring, and (b) tube.

The ion sources were run without neutralizer filaments, since tungsten contamination was observed in films grown using tungsten neutralizer filaments in background partial pressures of $O_2 \geq 10^{-5}$ Torr. No tungsten contamination was observed in films grown without neutralizer filaments.

Iron contamination was observed in some films, and determined to come from stray-ion sputtering from the stainless steel carousel. The carousel was then coated with Cu after which no Fe contamination could be detected in the films.

Films were grown on (001) $SrTiO_3$ and (001) MgO polished substrates. The typical substrate dimensions were 0.5 cm × 0.5 cm × 0.05 cm. The substrates were mounted with crystal bond on a glass slide, cut with a diamond saw, and removed from the glass slide. They were then cleaned using organic solvents (acetone and propanol or methanol), and annealed in 1 atm of O_2 at 1000°C for 1 hour before loading into the UHV system.

Some samples were grown on thinned, electron transparent substrates, and could be analyzed in a transmission electron microscope without any further sample preparation. These included SiO_2/(001) Si, $CoSi_2$/(001) Si, (001) Si, and C coated Ag or Be grids. Films were also grown on (001) Si, mainly for calibration purposes.

2.5 Sample Characterization

Samples were characterized by x-ray diffraction, transmission electron microscopy, scanning electron microscopy, optical microscopy, Rutherford backscattering spectrometry, energy dispersive x-ray analysis, and low temperature resistivity measurements.

X-ray diffraction $\theta-2\theta$ spectra were taken with Cu radiation in a high resolution geometry, using a Siemens D500 x-ray diffractometer (which is integrated to the UHV system). A Ni filter was used to reduce Kβ radiation. In typical scans, using 1° x-ray tube slits and 1° and 0.05° detector slits, the instrumental broadening was ~0.1°- 0.15°, after correcting for Kα_2 broadening. Scans in the small angle region were also taken from multilayer films, using 0.1° slits for the x-ray tube and 0.1° and 0.018° slits for the detector.

The lattice parameters of films were determined from the x-ray data by high angle extrapolations. The main source of error was determined to be the sample height. In this case, the experimental lattice parameter d_{exp}, is given by

$$d_{exp}(\theta) = d_o + \frac{\cos^2(\theta)}{\sin(\theta)} \frac{\Delta}{R} , \qquad (2.5.1)$$

where θ is the angle of incidence of the x-ray beam, d_o is the lattice parameter of the sample, Δ is the height misalignment of the sample, and R the radius of the focusing diffraction circle [Klug and Alexander, 1974]. The c-axis parameters of "123" films were determined by least squares fits, using expression (2.5.1), for the (00*l*) series (typically from (001) up to (007)).

The presence of inhomogeneous strains in the films was determined by analyzing the width of the x-ray Bragg peaks for several orders of diffraction. The effects of finite crystal size and inhomogeneous strains were separated, through their different dependence on wave vector on reciprocal space. The line broadening due to finite crystal size along the film surface normal (c-direction) is constant in reciprocal space and given by

$$\Delta K \cong 0.9 \ (2\pi/L)\,, \tag{2.5.2}$$

were L is the crystal size. The line broadening due to inhomogeneous lattice distortions along the c-direction is given by

$$\Delta K \cong 2.4 \ \epsilon_{rms} K, \tag{2.5.3}$$

were $\epsilon = \delta c/c$ is the local inhomogeneous lattice distortion along the c-direction, $\langle \epsilon \rangle = 0$ and $\epsilon_{rms} = \langle \epsilon^2 \rangle^{1/2}$ is the root mean square inhomogeneous lattice distortion [Klug and Alexander, 1974].

Transmission electron microscopy was performed in a Phillips 430, 300 keV microscope, with energy dispersive x-ray analytical capability. The microscope was operated to form images by bright field (BF), dark field (DF), or high resolution (phase) contrast . In BF or DF imaging, only one transmitted beam (the direct beam in BF, a diffracted beam in DF) is used to form the image. In high resolution imaging, the lattice image is formed by the interference of at least two transmitted beams [Ruhle and Wilkens, 1983]. In plan-view studies of epitaxial films, we observed Moire patterns, produced by the difference in lattice constant between the film and the substrate. When two crystals that have the same orientation but different lattice constant overlap, a pattern of fringes (Moire pattern) is observed. The spacing of the Moire fringes D, is given by

$$D = \left| \frac{d_1 d_2}{d_1 - d_2} \right| \quad , \qquad (2.5.4)$$

where d_1 and d_2 are the lattice spacings of the two crystals [Ruhle and Wilkens, 1983]. The lattice mismatch δ, is give by

$$\delta = \left| \frac{2\,(d_1 - d_2)}{d_1 + d_2} \right| \quad . \qquad (2.5.5)$$

If δ is small ($d_1 \sim d_2$), we have

$$D \approx \frac{d_1}{\delta} \approx \frac{d_2}{\delta} \quad . \qquad (2.5.6)$$

The real space microstructural information obtained by the imaging techniques, was complemented by the electron diffraction patterns, produced by diffractions from crystal planes parallel to the microscope axis. The electron diffraction patterns provide crystallographic information, that is complementary to the information obtained from x-ray diffraction. Although the accuracy in determining lattice parameters is much lower than in x-rays, there is more flexibility in analyzing the samples in different orientations. In particular, the electron diffraction patterns of plan-view samples, provide in-plane crystallographic information. Samples were analyzed both in cross section and in plan-view. For transmission electron microscopy of samples grown on $SrTiO_3$, the samples were lapped to a thickness of 100 µm and then dimpled to a thickness of 10-30 µm. An argon ion mill was then used to thin the samples to electron transparency. The last hour of ion milling was performed at liquid nitrogen temperatures to attempt to minimize ion damage. The cross section samples were cemented face to face prior to lapping, dimpling, and ion milling. For samples grown on MgO, material of the sample surface was removed by scratching it with a diamond tip, and then placed between two carbon coated grids. A fraction of the pieces of sample spread on the grids consisted of film detached from the substrate, and constituted good specimens for plan-view analysis. For cross-sectional analysis, the material scratched from the sample surface was crushed with a pistol and mortar in propanol, before placing it between the grids. A few pieces of sample were close enough to the correct orientation, so that cross sectional analysis could be done after adequate tilting.

The electrons from the microscope electron beam, have energies high enough to cause the ejection of tightly bound inner-shell electrons from the sample atoms. Subsequent decay of these excitations are accompanied by the emission of characteristic x-rays. The wavelengths and intensities of the x-rays emitted, are used in energy dispersive x-ray analysis (EDX) to determine the elements present in the sample, and their relative concentrations. This technique was used, in this work, to determine the composition of films, and the presence of impurity elements. For this purpose, calibration films were grown on carbon coated Ag and Be grids at room temperature. The typical thickness of a calibration film was 100-200 Å. The departures from the ideal composition were determined by comparing the ratios of the K lines from yttrium, the L lines from Ba, and the K lines from copper, to those of a standard. The standard had the ideal $YBa_2Cu_3O_{7-\delta}$ composition as determined by Rutherford backscattering spectrometry. Typical errors in the determination of cation ratios were ~5%.

Film thicknesses were determined by cross-sectional transmission electron microscopy and by Rutherford backscattering spectrometry.

Rutherford backscattering spectrometry was performed using He ions at energies ranging from 2 to 3.2 MeV. Measurements were done on films grown on (001) Si substrates at room temperature, and on (001) MgO substrates at various deposition temperatures. Typical errors in the determination of cation ratios and thicknesses were ~3% and ~10% respectively.

For typical film thicknesses of ~400 Å, the cation ratios were determined from the total number of counts in the corresponding signals, using the Rutherford cross sections. The film thickness, *t*, was determined from the total number of counts in the Y, Ba and Cu signals, and the height of the substrate signal (Si or Mg).

The atomic ratio of element A to B for a film of composition A_mB_n is given by

$$\frac{\mathrm{m}}{\mathrm{n}} = \frac{A_A/\sigma_A(E_o)}{A_B/\sigma_B(E_o)}, \tag{2.5.7}$$

were A_A and A_B are the total number of counts in the signals of elements A and B, σ_A and σ_B the corresponding Rutherford cross sections, and E_o the energy of the incident He ions. Note that the expression in the right hand side of the equation is independent of the incident particle energy, since the energy dependence of the Rutherford cross section is the same for all elements and factors out. This equation does not assume the surface energy approximation, and is valid for thick films as well (this again, is a consequence of the way in which the Rutherford cross section depends on energy). For a thin film of composition A_mB_n, deposited on a substrate of composition C_kD_l, the film thickness, *t*, is given in the surface energy approximation by

$$t_{A_mB_n} \cong \frac{\mathrm{k}}{\mathrm{m}} \frac{\sigma_C(E_0)}{\sigma_A(E_0)} \frac{A_A}{H_C} \frac{\mathcal{E}}{[\varepsilon_0]_C^{CD} N^{AB}} , \tag{2.5.8}$$

were σ_C is the Rutherford cross section of element C, H_C the height of the signal of element C at the front edge of the signal (corresponding to the region near the film-substrate interface) measured in counts per channel, $\mathcal{E}$ the energy width of a channel (which is determined by the electronic setting of the detecting system), $[\varepsilon_0]_C^{CD}$ the stopping cross section factor in C_kD_l for particles scattered from element C in the surface energy approximation, and N^{AB} the number of molecules A_mB_n in the film per unit volume.

For thicker films (thicknesses ≥ 1000 Å), the film thickness was determined from the signal widths. When the signals from the different elements overlapped, the composition was determined by the signal heights. In order to separate the signals from the different elements in films of ~1500 Å, incident energies of ~ 3 MeV were used.

The atomic ratio of element A to element B in a film of composition A_mB_n is obtained from the signal heights, in the surface energy approximation by

$$\frac{\mathrm{m}}{\mathrm{n}} \cong \frac{H_A\,[\varepsilon_0]_A^{AB} / \sigma_A(E_0)}{H_B\,[\varepsilon_0]_B^{AB} / \sigma_B(E_0)} , \tag{2.5.9}$$

and the film thickness from the signal width by

$$t_{A_mB_n} \cong \frac{\Delta E_A}{[\varepsilon_0]_A^{AB} N^{AB}} , \tag{2.5.10}$$

were ΔE_A is the energy width of the signal from element A. For a thorough description of the Rutherford backscattering spectrometry technique, and the deduction of the expressions used to compute thicknesses and compositions, see Chu et al., 1978.

Low temperature resistivity measurements were done using the AC four point probe technique [Logan, 1961], in a He closed cycle cryogenic system.

Chapter 3: Three Step Processes

3.1 $YBa_2Cu_3O_{7-\delta}$ Films Grown by Sequential Ion Beam Sputtering

There has been considerable interest in the growth of high-Tc superconductor films, due to their potential applications in electronic devices, SQUIDS, etc [Chaudhari et al., 1987; Oh et al., 1987; Webb et al., 1987; Char et al., 1987; Dijkkamp et al., 1987]. The $YBa_2Cu_3O_{7-\delta}$ ("123") phase, is a preferred candidate to study the growth of high-Tc superconductor films, since it is the simplest phase (the one with the smallest number of components and simplest structure) that is superconducting above the temperature of liquefaction of nitrogen (77 K). We have investigated the growth of $YBa_2Cu_3O_{7-\delta}$ films by a three step process, using a sequential ion beam sputtering deposition technique.

Films were deposited at room temperature from separate Y, Ba, and Cu targets by sequential ion beam sputtering as described in section 2.4. Oxygen was supplied during deposition by a Kaufman-type ion source. The O_2^+ ion beam, with a current of 20 mA and an energy of 100 eV, was directed towards the sample. The sputtering, Kaufman type ion source current was 40 mA, and the beam energy was 1000 eV. The argon partial pressure in the chamber (arising from the sputtering ion source) was

1×10^{-4} Torr, and the oxygen partial pressure (arising from the substrate-bombardment ion source) was 1×10^{-4} Torr. The layer thickness was controlled by a quartz crystal rate monitor. The average film growth rate was ~ 1 Å/s. The films consisted of multilayers, with a periodicity length of 60 Å. The 60 Å units were trilayers that resulted from the sequential deposition from the Y, Ba and Cu targets. The total film thicknesses ranged from ~1000 to 3000 Å, corresponding to ~20 to 50 trilayers. The thicknesses of the three layers that constitute the 60 Å unit were calibrated to produce the "123" stoichiometry. The as-deposited films were amorphous, however, due to the long-wavelength periodicity imposed artificially by the deposition technique, x-ray diffraction peaks were observed in the small angle region (Fig. 11). This demonstrates the achievement of a good layer thickness control.

The films were annealed in a furnace for 1/2 hour to 1 hour, in flowing oxygen, at temperatures in the range of 800-900°C, and then cooled down in the oxygen flow to 400°C. They were kept at that temperature for 1/2 hour to 1 hour before cooling down to room temperature, in order to induce the tetragonal to orthorhombic transition. After annealing, the films were predominantly single phase $YBa_2Cu_3O_{7-\delta}$. X-ray scans showed the (00*l*), and (*h*00) diffraction peaks from the "123" phase (Fig. 12). In higher resolution x-rays scans (taken using a .018° detector slit, and 0.02° steps) performed around the (002) substrate peak, the "123" (020) peak was observed (Fig. 13). In standard scans (0.15° detector slit, 0.05° steps) the (0*k*0) peaks were not resolved from the substrate peaks.

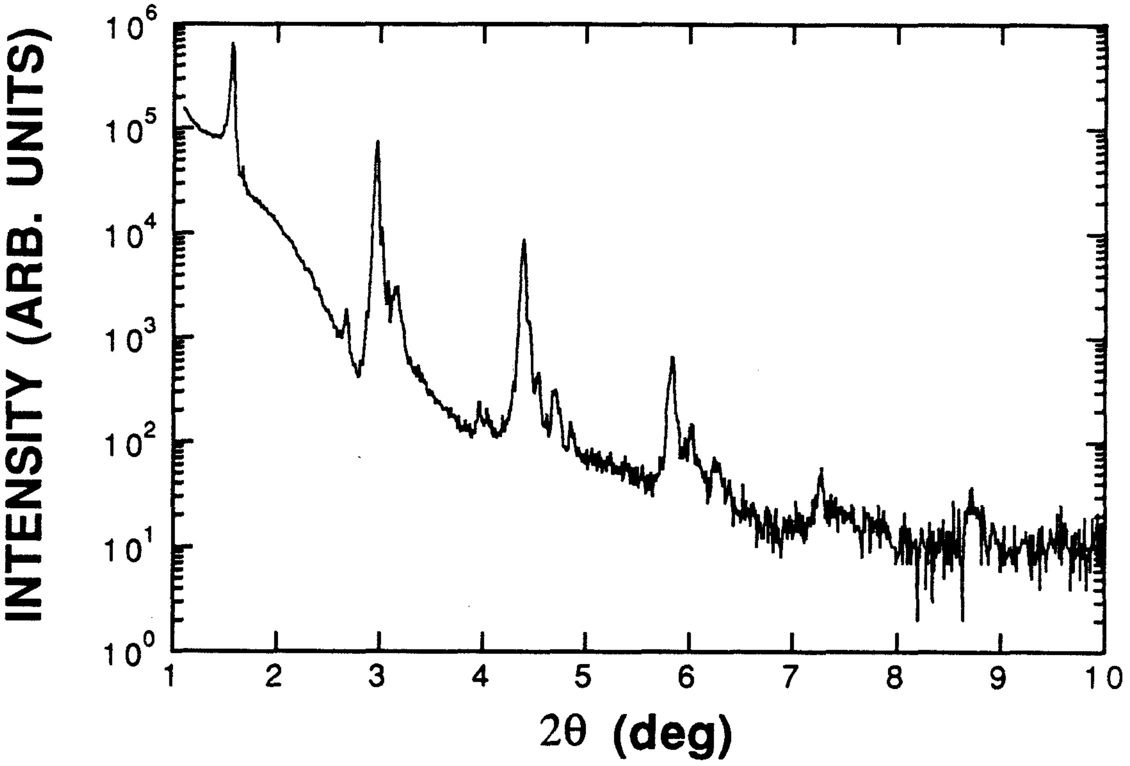

Fig. 11. Small angle x-ray diffraction pattern of as deposited film. The Bragg peaks observed are produced by the artificial composition modulation imposed by the sequential deposition process. The modulation wavelength is 60 Å.

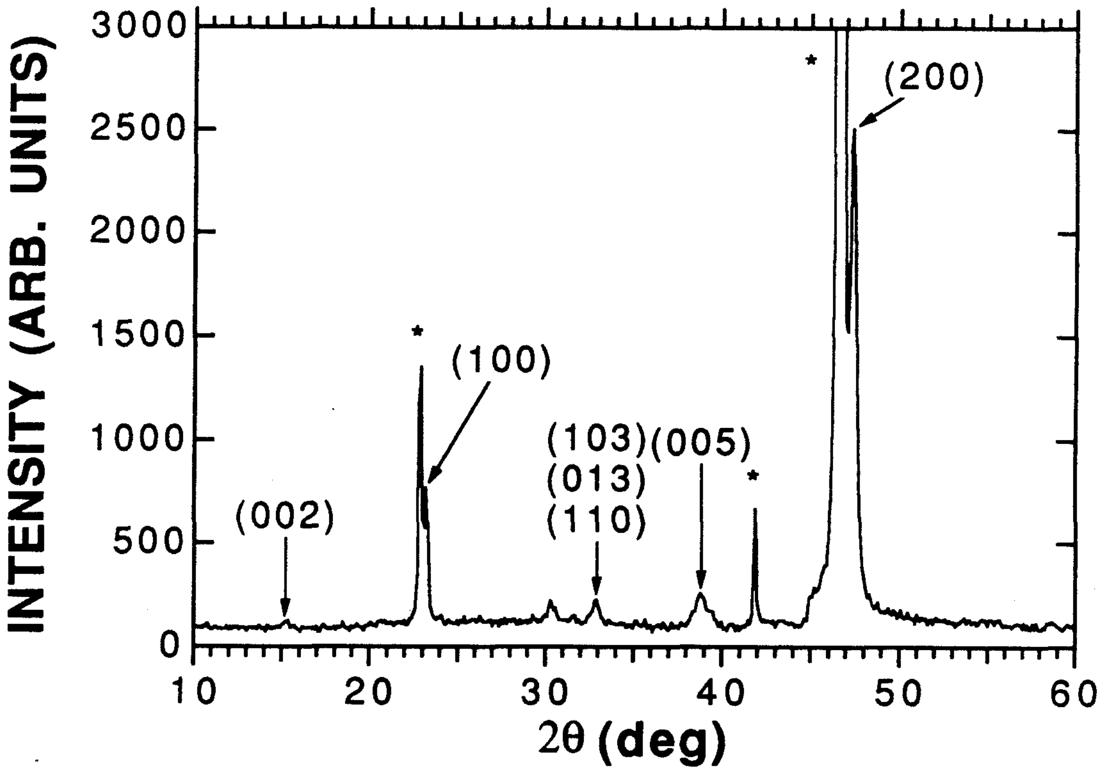

Fig. 12. X-ray diffraction pattern of a film grown on $SrTiO_3$ after high temperature anneal in oxygen. The substrate peaks are marked with an asterisk.

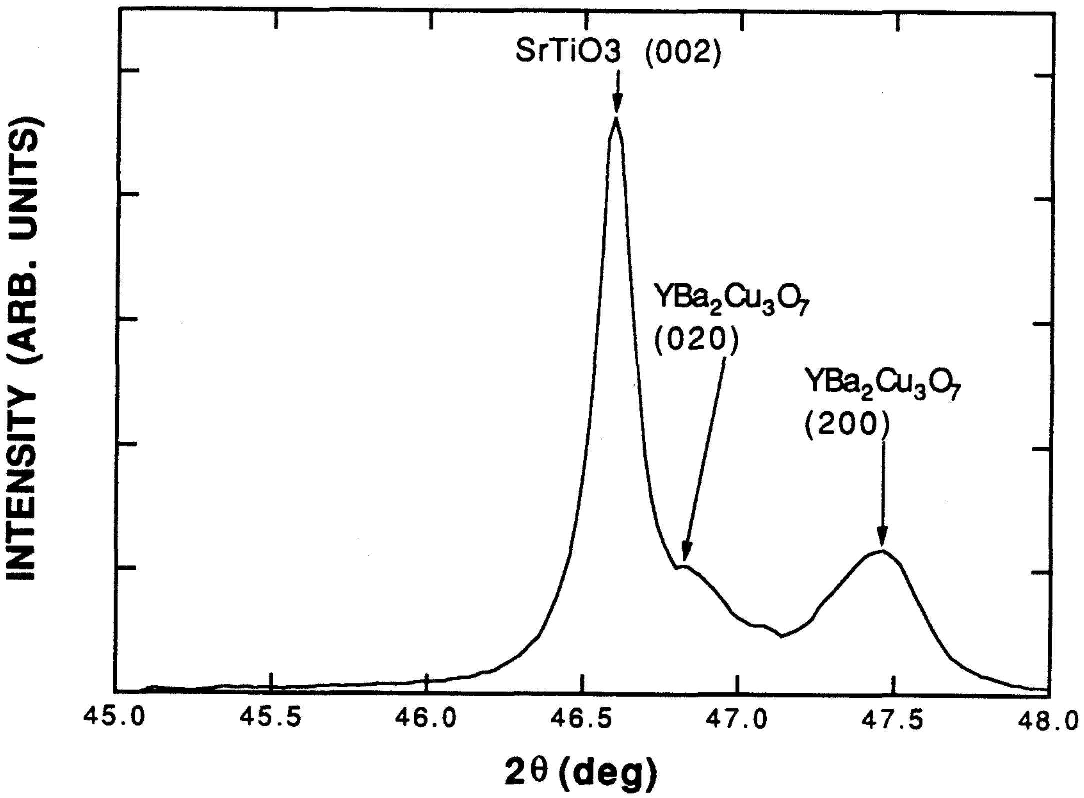

Fig. 13. Portion of the x-ray diffraction pattern of a film grown on $SrTiO_3$ after high temperature anneal in oxygen, showing the orthorhombic splitting of the (200) and (020) peaks. The data was corrected for Kα broadening.

A small amount of a second phase was present in the films, as indicated by the diffraction peak in the x-ray pattern at about 30.3° (Fig. 12). The identification of this impurity phase based on this information is not possible, since there are various phases in the Y-Ba-Cu-O system with the strongest diffraction peak close to the one observed. The diffraction peak at ~32.9°, with lattice spacing of ~2.73 Å corresponds to the (013), (103), and (110) diffractions (not fully resolved). These are the strongest diffractions in the powder diffraction pattern of $YBa_2Cu_3O_{7-\delta}$. The presence of this peak in the diffraction pattern, characteristic of randomly oriented polycrystalline "123", indicates the presence of a fraction of randomly oriented "123" in the film.

Resistivity measurements by the four-point technique indicated the onset of the resistive superconducting transition above 90 K. The films showed zero resistivity at lower temperatures (Tc (R=0) ~ 70 K), presenting rather broad transitions. The lattice parameters obtained in the films had similar values to those reported for bulk $YBa_2Cu_3O_{7-\delta}$ samples [Cava et al., 1987b].

3.2 TEM Studies of Y-Ba-Cu-O Films Grown by Magnetron Sputtering

There has been considerable interest on Y-Ba-Cu-O superconducting films grown by three step processes, in which the deposition sources contain fluorine [Mankiewich et al., 1987; Levi et al., 1988; Marshall et al., 1988; Gupta et al., 1988]. The as-deposited films are amorphous, and the superconducting phases are obtained by annealing at high temperatures (800-900°C) in the presence of wet oxygen. The water vapor aids in converting the fluorine containing film to the superconducting phase. The annealed films have two superconducting phases, $YBa_2Cu_3O_{7-\delta}$ ("123") and $YBa_2Cu_4O_{8-x}$ ("248"). The "248" phase has been observed to form in Copper rich films containing halogens [Marshall et. al, 1988; Kwo et al., 1988a]. The "248" phase is a superconducting phase with a Tc about 10° lower than the "123" phase. The unit cell of the "248" phase consists of a doubling of the unit cell of the "123" phase, with an extra Cu-O plane. The c-axis lattice parameter of the "248" phase is 27.2 Å.

The films analyzed in this study were grown at Hughes Research Laboratories by magnetron sputtering from separate Y, BaF_2 and Cu sources [Clemens et al., 1988]. Films were grown on (001) $SrTiO_3$, and were amorphous as-deposited. Typical film thicknesses were on the order of 0.3 μm. Superconducting films with Tc(R=0) above 90 K and sharp resistive transitions ($\Delta T \sim 1$ K) were obtained by anneals in wet oxygen for 1/2 hour at 850°C. X-ray studies showed the presence of the (00*l*) and the (*h*00) peaks of the "123" and the (00*l*) peaks of the "248" phases in films annealed at 850°C for 1 hour (note that the (0*k*0) peaks from the "123" phase overlap with the substrate peaks). X-ray analysis of a film heated to 800°C and furnace cooled, showed the most prominent features to be the (00*l*) "248" peaks, suggesting that this phase nucleates first in the crystallization process [Clemens et al., 1988]. Scanning Electron Micrographs showed that the films had rough surfaces. The more prominent features were rectangular grains, of ~1μm by 10 μm in two orientations at 90° from each other, indicating that these grains were epitaxial. These grains gave a basket-weave appearance to the film surface [Clemens et al., 1988].

In order to be able to control the surface morphology, orientation and crystal quality of superconducting films, an understanding of the nucleation and growth properties of the films is necessary. For this purpose, we performed TEM analysis on films with different annealing treatments, and focused on the sequence and character of nucleation and growth of the superconducting phases from the as deposited amorphous matrix. The sample preparation for TEM studies (described in detail in section 2.5) consisted of dimpling and ion-milling.

A sample taken to 750°C and then furnace cooled was investigated in cross section and plan-view. In Fig. 14, we show a cross-sectional micrograph of this sample. A plate-like crystal of the "248" phase that nucleated epitaxially at the film-substrate interface with the c-axis parallel

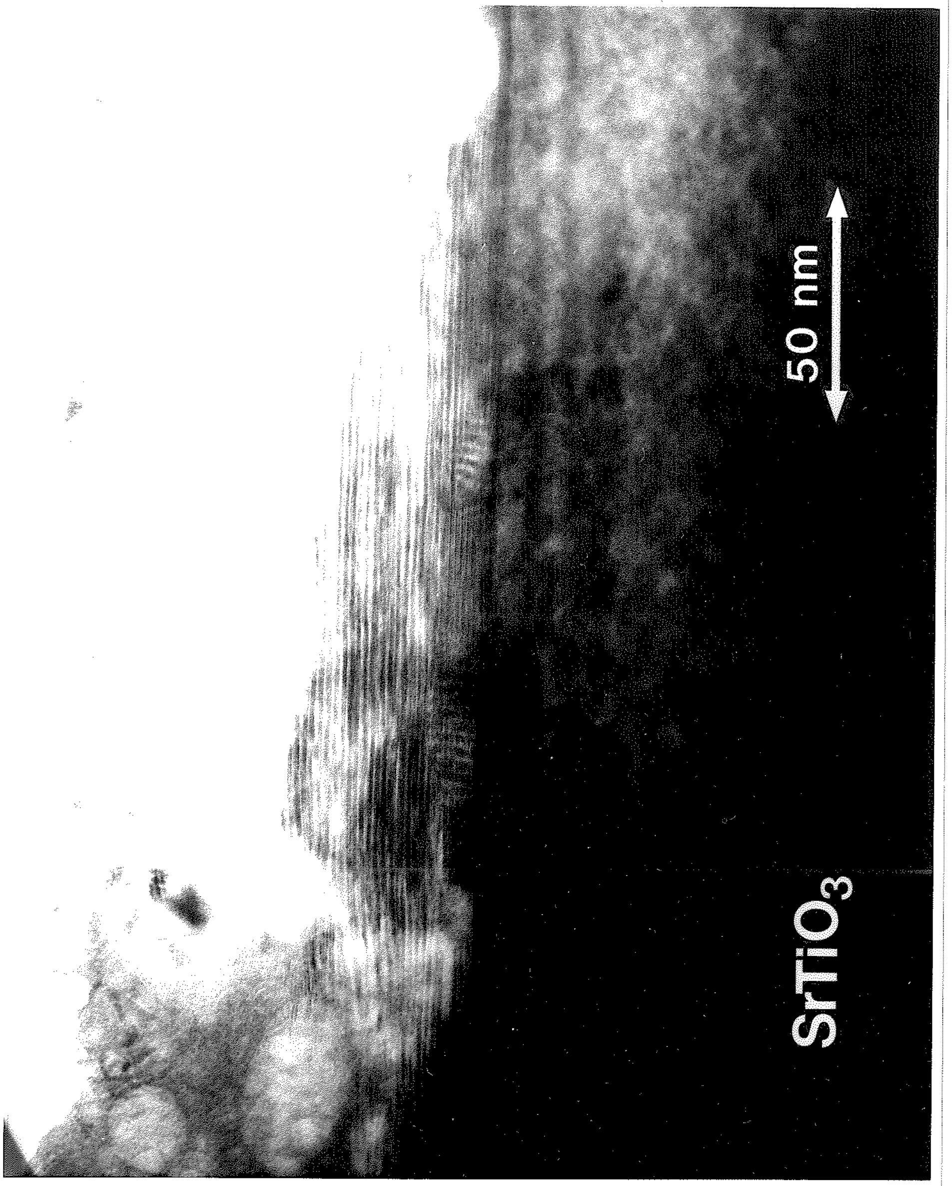

Fig. 14. Cross-sectional TEM view of a sample heated to 750°C and furnace cooled. The lattice fringes observed correspond to the c-axis planes of the "248" phase that nucleated at the film-substrate interface.

to the substrate surface normal ([001] direction) is observed. The lattice fringes seen in this grain correspond to the c-axis planes of the "248" crystal. Plan-view analysis of this sample showed Moire patterns corresponding to the lattice mismatch between the "248" phase (oriented with the c-axis normal to the substrate surface) and the substrate. The Moire patterns indicated that approximately 70-80% of the substrate was covered by epitaxial c-axis oriented "248" grains. In addition, smaller grains (~100 Å large) of the "123" phase, were observed both in plan-view and in cross-section to have nucleated with random orientations in the bulk of the film. We also observed in plan-view analysis, a small amount of needle-shaped "123" crystals, of about 2000-3000 by 500 Å. These grains were oriented with the c-axis along the [100] or [010] substrate directions. Similar, but larger "123" grains were observed in plan-view analysis of a sample taken to 800°C and furnace cooled. In this sample, the grains had dimensions of ~1μm by 1000 Å (Fig. 15).

Another sample was annealed at 850°C for 1 hour in wet oxygen, and analyzed in cross-section (Fig. 16). We observed the presence of large, flat, c-axis oriented crystals of both the "123" and the "248" phase near the film-substrate interface. We also observed large "123" crystals with the c-axis along the [100] or [010] substrate directions. Crystals with these orientations protruded from the film surface, indicating a fast growth rate along the substrate normal direction. These crystals are the result of the growth of the needle-shaped crystals observed on films with lower temperature anneals, and are the ones that give the basket-weave

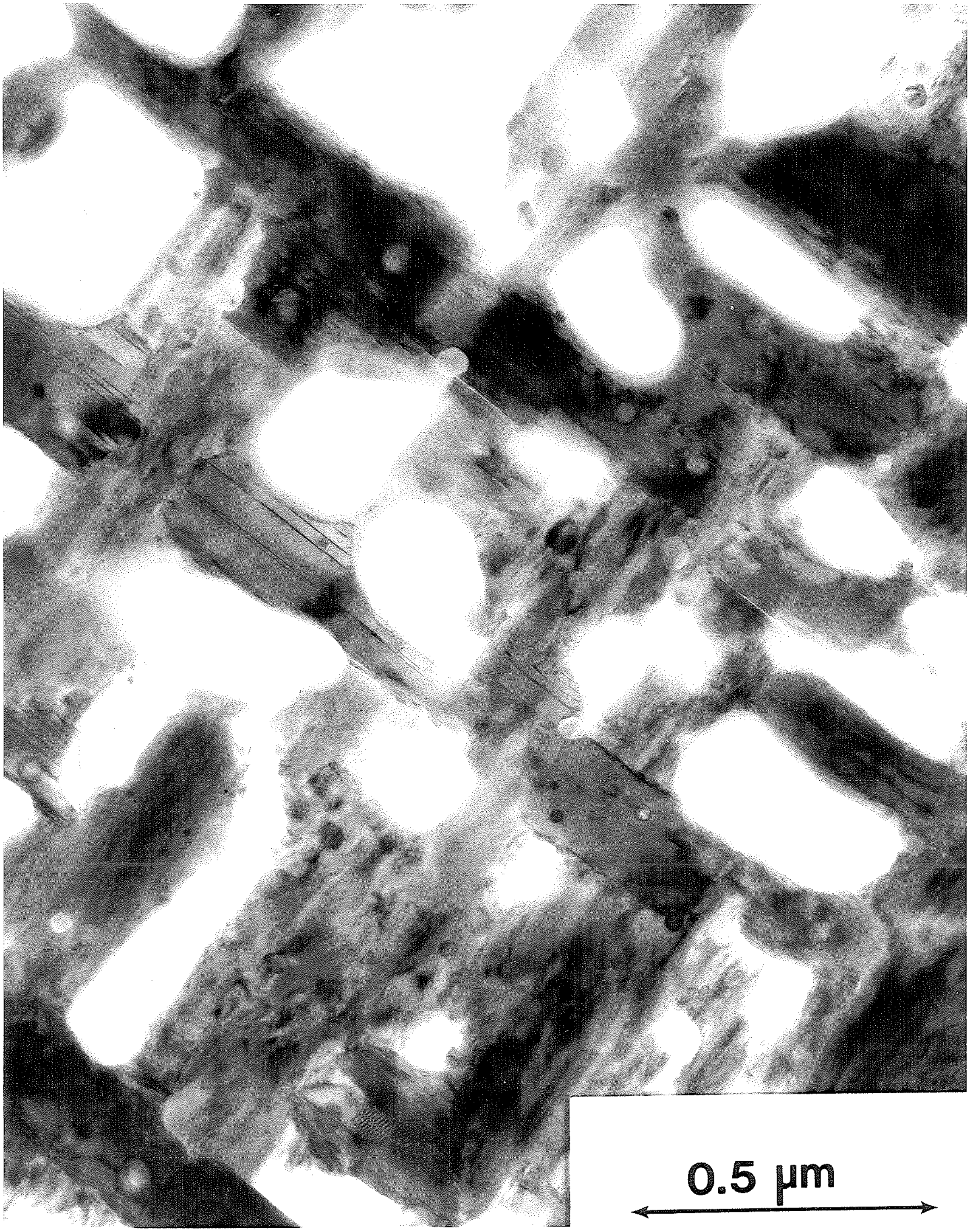

Fig. 15. Plan-view TEM of a sample heated to 800°C and furnace cooled. The needle shaped crystals observed correspond to "123" with the c-axis in the plane of the substrate.

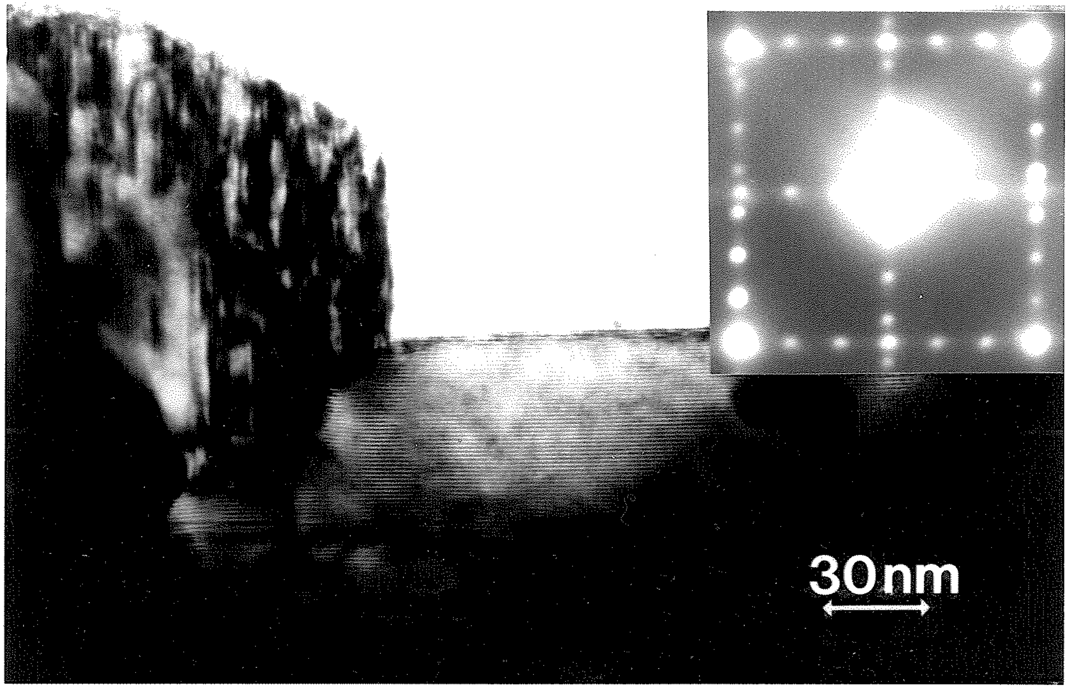

Fig. 16. Cross-sectional TEM view of a sample annealed at 850°C for 1 hour. The crystal protruding from the film surface has the c-axis in the plane of the substrate. The crystal that shows a smooth surface, has the c-axis normal to the plane of the substrate. The inset shows the electron diffraction pattern.

appearance to the scanning electron micrographs. The cross-sectional analysis also showed that near the interface there is a disordered region (Fig. 17). This was not observed in films with milder anneals, and may correspond to a substrate-film reaction. The inset in Fig. 17 shows the electron diffraction pattern. In this diffraction pattern, we can see the spots corresponding to the c-direction of the "123" phase along the direction parallel to the substrate surface. The spacing of this spots is ~1/3 of the spacing of the substrate spots, that corresponds to the relation $a_{SrTiO_3} \sim 1/3\ c_{YBa_2Cu_3O_{7-\delta}}$. In contrast, in the direction normal to the substrate surface, the spacing of the diffraction spots corresponding to the film is approximately 1/3.5 of the spacing of the substrate spots. This indicates that the crystal contributing to the diffraction is of the "248" phase.

The morphologies observed in the films, the geometry of grains observed in the TEM analysis, and the sequence in which they nucleate and grow is consistent with the crystal growth being slower along the c-direction than along the a- or b-directions. The crystals that nucleate at the interface with the c-axis normal to the substrate surface, grow fast in the plane of the substrate, tending to cover it, and grow slow in the normal direction. This results in flat c-axis oriented crystals near the interface. The crystals that nucleate with the c-axis in the plane of the substrate, have two different growth rates (one fast and one slow) along this plane, resulting on the needle-shaped crystals observed in plan-view. The growth rate of these crystals along the substrate normal direction is fast, resulting in the protruding crystals observed in cross-section.

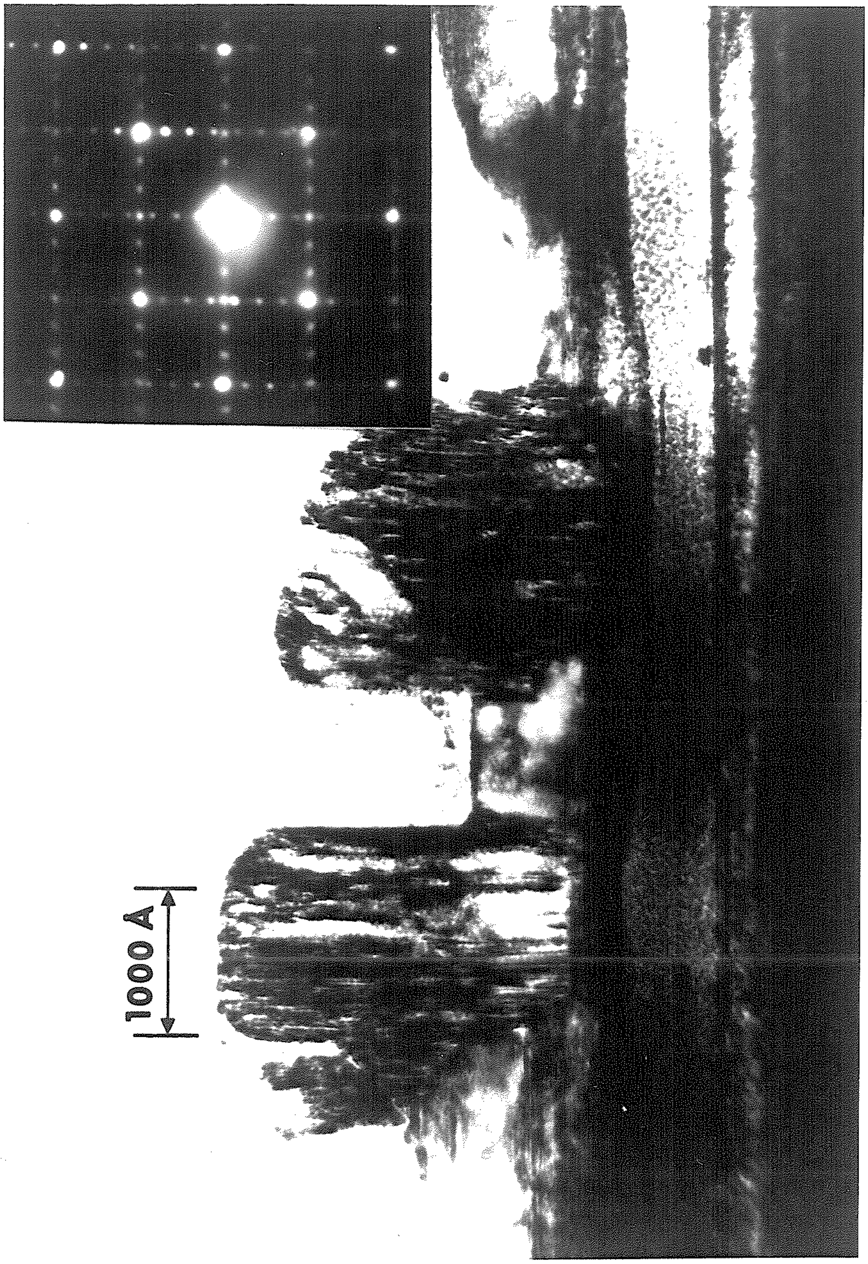

Fig. 17. Cross-sectional TEM view of a sample annealed at 850°C for 1 hour. The crystals protruding from the film surface have the c-axis in the plane of the substrate. A disordered layer is observed at the film-substrate interface. The inset shows the electron diffraction pattern.

The presence of the "248" phase is believed to be due to the initial fluorine content of the films, which may help to stabilize this phase [Kwo et al., 1988a]. This is consistent with our observations that show that the "248" phase nucleates before the "123" phase. At the initial stages of annealing, the fluorine content of the films is high, and it decreases as the annealing proceeds.

3.3 Conclusions

In conclusion, we have demonstrated the sequential ion beam sputtering technique to grow superconducting $YBa_2Cu_3O_{7-\delta}$ films. We have analyzed the orientation relations, microstructure, nucleation and growth process, and morphology of Y-Ba-Cu-O films grown on $SrTiO_3$ substrates by three step processes. We found the films to present several epitaxial orientations, with the film [001] direction along one of the substrate <001> directions. We interpreted the rough surface morphologies observed in the films as a consequence of the multiple orientations present and the anisotropy of crystal growth rate in the "123" and "248" structures.

Chapter 4: *In Situ* Growth

4.1 Deposition Process

Several *in situ* techniques have been reported for the growth of high T_c superconductors, such as magnetron sputtering [Adachi et al., 1987; Li et al., 1988; Geerk et al., 1989], laser ablation [Witanachchi et al., 1988; Chang et al., 1988], plasma assisted evaporation and MBE [Terashima et al., 1988; Kwo et al., 1988b], and ion beam sputtering [Fujita et al., 1988]. In these techniques, the different metal atoms are deposited simultaneously. Recently there has been some activity focused on the *in situ* growth of high T_c materials by sequential deposition methods with individual layer thicknesses in the order of a few monolayers [Triscone et al., 1989; Fujita et al., 1989].

High T_c superconductors have layered structures. For a given superconducting phase, there are frequently several other related superconducting phases which differ from each other in the number of planes of the different components and the way in which they are stacked to form the unit cell. This is the case for example of the Bi-Sr-Ca-Cu-O, the Tl-Ba-Ca-Cu-O and the Y-Ba-Cu-O series. An *in situ* growth technique in which the different components are deposited sequentially with layer thicknesses in the monolayer range offers the possibility of selecting a particular stacking sequence and attempting the growth of artificially layered superconductors. The nucleation and growth characteristics in these kind of processes could be entirely different than in other techniques in which the different components are deposited simultaneously.

We have investigated the *in situ* growth of $YBa_2Cu_3O_{7-\delta}$ thin films [Kittl et al., 1990a]. The sequential ion beam sputtering deposition process described in section 2.4 was adapted to grow $YBa_2Cu_3O_{7-\delta}$ thin films *in-situ*. In this type of growth process, the crystalline phase grows monolayer by monolayer as the film is deposited. The high mobility of atoms on the surface (compared to the bulk) allows the nucleation and growth of the $YBa_2Cu_3O_{7-\delta}$ phase at lower temperatures than in films grown by three step processes. In order for this argument to be applicable to a sequential deposition process, the individual layer thicknesses must be in the monolayer range.

A Kaufman type broad beam ion source was used to sputter sequentially from elemental Y, Ba and Cu targets. Films were grown following the stacking sequence of $YBa_2Cu_3O_{7-\delta}$, with individual layer thicknesses nominally equal to one monolayer. In this way, the diffusion distances are minimized and the c-axis orientation (c-axis normal to the film surface) is favored.

The layer thicknesses were controlled by a shuttering mechanism. The closing of the shutter for each layer was determined by a preset deposition time, since the quartz crystal monitor is not accurate to determine thicknesses in the monolayer range. The appropriate deposition time for each element was calibrated by measuring the film composition and thickness after growth. The average layer thickness was determined from the total film thickness measured by Rutherford backscattering spectrometry and by cross-sectional transmission electron microscopy. The stability of the Kaufman type sputtering ion source, and the low deposition rates used (~10 s/monolayer), are fundamental for achieving good layer thickness control in the monolayer range.

The sputtering ion source parameters were varied from target to target in order to obtain similar deposition rates for the three elements, typically in the order of 10 seconds for each monolayer. The Ar^+ ion beam current was fixed at 16 mA. Ion beam energies to sputter Cu ranged from 180 eV to 280 eV. The ion beam energy to sputter Y and Ba was 800 eV. The background partial pressure of argon (arising from the sputtering ion source) was 3×10^{-4} Torr.

To ensure reproducibility and uniformity through the deposition, the targets were sputter cleaned and the process was run during a predeposition stage before activating the shuttering mechanism and starting the deposition (this is explained in more detail in section 4.2). The predeposition stage lasted typically one hour.

All the films were grown in an oxygen environment, achieved by introducing molecular oxygen into the chamber via a feedthrough, as described in section 2.4. The background partial pressure of oxygen (P_{O_2}) ranged from 1×10^{-4} Torr to 1×10^{-3} Torr. The local partial pressure of oxygen at the substrate was estimated to be 1 to 2 orders of magnitude higher (due to the proximity of the oxygen outlet situated at 1.5 cm from the substrate). Some films were grown under a controlled background oxygen pressure. The regions of the oxygen pressure--temperature diagram in which films were grown are shown in Fig. 3. A plasma was produced in the sputtering chamber during deposition, in the vicinity of the targets. As shown in Fig. 3, the deposition conditions were such that the films grew with the tetragonal, oxygen-deficient structure. In order to incorporate more oxygen into the structure, immediately after deposition, the partial pressure of oxygen was increased (typically by factors of 4-10), and the samples were cooled down to room temperature at a rate of 10°C per minute. In some cases, the films were annealed after deposition in a furnace, at 400°C, in oxygen for 1/2 hour. Films analyzed (structural and electrical properties) before and after this *ex situ* low temperature anneal showed, in most cases, no significant differences. This will be discussed in detail in section 4.5.

Films were grown on (001) MgO and on (001) $SrTiO_3$ substrates. The substrates were clamped to a Cu plate that was heated radiatively. The substrate temperatures ranged from 550 to 750°C (corresponding to Cu plate temperatures ranging from 650 to 850°C). Film thicknesses ranged from 300 Å to 1700 Å. The typical film thickness was 400 Å. Films were also grown on substrates thinned down to electron transparency, and on Si, as described in section 2.4.

4.2 Composition and Thickness Measurements

The compositions of the films were determined by Rutherford backscattering spectrometry (RBS), and by energy dispersive x-ray analysis (EDX), as described in section 2.5. EDX analysis was performed on 100-200 Å films grown at room temperature on carbon coated Ag or Be grids. Typical errors in the determination of cation ratios with these techniques were ~3% for RBS, and ~5% for EDX. Results from these two techniques were consistent within the experimental errors. Changes in the layer deposition times ≥ 0.4 seconds produced changes in the composition that were reflected in the EDX and RBS spectra. Typical RBS and EDX spectra are shown in figures 18 and 19 respectively. In order to study the uniformity of the depositions, several films were grown for EDX analysis with "predeposition" stages in which the process was run without activating the shutter, before the actual deposition started. The targets were sputter cleaned before starting the process. The total deposition time for each one of these films was ~20 minutes. Films grown with predeposition stages of 0, 20 and 40 minutes presented changes in composition, indicating that there are drifts in the sputtering rates during

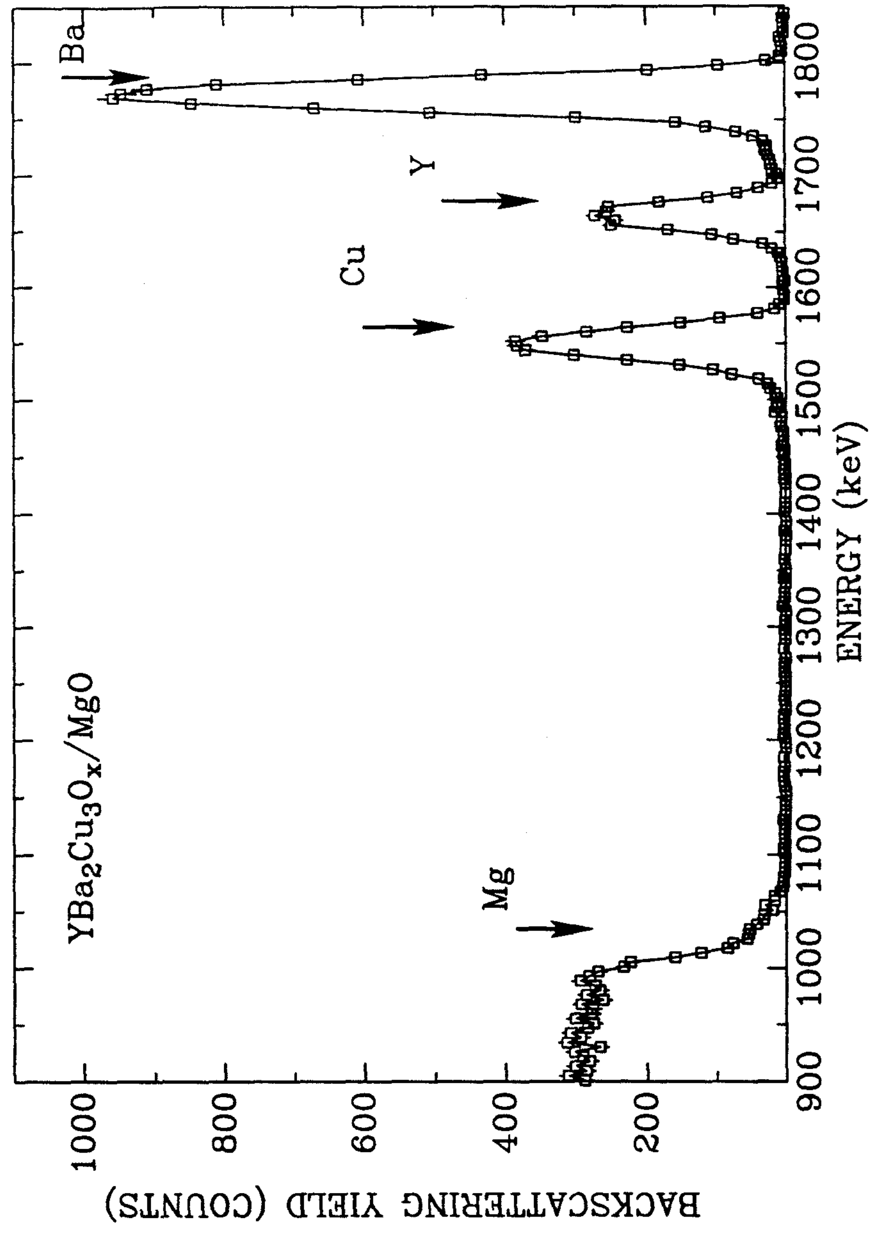

Fig. 18. Rutherford backscattering spectrum of a 290 Å film grown on MgO at Cu-plate temperature of 850°C. The spectrum was taken using 2 MeV He ions.

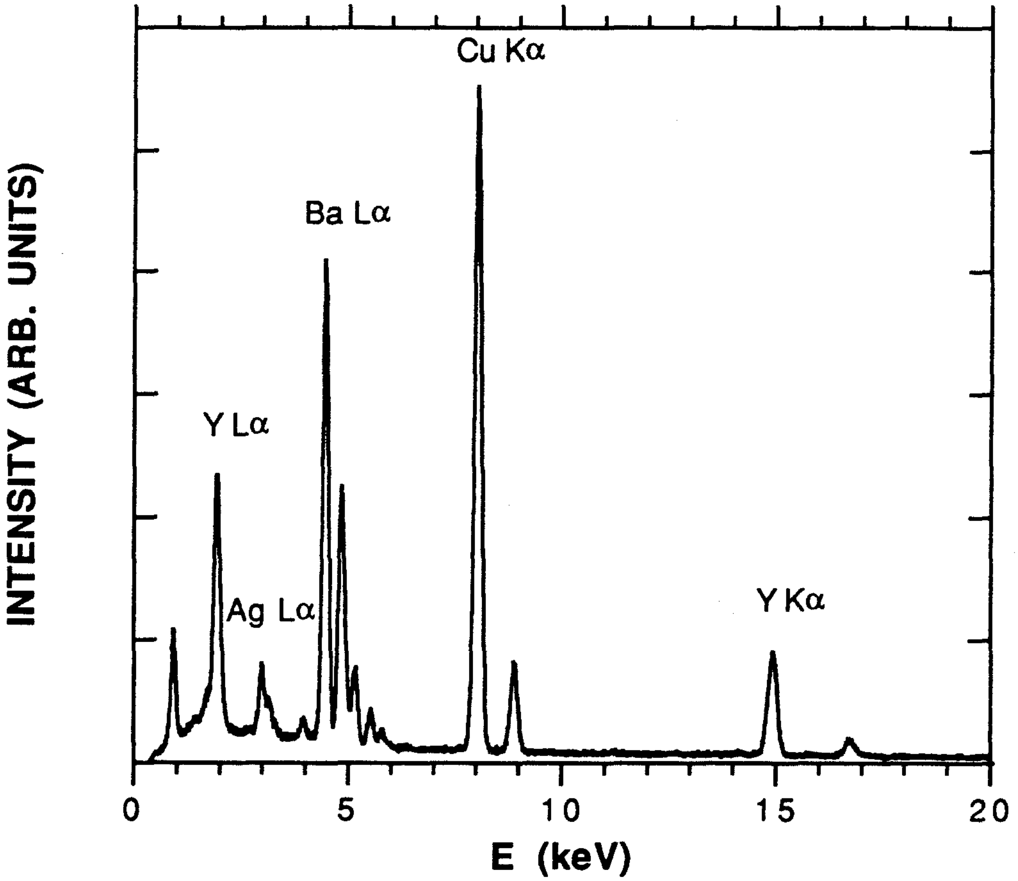

Fig. 19. Energy dispersive x-ray spectrum of a film grown on a carbon coated silver grid.

the first hour that the process is run. Films grown with predeposition stages from one hour to three hours had the same composition to within 5%, indicating that the process stabilizes after one hour. The total drift in cation ratios from the beginning of the deposition to the achievement of a steady state is ~10-15%. The uniformity of a 1650 Å film grown at room temperature, with a predeposition stage of one hour was also verified by RBS analysis, using 3 MeV He^+ ions (Fig. 20). In the spectrum from this film, a small signal corresponding to Ar trapped in the film (~ 1 atomic %) is observed. No evidence of Ar trapping was observed in films grown at the substrate temperatures used for *in-situ* growth. RBS and EDX analysis of many samples showed that compositions of films grown under the same conditions were reproducible, with the cation ratios being constant to within 5%. Most samples were grown within this range of the ideal "123" composition. The process becomes less reliable at the higher background oxygen pressures, due mainly to the oxidation of the targets. Comparison of RBS spectra for samples grown on MgO at different temperatures showed Cu losses (<10%) at the higher deposition temperatures. This was attributed to Cu evaporation from the film surface, and was easily compensated by changing the deposition parameters.

Thickness calibrations were done by measuring the total thickness of the films both by RBS and by cross-sectional transmission electron microscopy (XTEM). The average individual layer thickness was kept equal to one monolayer to within 10%.

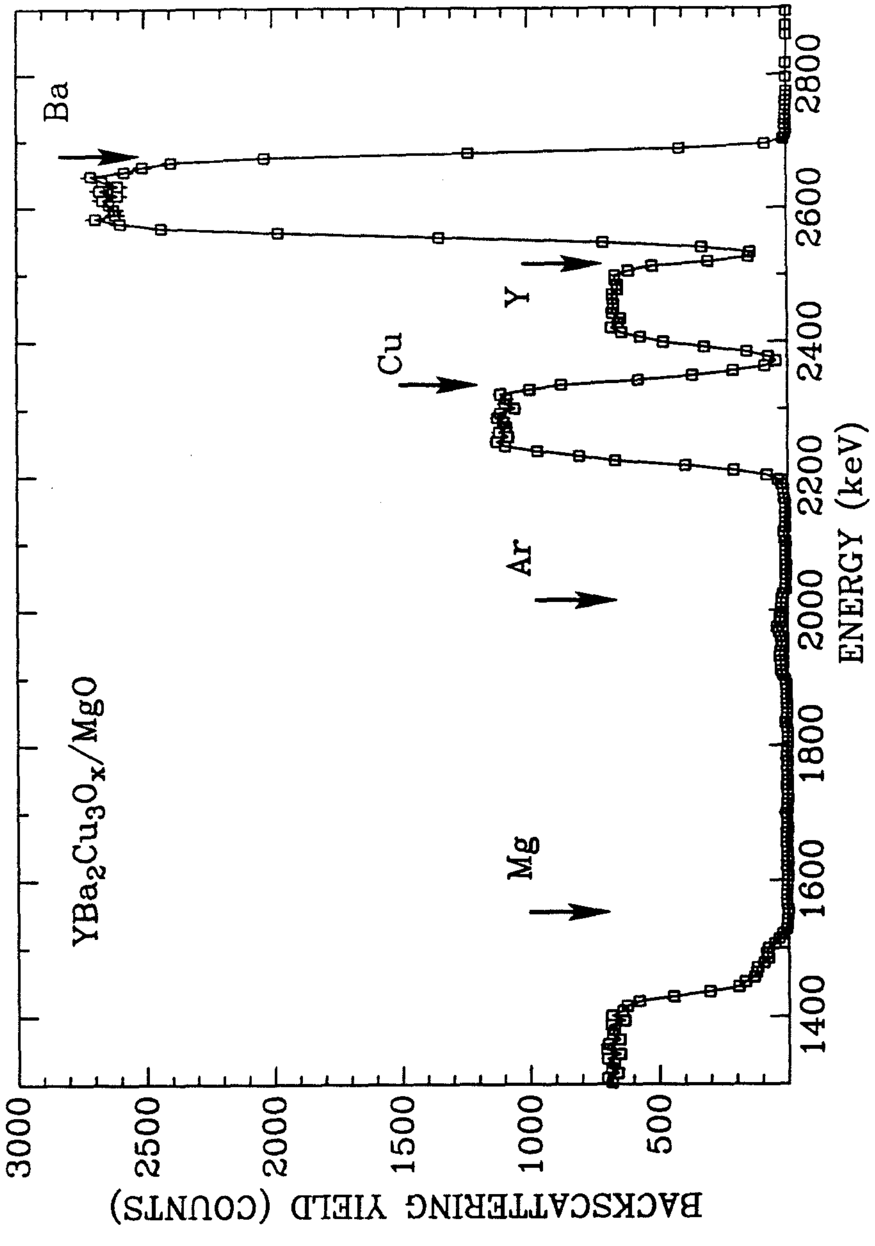

Fig. 20. Rutherford backscattering spectrum of a 1650 Å film grown at room temperature on MgO. The spectrum was taken using 3 MeV He ions.

4.3 Growth Temperature Range

Not all combinations of growth temperatures and oxygen pressures produced $YBa_2Cu_3O_{7-\delta}$ films. At a given partial pressure of oxygen there is a temperature window in which $YBa_2Cu_3O_{7-\delta}$ films can be grown. For a given oxygen pressure there is a growth temperature above which stoichiometric films contained multiple phases such as $BaCuO_2$, Cu_2O, etc. Films grown in a controlled background P_{O_2} of 2×10^{-4} Torr showed this phase separation at a Cu plate temperature of 800°C (the sample temperature was ~ 100°C lower). Films grown at the same oxygen pressure, at a Cu plate temperature of 700°C, were predominantly single phase $YBa_2Cu_3O_{7-\delta}$. Systematic studies of the thermodynamic equilibrium of the $YBa_2Cu_3O_{7-\delta}$ phase, show that at low oxygen pressures and high temperatures it is unstable and decomposes into several other oxides [Bormann and Nolting, 1989]. Our results are roughly consistent with the data on thermodynamic stability reported by Beyers and Ahn [Beyers and Ahn, 1991] and shown in Fig. 3.

At low temperatures, there is another constraint for the growth of $YBa_2Cu_3O_{7-\delta}$, given by the kinetics of nucleation and growth of this phase. Below a certain growth temperature (~550°C), the films were amorphous. One of the possible kinetic limitations to the formation of the "123" phase at low temperatures and low oxygen pressures is the incorporation of oxygen into the film during deposition. At low temperatures, this is limited by the kinetics of dissociation of the oxygen molecule at the film surface (this will be discussed in detail in section 4.6). This constraint is not present if the films are grown with a supply of activated oxygen species. This may explain the observation of growth of the "123" phase at lower temperatures by laser ablation, under activated oxygen species [Witanachchi et al., 1989]. Another possible kinetic constraint to the growth of "123" at low temperatures is given by the mobility of the cations.

The temperature window for growth of the "123" phase was studied by transmission electron microscopy on films grown in a controlled background oxygen pressure of 5×10^{-4} Torr. The films were grown directly into thinned, electron transparent substrates. The substrates used consisted of (001) Si with a buffer layer of SiO_2. The temperatures in these experiments were determined from a calibration done using an optical pyrometer. A good correlation was obtained between the fourth power of the absolute temperatures measured, and the heating power. This allowed extrapolations of the calibration to lower temperatures. In Fig. 21, we show four diffraction patterns corresponding to films grown at different temperatures. Films grown at 550°C were amorphous. The electron diffraction pattern showed diffuse rings characteristic of the amorphous structure (Fig. 21 (a)). Films grown at 600°C were polycrystalline $YBa_2Cu_3O_{7-\delta}$ with preferred c-axis orientation. This can be inferred from the plan-view electron diffraction pattern (Fig. 21 (b)), considering the relative intensities of the diffraction rings. The rings observed correspond to diffractions from lattice planes which are normal to the film surface.

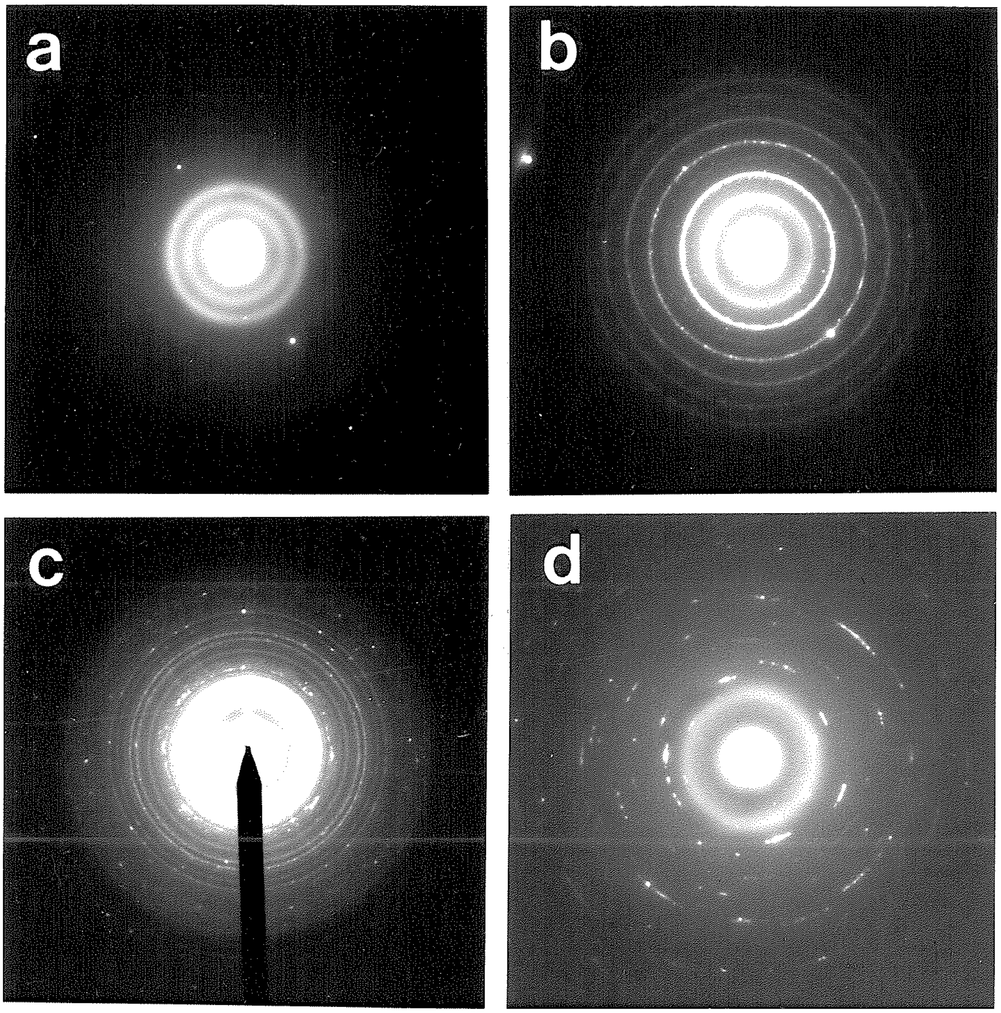

Fig. 21. Plan-view electron diffraction patterns of films grown on SiO_2/Si at (a) 550°C, (b) 600°C, (c) 650°C, and (d) 750°C.

The three strongest rings observed correspond (in increasing diameter) to the (103), (013) and (110) diffractions (first ring around central spot), to the (100), (010) and (003) diffractions (second strong ring), and to the (200), (020) and (006) diffractions (third strong ring). The contribution of the (00*l*) series can be estimated from the intensities of the superlattice diffractions which do not overlap with the (*h*00) or (0*k*0) diffractions. In particular the (005) diffraction is the strongest superlattice diffraction of the (00*l*) series. The weak intensity of the (005) ring observed in Fig. 21b, indicates that there is a much smaller fraction of a- or b-axis oriented grains (c-axis in plane) than c-axis oriented grains (c-axis normal to the film surface). This indicates that the orientations of the "123" grains are not completely random. The presence of the (103), (013), and (110) diffraction ring is attributed to a fraction of randomly oriented grains, since this is the strongest diffraction ring in randomly oriented "123". The main contributions to the diffraction pattern are seen to come from a fraction of randomly oriented grains, and a fraction of grains with c-axis orientation. The spot observed in the third strong ring in Fig. 21b, corresponds to the Si substrate (110) diffraction. The superposition of this spot with a diffraction ring from the "123" phase, illustrates the good lattice matching between these two phases, given by $a_{Si} \sim \sqrt{2}\, b_{\text{“}123\text{”}}$. A peculiar issue in the diffraction pattern was the absence of orthorhombic splitting, that persisted after annealing the TEM specimen at 400°C in 1 atm of oxygen. Films grown at 650°C were polycrystalline, and composed of several oxide phases excluding $YBa_2Cu_3O_{7-\delta}$, as indicated by the electron diffraction pattern (Fig. 21(c)). Films grown at 750°C consisted of Cu_2O grains of about

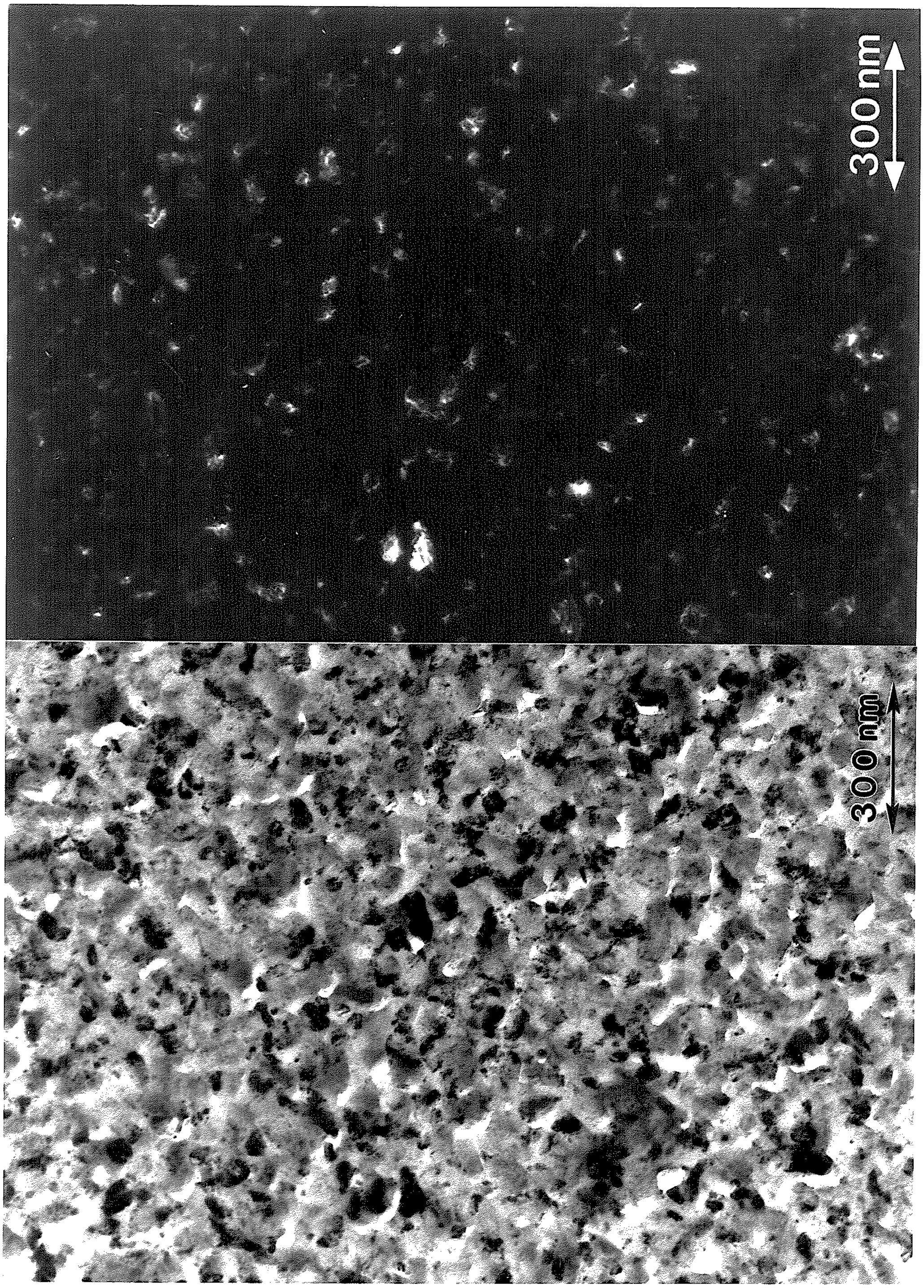

Fig. 22. Bright field (left) and dark field (right) plan-view transmission electron micrographs of a $YBa_2Cu_3O_{7-\delta}$ film grown on SiO_2/Si at 600°C.

1 μm, in an amorphous matrix (the diffraction pattern is shown in Fig. 21 (d)). These results are consistent with the results obtained for films grown on MgO and $SrTiO_3$ substrates, and with the studies on the stability of the "123" phase [Beyers and Ahn, 1991]. In Fig. 22 we show bright field and dark field micrographs of an $YBa_2Cu_3O_{7-\delta}$ film grown on SiO_2/Si at 600°C. The film is polycrystalline, with a grain size of ~500 Å.

4.4 Properties and Microstructure of Films Grown on MgO and on $SrTiO_3$ Substrates

Epitaxial, c-axis oriented (c-axis normal to the film surface) $YBa_2Cu_3O_{7-\delta}$ films were grown on (001) $SrTiO_3$ and on (001) MgO substrates at temperatures ranging from 550 to 750°C. Figure 23 shows the x-ray diffraction patterns of typical films, showing c-axis orientation. The films were predominantly single phase, and predominantly c-axis oriented, as was confirmed by transmission electron microscopy.

The film surfaces were smoother and the film-substrate interfaces were sharper than those typically found in films grown by three step processes. This is shown in a cross-sectional TEM micrograph of a 300 Å film grown on MgO (Fig. 24). The lattice fringes observed in Fig. 24 correspond to the c-axis planes of the "123" phase. The surfaces of films

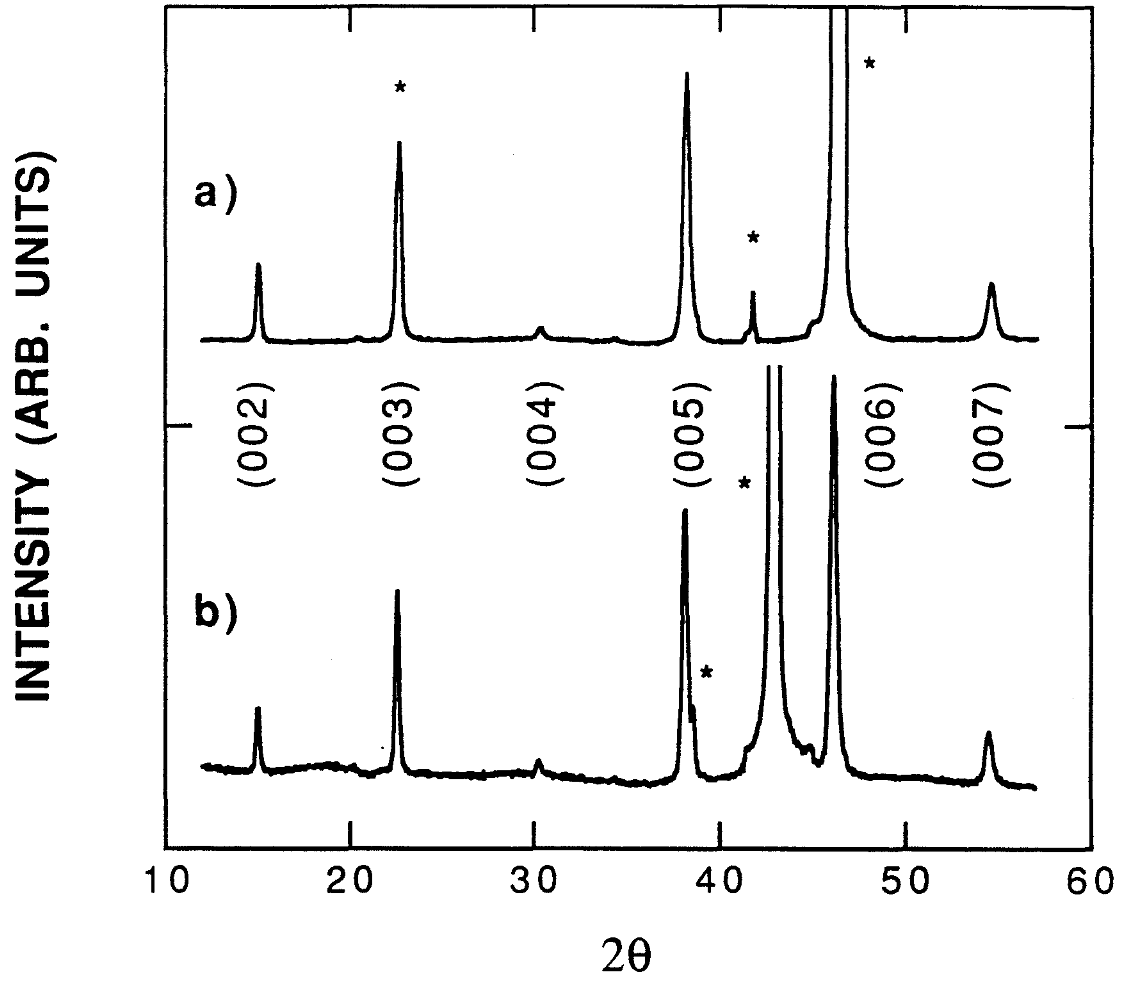

Fig. 23. X-ray diffraction patterns of films grown on (a) $SrTiO_3$ and (b) MgO, showing c-axis orientation. The patterns were taken using Cu radiation. Peaks with substrate components are marked with an asterisk.

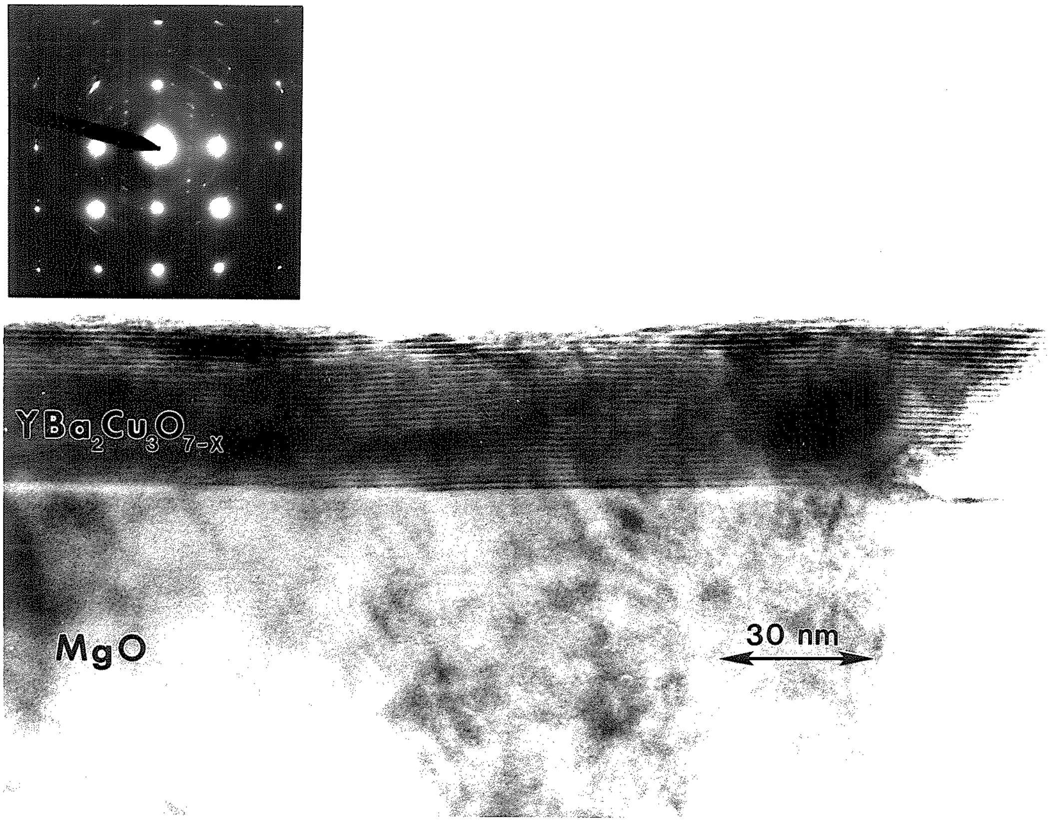

Fig. 24. Cross-sectional TEM view of a $YBa_2Cu_3O_{7-x}$ film grown *in-situ* on MgO. The inset shows the electron diffraction pattern. A small misorientation between the film c-direction and the substrate [001] (surface normal) direction is observed in the diffraction pattern.

were also investigated by Scanning Electron Microscopy. We observed surface imperfections consisting of grains of ~ 1 μm (Fig. 25). EDX analysis showed that the grains were Cu-Ba rich with respect to the matrix.

Some samples showed peaks in the x-ray diffraction patterns corresponding to second phases, at 4.08Å and 2.04Å. These were found in Cu deficient films grown at high deposition temperatures. Some samples grown without enhancement of the local oxygen pressure showed impurity phase peaks at 3.15Å and at 1.58Å. These peaks were not observed after annealing the samples in O_2 at 400°C. The determination of the second phases present in these films was prevented by the complexity of the phase diagram of the Y-Ba-Cu-O system, which has not been fully investigated. Furthermore, many of the phases in this diagram have diffraction patterns with the strongest peaks at the same d-spacings. This and the possibility of texturing (preferred orientations) prevents an unambiguous phase identification from the θ-2θ x-ray diffraction data.

High resolution cross-sectional TEM analysis was performed, particularly on films with expanded c-lattice parameters, to investigate the presence of stacking faults. In figures 26 and 27, we show high resolution TEM cross sections of a film grown on MgO. The three perovskite-like units that constitute the "123" unit cell are resolved along the c-direction. The film had a c-axis lattice parameter of 11.85 Å, as determined by x-ray diffraction. The two figures correspond to two different values of defocus. The TEM specimen analyzed did not have a uniform thickness, and was

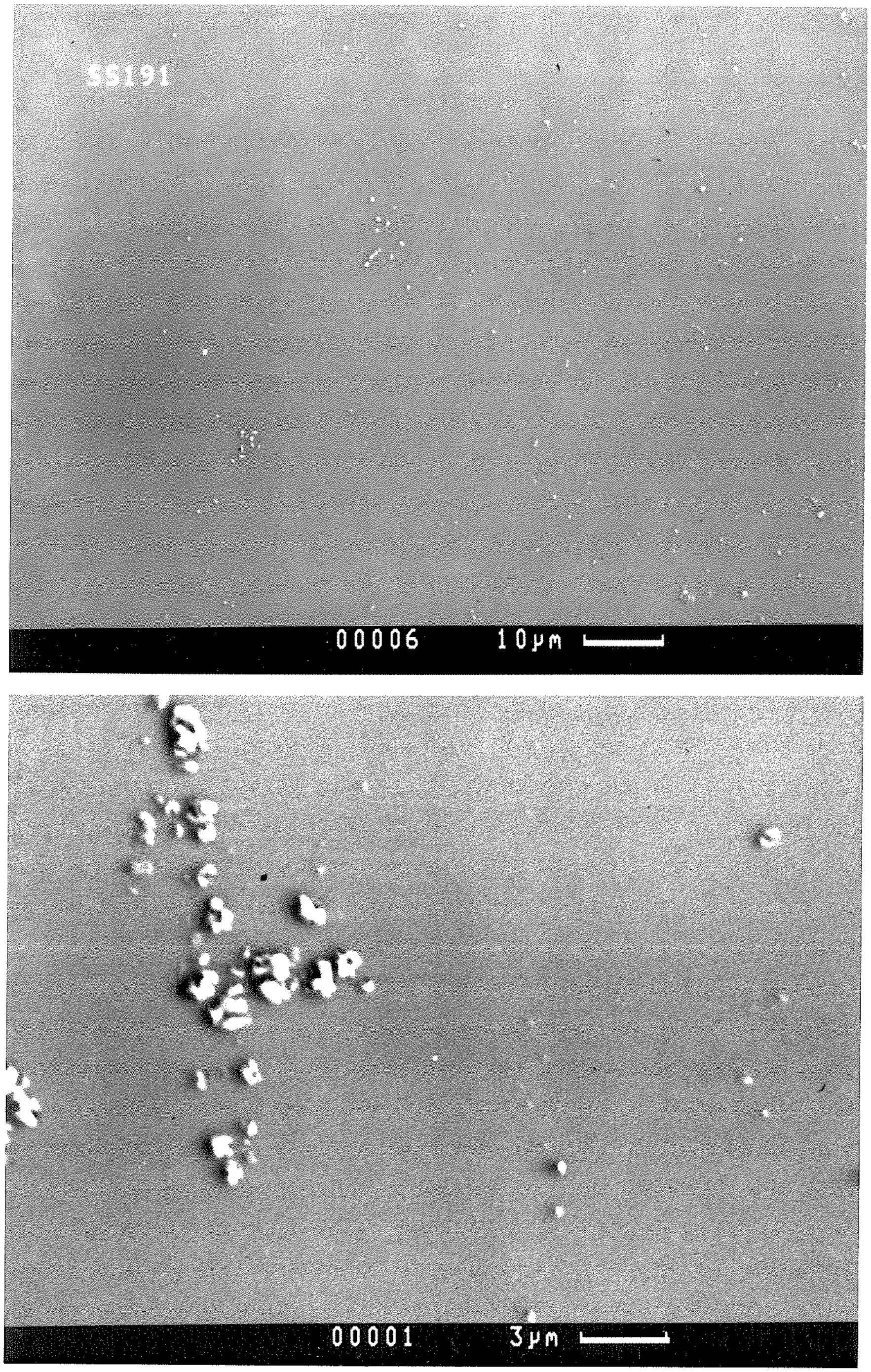

Fig. 25. Scanning electron micrographs of a stoichiometric YBa$_2$Cu$_3$O$_{7-\delta}$ film grown on MgO. The ~1μm grains observed correspond to a Cu and Ba rich second phase.

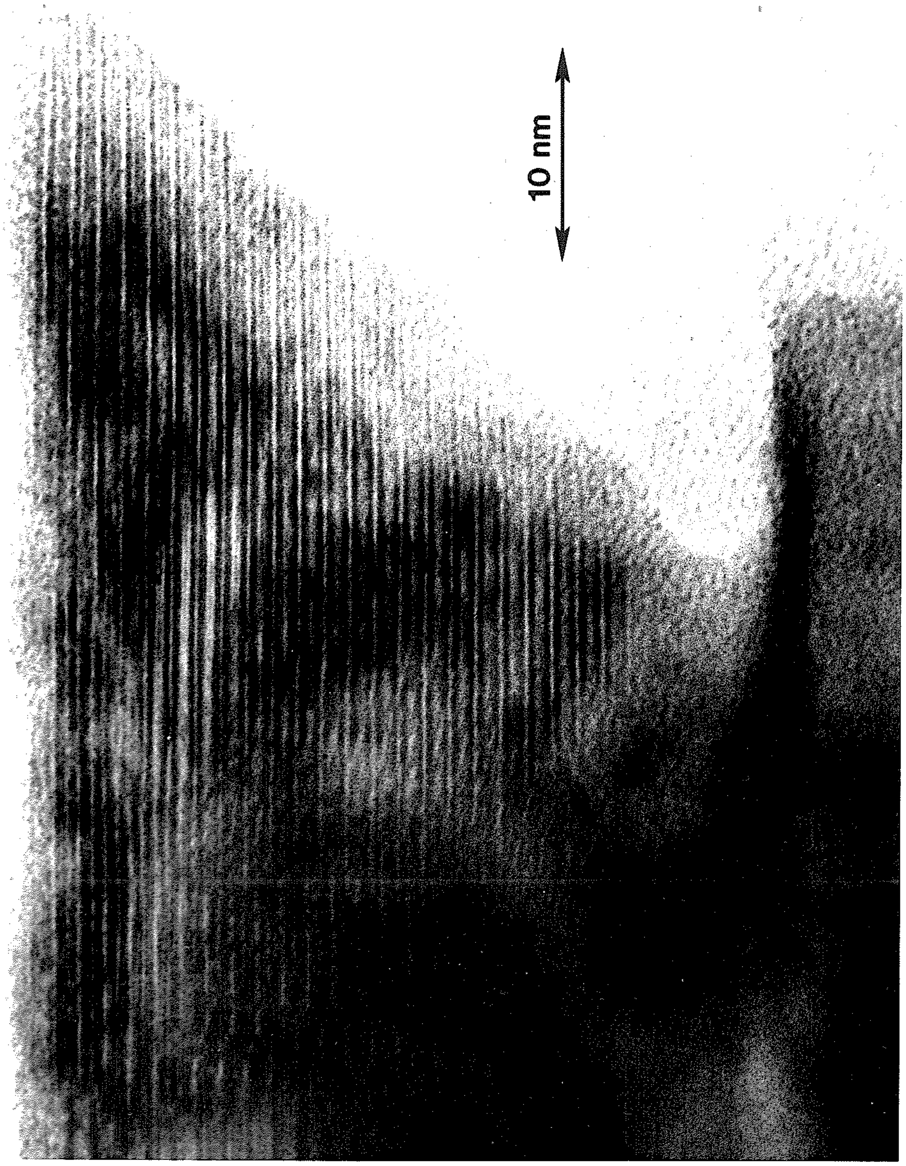

Fig. 26. High resolution cross-sectional TEM view of a film grown on MgO. The lattice fringes observed correspond to the planes normal to the c-direction. The c-axis lattice parameter of the film is 11.85 Å.

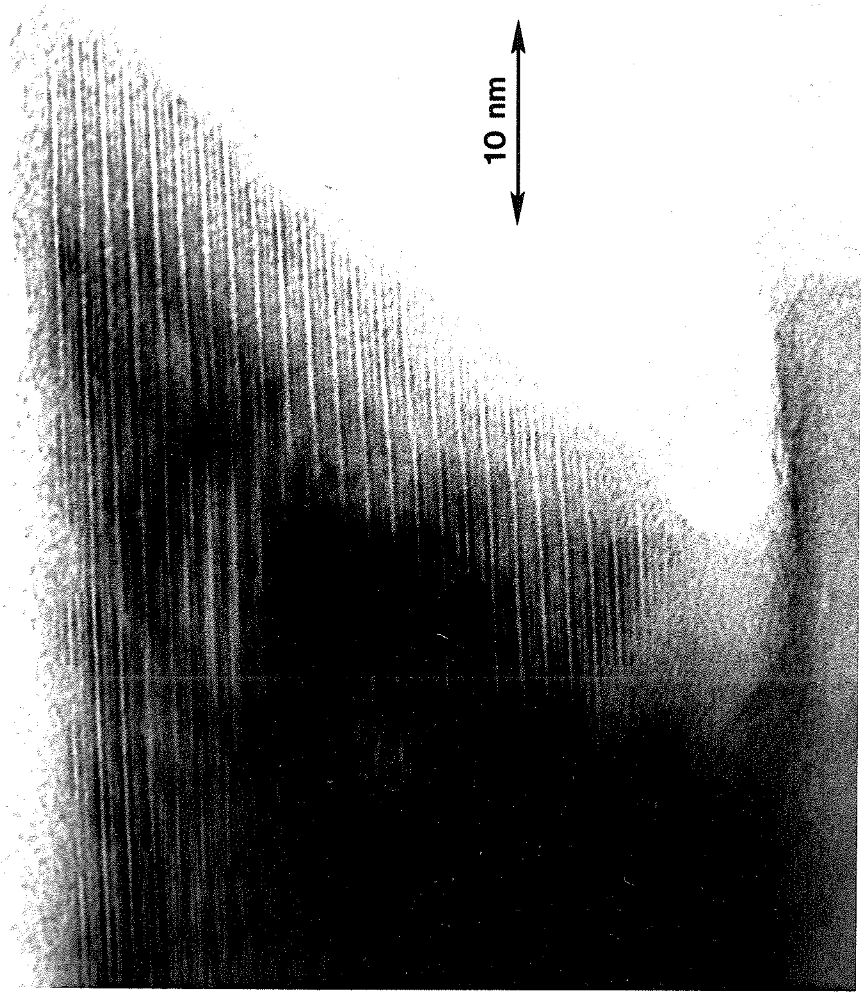

Fig. 27. High resolution cross-sectional TEM view of a film grown on MgO. The lattice fringes observed correspond to the planes normal to the c-direction. The c-axis lattice parameter of the film is 11.85 Å.

thinner close to the region were it cracked during the preparation procedure (right side of the pictures). In this region, the lattice images are easy to interpret, and show a perfect stacking sequence. Image simulations showed a strong effect of thickness on the contrast, including contrast reversal. This impedes a simple interpretation of the lattice images for other regions of the pictures.

Most of the films grown on (001) $SrTiO_3$ substrates, were epitaxial, c-axis oriented, with the $YBa_2Cu_3O_{7-\delta}$ [100] direction parallel to the substrate [100] or [010] direction. In Fig. 28 we show a plan-view TEM micrograph of a film grown on $SrTiO_3$. A Moire pattern of spacing ~300 Å is observed. The Moire pattern arises from the lattice mismatch between the film and the substrate. The pattern observed corresponds to a film in-plane lattice constant of ~3.85 Å. This indicates that the film is epitaxial (meaning by this that there is a specific orientation relation between substrate and film), and that it has relaxed (it has a lattice parameter different than that of the substrate). Diffraction patterns taken from plan-view samples did not show the spots corresponding to the "123" phase. This is a consequence of the small lattice mismatch between the "123" a- or b-axis lattice constants and the substrate lattice constant, and indicates the perfect orientation relation between the film and the substrate. Fig. 28 also shows that there were coherent precipitates, of about 300 Å, present in the film. EDX analysis showed that these were Y rich with respect to the matrix. The Moire pattern spacing indicates that there is a large lattice parameter difference between this second phase and the substrate or the "123" phase.

Fig. 28. Plan-view TEM of a film grown on $SrTiO_3$. The Moire pattern of spacing ~300 Å, corresponds to the lattice mismatch between the substrate and c-axis oriented $YBa_2Cu_3O_{7-\delta}$. The arrow points to a coherent precipitate.

Weak spots were observed in the diffraction patterns, corresponding to this phase. The in-plane lattice parameter for this impurity phase is estimated to be ~4.2-4.3 Å. This phase was also observed in films grown on other substrates.

In contrast to what is observed in films grown on $SrTiO_3$, there is a more complicated grain structure in films grown on (001) MgO substrates. The films are mainly c-axis oriented, but present several in-plane orientations, resulting in low and high angle grain boundaries. Our results are consistent with the more systematic studies reported by Ravi et al. [Ravi et al., 1990]. These indicate that in MgO substrates, despite the large lattice mismatch (9%), the c-axis oriented films still tend to grow with the [100] $YBa_2Cu_3O_{7-\delta}$ direction parallel to the substrate [100] or [010] direction. In the cross-sectional TEM micrograph shown in Fig. 24, we included a diffraction pattern, that shows a misorientation between the c-axis of the film and the MgO substrate [001] direction, of ~3°. Plan-view studies also showed the presence of low-angle grain boundaries, twin boundaries and a few high angle grain boundaries in the films. The specimens analyzed consisted generally of several c-axis oriented grains. The diffraction patterns showed the orientations of the grains to be similar, indicating that the grain boundaries observed corresponded either to twin or to low angle grain boundaries. The grains had typically rectangular shapes, with sizes in the order of 0.5 × 2 μm for films grown at sample holder temperatures of 730°C, and of 1 × 4 μm for films grown at sample holder temperatures of 780°C. In cross section micrographs, the grain boundaries observed

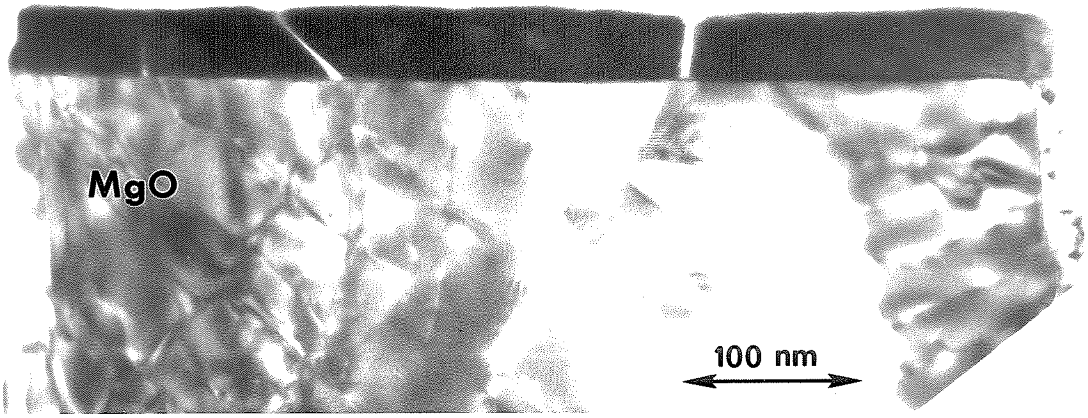

Fig. 29. Cross-sectional TEM of a film grown on MgO, showing that the film is composed of c-axis oriented grains. The film has cracked along the grain boundaries.

were approximately normal to the film surface, or forming approximately a 45° angle with it (Fig. 29). In Fig. 29, the film seems to be discontinuous at the boundaries. This is possibly a result of the preparation technique for TEM analysis, which involves crushing pieces of the samples with a pistol and mortar. In plan-view samples, the shapes of the pieces investigated suggested that the samples had cracked along grain boundaries. This was further supported by evidence found in a plan-view sample in which a crack was seen along a grain boundary, with the corresponding grains attached to each other only on one section of it.

A film grown on $SrTiO_3$ with an unusually large number of grains with the c-axis oriented in the plane of the substrate, was investigated by TEM plan-view analysis. The film was grown at 650°C (Cu plate temperature of 750°C), in a controlled oxygen partial pressure of 5×10^{-4} Torr. In this study, we found several c-axis in-plane orientations. We observed grains having the c-axis parallel to the [010], [100], [110], and $[1\bar{1}0]$ substrate directions. In Fig. 30, a plan-view TEM, we show two grains with the c-axis in the plane of the substrate, making a 45° angle. The lattice fringes observed correspond to the c-spacing of $YBa_2Cu_3O_{7-\delta}$. The diffraction pattern in Fig. 30 shows the different epitaxial c-axis in plane orientations. The diagonal directions in the inset of Fig. 30 correspond to the substrate [100] and [010] directions. The spots at small spacings correspond to the c-direction of "123". The spacing of the "123" spots is approximately 1/3 of the spacing of the substrate spots along the diagonal directions, corresponding to the relation $a_{SrTiO_3} \sim 1/3\ c_{YBa_2Cu_3O_{7-\delta}}$. The

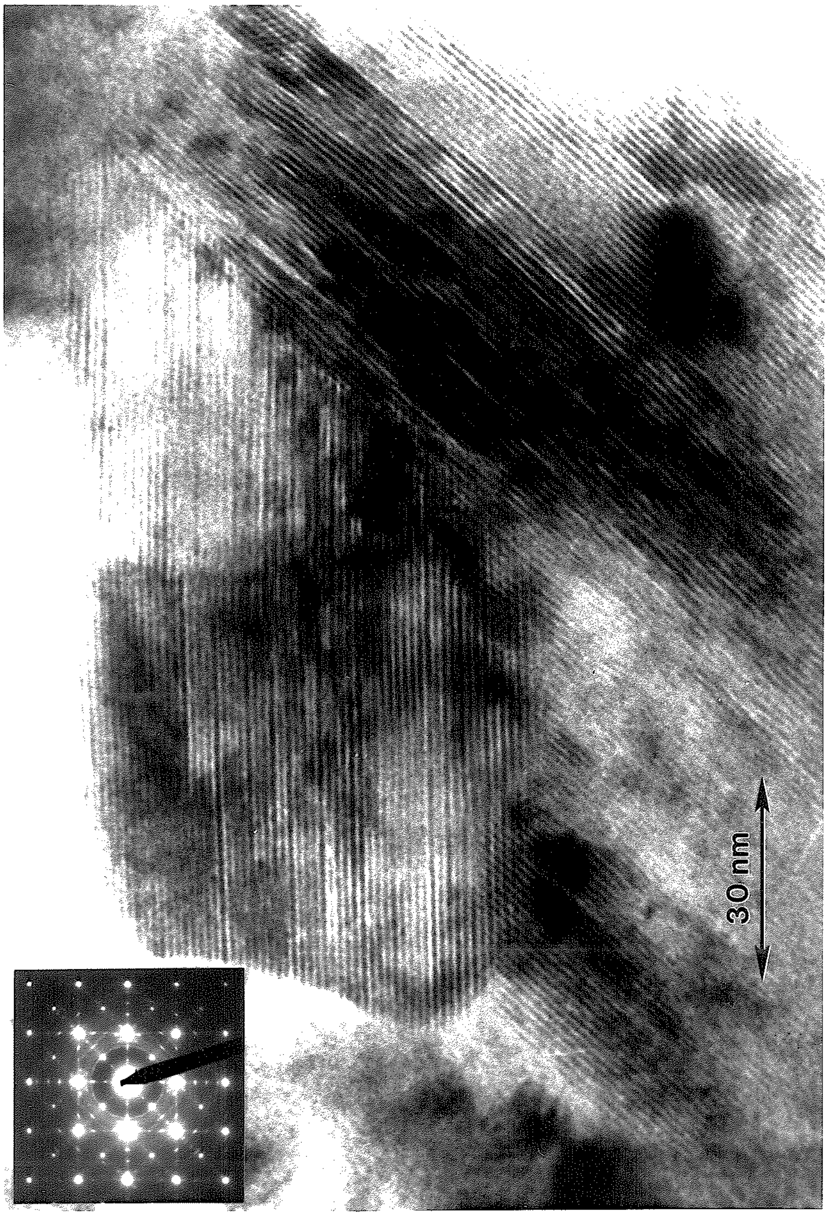

Fig. 30. Plan-view TEM of a film grown on $SrTiO_3$, showing two grains with the c-directions oriented in the plane of the substrate, making a 45° angle. The inset shows the electron diffraction pattern, with the different c-axis in-plane epitaxial orientations.

spacing of the "123" spots is approximately 2/9 of the spacing of the substrate spots along the horizontal or vertical directions, corresponding to the relation 9 $a_{SrTiO3} \sim 2\sqrt{2}\, c_{YBa2Cu3O7-\delta}$. In Fig. 31, we show a plan-view TEM that includes the four orientations with the c-axis in plane observed in the film. The fraction of grains with the c-axis parallel either to the [110], or the $[1\bar{1}0]$ substrate directions was about 20%. This fraction is large compared to what is usually found for films grown on $SrTiO_3$ [Eom et al., 1990a]. A possible explanation of this fact is that the film investigated had an expanded c-axis lattice parameter. The c-axis lattice expansion, improves the lattice matching with the substrate for orientations in which the c-axis is parallel to the substrate [110] or $[1\bar{1}0]$ directions, and deteriorates the matching for the standard orientations (c-axis parallel to [100] or [010] substrate directions). Geometrical arguments, based on lattice matching have been successfully used to account for the epitaxial orientations of "123" films on MgO substrates [Hwang et al., 1990]. From x-ray studies the c-axis lattice parameter was determined to be 11.93 Å for grains with c-axis normal to the film surface. It is reasonable to assume, according to off-axis x-ray diffraction studies [Eom et al., 1989, 1990a], that the in-plane c-lattice parameter is similarly expanded. Using the corresponding thermal expansion coefficients, and the oxygen pressure dependence of the c-lattice constant, we estimated the lattice mismatch between the film and the substrate along the "123" c-direction for the two types of orientations, at the deposition conditions. For the standard orientation ("123" c-direction along substrate [100] direction) the lattice mismatch was ~3.6%, and for the second orientation ("123" c-direction

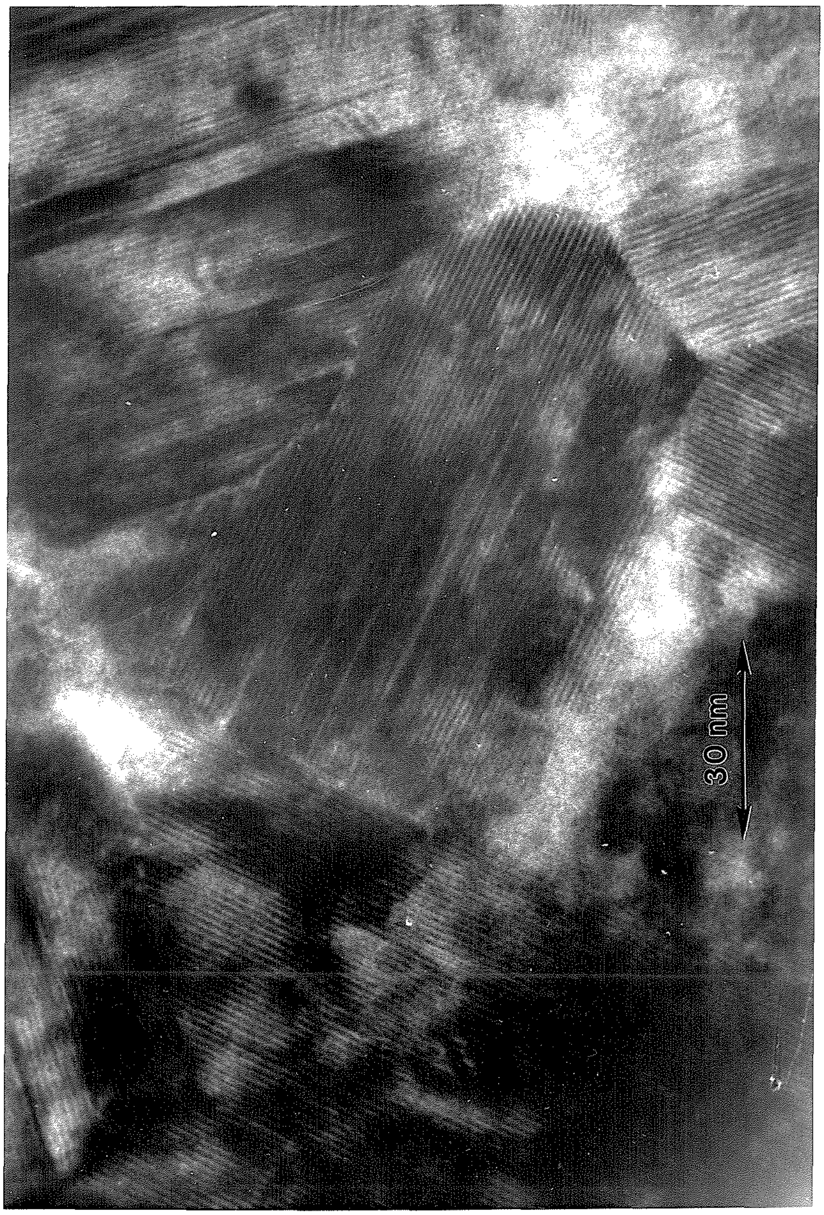

Fig. 31. Plan-view TEM of a film grown on $SrTiO_3$, showing the four more common c-axis in-plane orientations.

along substrate [110] direction) the lattice mismatch was ~2.2%. These results are relevant in the growth of a-axis oriented films, which has been the focus of considerable attention recently [Ramesh et al., 1990, Eom et al., 1990a, Inam et al., 1990].

Resistivity measurements were done by the standard AC four point technique. The highest transition temperature obtained is $T_c(R=0)=79$ K for a film grown on $SrTiO_3$. Superconducting transitions were obtained over a range of compositions, including films as far off stoichiometry as $Y_1Ba_{2.5}Cu_{4.0}O_{7-\delta}$ (Fig. 32). SEM analysis of these off stoichiometric films showed the presence of a larger amount of Ba-Cu rich grains than in stoichiometric films. The typical size of these grains was about 1 μm for films grown at 675°C (Fig. 33). In images obtained from secondary electrons, a difference in contrast was observed between the region surrounding the second phase grains, and the rest of the film. This indicates the presence of a depletion region surrounding these grains.

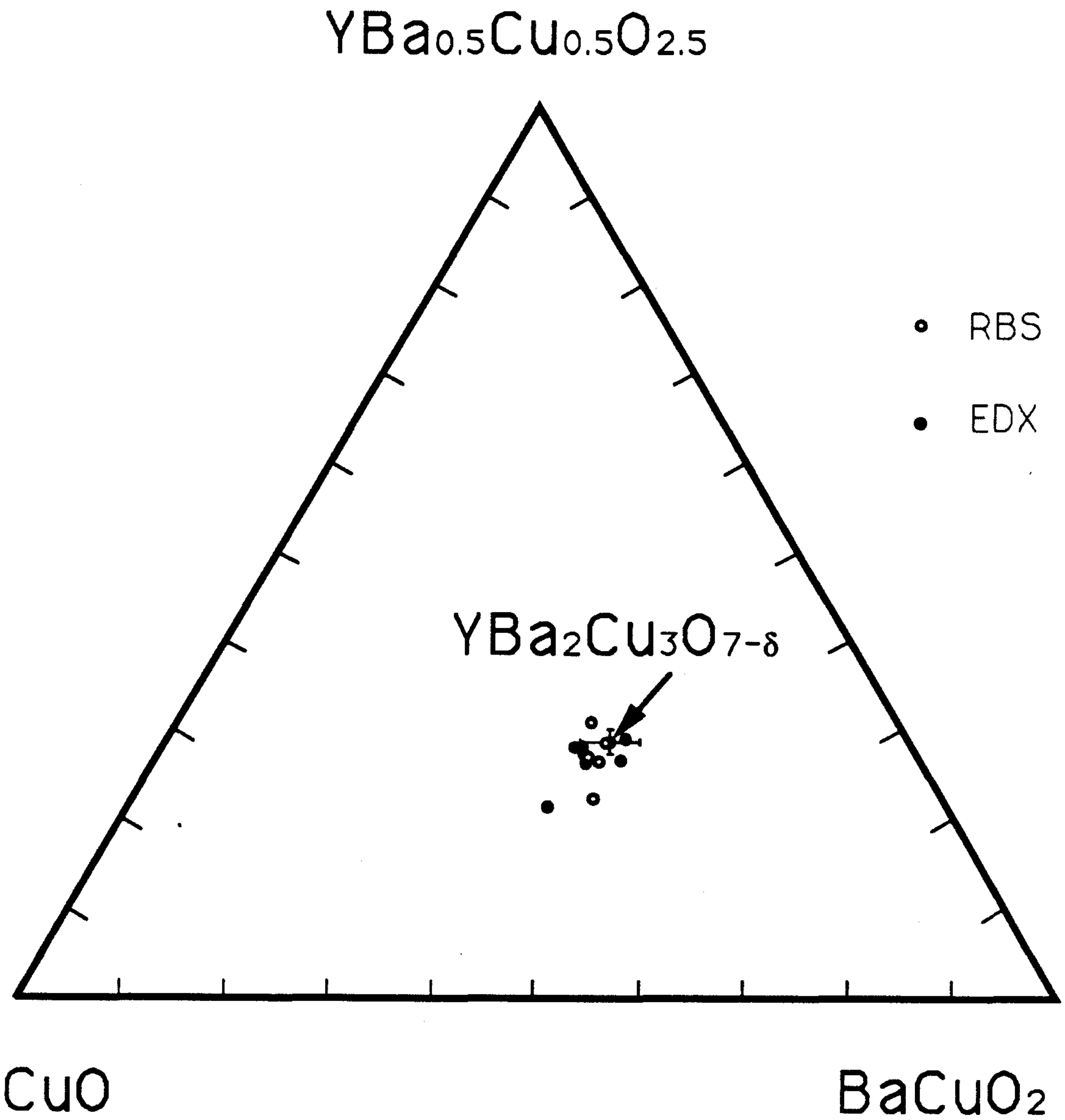

Fig. 32. Plot of compositions of superconducting films. The arrow points at the ideal $YBa_2Cu_3O_{7-\delta}$ composition. The error bars correspond to 5% departures from the ideal composition.

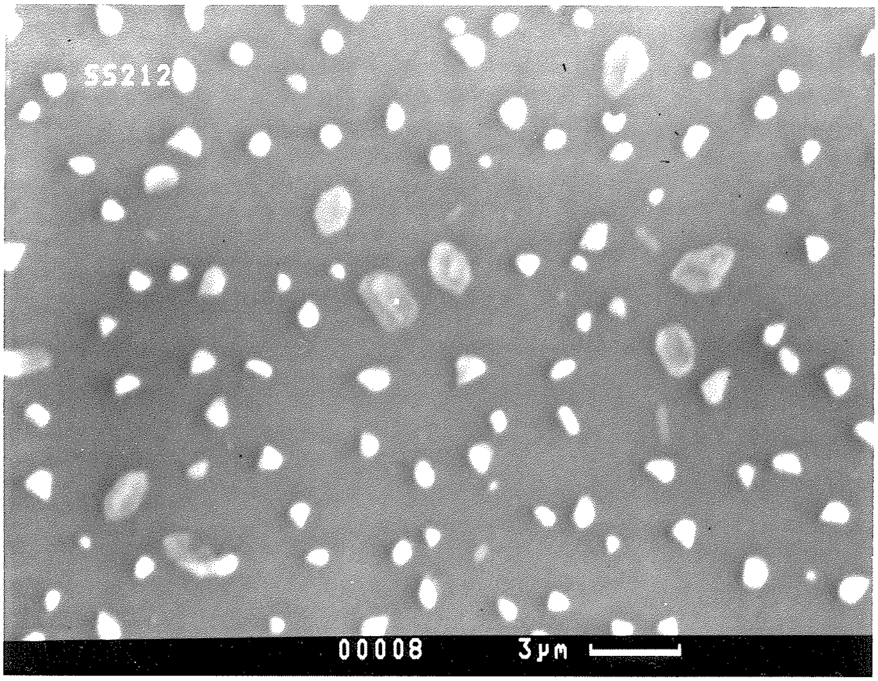

Fig. 33. Scanning electron micrograph of an off-stoichiometry film grown on MgO. The film is Ba and Cu rich.

4.5 Correlations Between C-Axis Lattice Distortions and Superconducting Properties

The *in situ* growth of $YBa_2Cu_3O_{7-\delta}$ films has raised a set of new issues not previously encountered in bulk samples or films obtained by high temperature post deposition anneals. One of the special characteristics often seen in *in situ* grown films is the expansion of the c-axis lattice parameter relative to the bulk value of 11.68 Å [Hellman et al., 1989; Eom et al., 1989; Berkley et al., 1988]. Early interpretations associated this expansion to a chain-site oxygen deficiency in the films by analogy to the well known expansion of the c-axis lattice parameter in oxygen deficient bulk samples. However, it was soon recognized that the properties of *in situ* grown films with a given lattice parameter were intrinsically different from those of an oxygen deficient bulk sample with the same lattice parameter [Hellman et al., 1989, Eom et al., 1989]. An important characteristic of the *in situ* grown films with expanded c-axis lattice parameter is their behavior under heat treatments in oxygen. Contrary to what is observed in bulk samples, the lattice parameter of the films cannot be reduced by anneals in oxygen at low temperatures ($T<650°C$) [Hellman et al., 1989, Eom et al., 1989].

We have analyzed epitaxial, c-axis oriented $YBa_2Cu_3O_{7-\delta}$ thin films grown *in situ* by sequential ion beam sputtering on (001) $SrTiO_3$ and (001) MgO substrates, studying the lattice distortions along the c-direction and their correlations to characteristics of the superconducting transitions [Kittl et al., 1990b, 1991a]. X-ray diffraction studies showed the presence of both homogeneous and inhomogeneous lattice distortions along the c-direction. The films had expanded c-axis lattice parameters. The x-ray data also showed a broadening of the *(00l)* Bragg reflections which can be correlated to the expansion of the c-axis lattice parameter. The broadening of the *(00l)* x-ray lines was analyzed for several orders of diffraction. This analysis showed that stacking faults are not an important cause of the broadening. The "size" and "inhomogeneous lattice distortions" contributions to the broadening were evaluated. The size coefficients were consistent with the film thicknesses. The broadening of the *(00l)* Bragg peaks in excess of the broadening due to finite film thickness was found to be due to inhomogeneous lattice distortions. The overall trend in the data shows an increase of the inhomogeneous strains with the enlargement of the c-axis lattice parameter. The inhomogeneous lattice distortions are interpreted as fluctuations in the c-axis lattice parameter.

The resistive transitions were found to be correlated to the lattice distortions. The transition temperatures were found to decrease with the enlargement of the c-axis lattice parameter. The resistive transitions were found to be wider for higher values of the inhomogeneous lattice distortion coefficient. We show correlations between the midpoint Tc and the c-axis lattice parameter and between the transition widths and the inhomogeneous lattice distortions.

X-ray diffraction θ–2θ spectra were taken with a Siemens D500 diffractometer in a high resolution geometry, using CuKα radiation. The x-ray scans were corrected for Kα and instrumental broadening. The c-axis lattice parameters were evaluated by high angle extrapolations using the (00*l*) series. The films had c-axis lattice parameters ranging from 11.72 to 12.00 Å. In contrast, the lattice parameter of fully oxygenated bulk samples or films grown by post-deposition anneal in O_2 at 850°C is 11.68 Å. Anneals in O_2 at low temperatures ($T < 650°C$) had little or no effect on the lattice parameter, producing changes in the c-axis lattice parameter of < 0.02 Å, and producing no significant changes in the superconducting transitions. Anneals in O_2 at 850°C followed by anneals at 400°C were effective in reducing the lattice parameter to approximately the bulk value of 11.68 Å. Similar results have been reported for other *in situ* techniques [Hellman et al., 1989, Eom et al., 1989].

The full widths at half maximum of the (*00l*) Bragg peaks, ΔK, were plotted in reciprocal space as a function of their K values. The plots show a monotonic increase of ΔK with K. Fig. 34 shows the plots for several films grown on MgO with different c-axis lattice parameters. The contributions to line broadening due to finite size and to inhomogeneous lattice distortions were evaluated by least square fits assuming particular peak shapes for each contribution, and using the expressions (2.5.2) and (2.5.3). The best fits were obtained in most cases assuming Cauchy size broadening and Gaussian lattice distortions broadening. The values of crystal size obtained were consistent with the film thicknesses as measured by

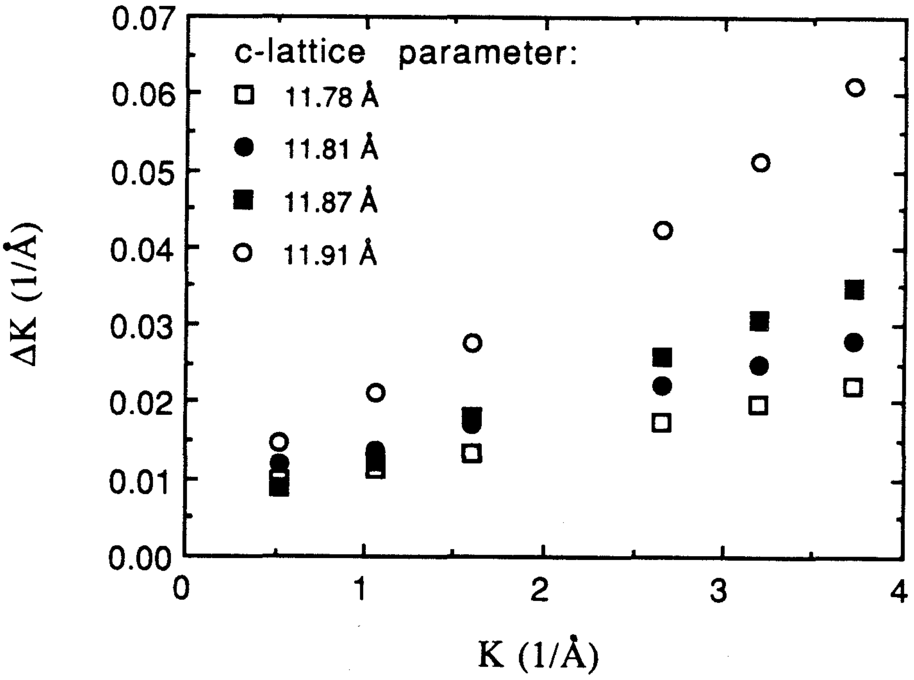

Fig. 34. Full widths at half maximum of the (00*l*) x-ray Bragg peaks ΔK, as a function of their K values, for several films grown on MgO. The data was corrected for Kα and instrumental broadening.

Rutherford backscattering spectrometry and by cross-sectional transmission electron microscopy. Fig. 35 shows a plot of the inhomogeneous strains, ϵ_{rms}, as a function of the c-axis lattice parameter. The error bars were evaluated by assuming Cauchy-Cauchy and Gaussian-Gaussian peak profiles. There is an overall tendency for films with larger c-axis lattice parameters to present higher inhomogeneous lattice distortions.

Comparison of the x-ray spectra for films before and after annealing in O_2 at 400°C showed no change in the widths and positions of the *(00l)* Bragg peaks. Films annealed at 850°C in O_2 showed a sharpening of the *(00l)* Bragg peaks and a shift to the bulk "123" lattice constant, indicating a relaxation of the strains (Fig. 35).

Resistivity measurements were done by the standard AC four point technique. Figure 36 shows the resistive transitions for (a) a 1000 Å film grown on $SrTiO_3$ at 750°C; and for 400 Å films grown on MgO at temperatures of (b) 675°C and (c) 630°C. The background P_{O_2} was 1×10^{-3} Torr for film (a) and 1×10^{-4} Torr for films (b) and (c). The c-axis lattice parameters were (a) 11.72 Å, (b) 11.77 Å and (c) 11.87 Å. For optimum films, the transition temperatures were found to decrease with increasing lattice parameter. Figure 37 shows a plot of the transition temperatures (midpoints) as a function of the c-axis lattice parameter. The tendency of Tc to decrease with the expansion of the c-axis lattice parameter was found to hold for a wide range of lattice parameters.

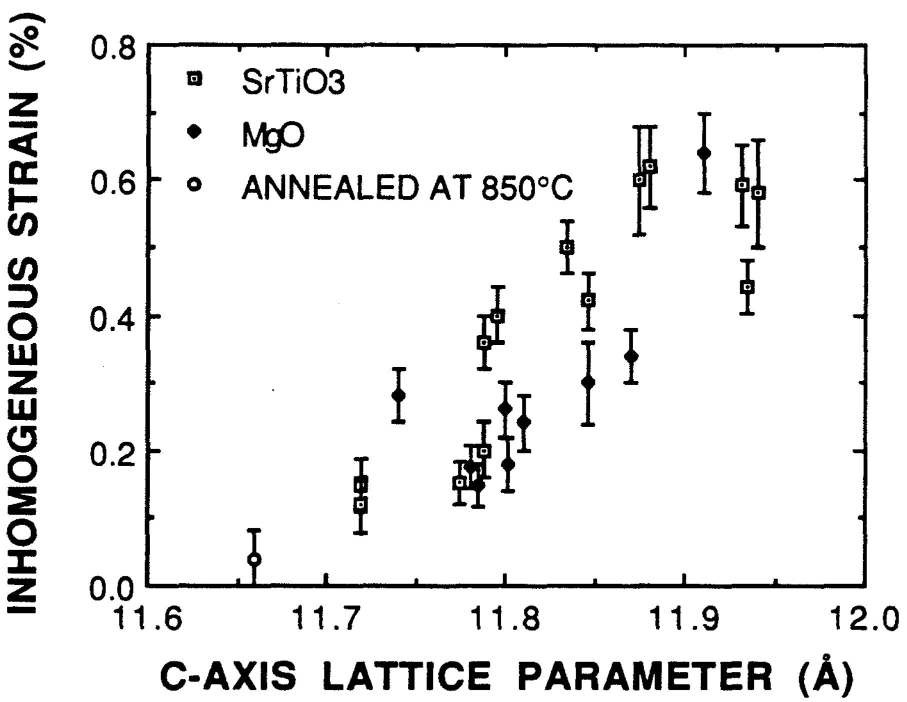

Fig. 35. Inhomogeneous strains ϵ_{rms}, as a function of the c-axis lattice parameter.

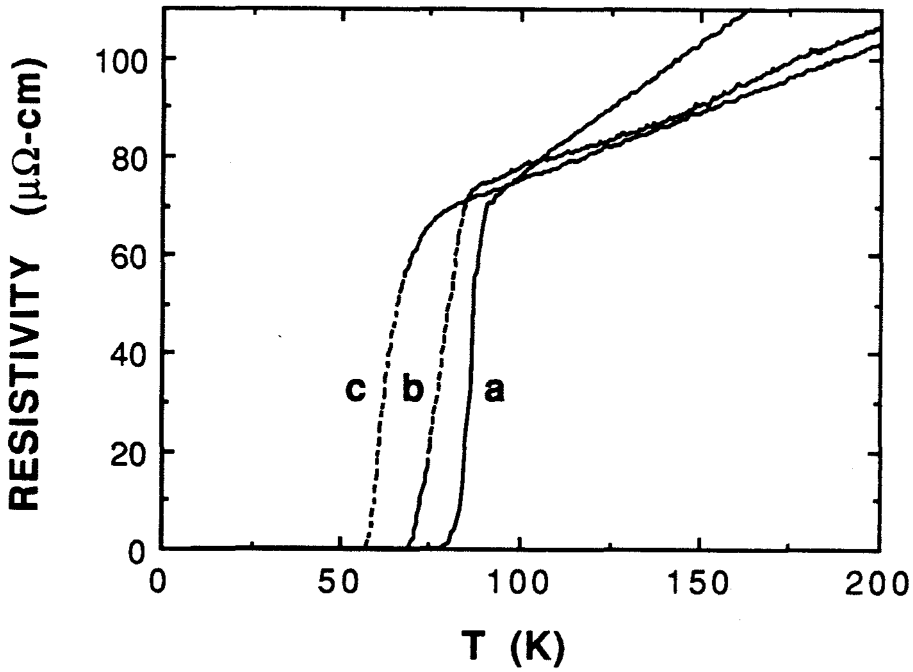

Fig. 36. Resistivity vs temperature for (a) 1000 Å film grown on $SrTiO_3$ with a c-axis lattice parameter of 11.72 Å; and 400 Å films grown on MgO with c-axis lattice parameters of (b) 11.77 Å, and (c) 11.87 Å. The films were grown at sample holder temperatures of (a) 850°C, (b) 775°C, and (c) 730°C.

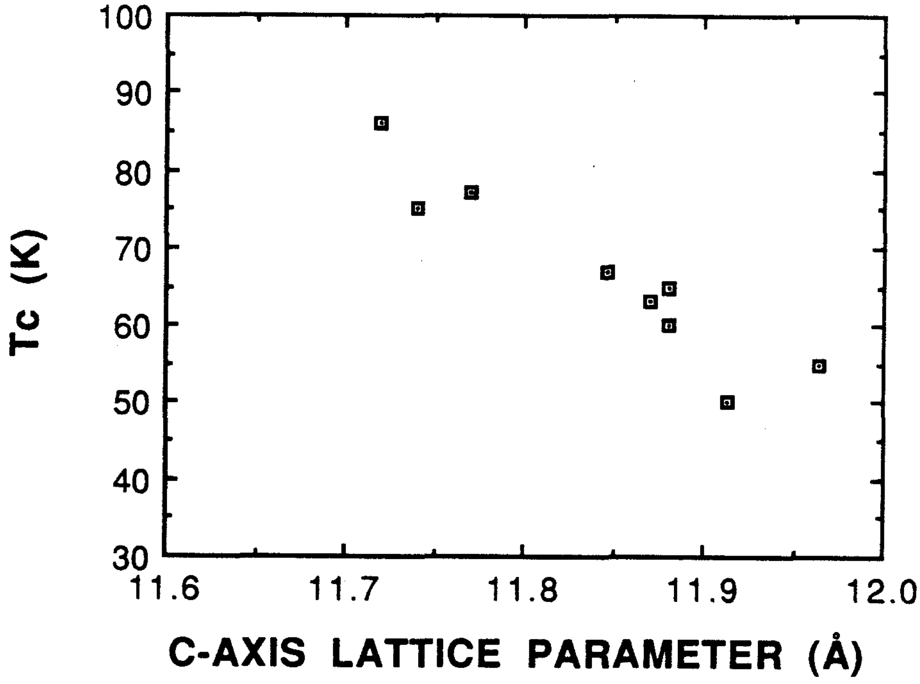

Fig. 37. Plot of the resistive superconducting transition temperature (midpoint) as a function of the c-axis lattice parameter.

A comparison of our results to those obtained for films grown by magnetron sputtering [Eom et al., 1989, 1990b], e-beam evaporation (stoichiometric films) [Matijasevic et al., 1991], and laser ablation [Roas et al., 1989; Gupta and Hussey, 1990, 1991], show that the relation between Tc and the c-axis lattice parameter, and the effects of anneals, are similar in different *in-situ* growth techniques. This suggests that films grown by these various techniques contain the same type of defects.

The resistivity data showed that films with large c-axis lattice parameters and high inhomogeneous strains had considerably broad transitions. The transition widths were best correlated to the inhomogeneous strains. Typically films with ϵ_{rms} of 0.15, 0.30 and 0.60% had transition widths of 5, 10 and 30 K respectively (Fig. 38). A relation between the broadening of diffraction lines and the broadening of superconducting transitions was proposed in perovskite superconductors [Cox and Sleight, 1976]. These broadenings have been attributed to fluctuations in the lattice parameter [Cox and Sleight, 1976], and to the proximity of phases with different oxygen ordering [Cox and Sleight, 1976; Cava et al., 1990].

These results suggest that the superconducting resistive transition midpoint and width are related to the fluctuations and mean value of the lattice distortions along the c-direction, which cause the *(00l)* x-ray peak broadening (other than the broadening due to finite film thickness) and shift.

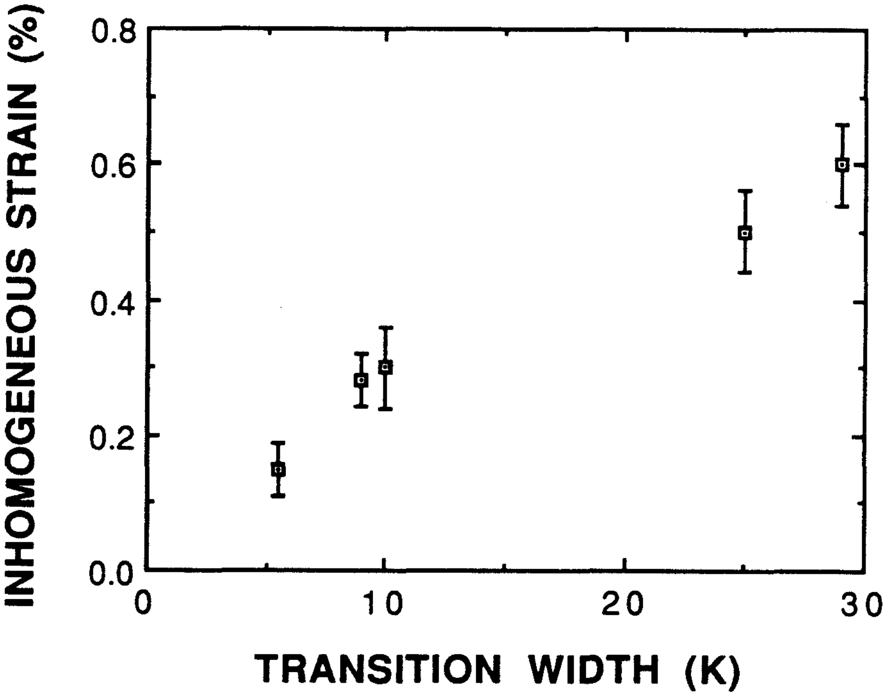

Fig. 38. Plot of inhomogeneous strains $\in_{rms}$, vs resistive superconducting transition widths.

4.6 Correlations Between Deposition Parameters and C-Axis Lattice Expansion

Understanding the nature of the c-axis lattice expansion and its dependence on deposition parameters is crucial for the successful control and optimization of the superconducting properties of *in situ* grown films.

We investigated the dependence of the c-axis lattice parameter on deposition parameters [Kittl et al., 1990b], finding that, under the conditions investigated, the growth temperature was the predominant factor in determining its value. Figure 39 shows a plot of the c-axis lattice parameter as a function of the temperature during growth, for a large number of films. The temperatures in Fig. 39 are those of the Cu plate on which the samples were clamped (the sample temperatures were ~ 100°C lower). We include films grown under different partial pressures of oxygen, and a few films grown off stoichiometry by as much as 20%.

These results show that, under the conditions investigated, there is a strong correlation between the growth temperature and the c-axis lattice parameter. The growth temperature is clearly the principal variable in determining the value of the c-axis lattice parameter, with other variables having only secondary effects. In the range investigated, the oxygen pressure during deposition did not have a strong effect on the value of the

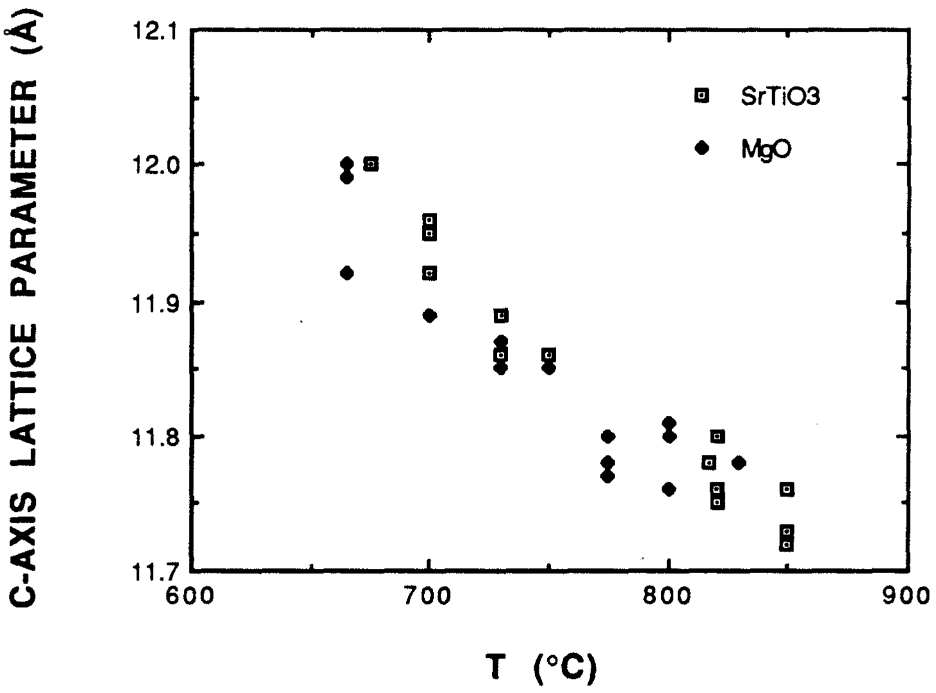

Fig. 39. Plot of c-axis lattice parameter vs temperature during growth. The temperatures are those of the Cu plate on which the samples were clamped.

c-axis lattice parameter; it is, however, constrained to be above a critical value corresponding to the boundary for phase separation.

In the plot of the c-axis lattice parameter vs. temperature, the data for films grown on MgO and on $SrTiO_3$ follow the same trend, suggesting that the expansion of the lattice parameter is not caused by the substrate. This is consistent with Off-axis x-ray diffraction studies in films grown by magnetron sputtering which rule out a substrate induced stress as the main cause of the c-axis lattice parameter expansion [Eom et al., 1989].

Reports on results obtained by other *in situ* deposition techniques indicate that, when the oxygen partial pressure for deposition is varied over orders of magnitude, it produces systematic expansions in the c-axis lattice parameter. This was shown for films grown *in situ* by laser ablation [Roas et al., 1989, Gupta and Hussey, 1991], magnetron sputtering [Matijasevic et al., 1991], and e-beam evaporation [Matijasevic et al., 1991]. These expanded c-lattice parameter films have the same overall characteristics than the ones grown by our technique. For films grown at the same temperature, the change in c-lattice parameter is in the order of 0.1 Å for a change in oxygen pressure of 1 order of magnitude (a factor of 10) [Roas et al., 1989]. These results suggest that the expansion of the c-lattice parameter is related to the incorporation of oxygen to the films during growth. The fluctuations on the data presented in Fig. 39 at a given temperature are consistent with a range of partial pressures of oxygen spanning one order of magnitude, corresponding to the one order of magnitude range in the background pressures of oxygen used for different depositions.

Several groups have investigated the effects of oxidizing agents other than molecular oxygen in the *in situ* growth of "123" films [Kwo et al., 1988b; Koren et al., 1989; Doyle et al., 1990]. The use of atomic oxygen was shown to allow the growth of films with near-bulk values of the c-lattice parameter (and high superconducting transition temperatures) at deposition temperatures of ~600°C [Terashima et al., 1988; Kwo et al., 1988b; Koren et al., 1989]. It was also shown that films with similar characteristics (high superconducting transition temperatures) to those obtained with atomic oxygen sources could be obtained with molecular oxygen using higher deposition temperatures [Koren et al., 1989]. The high growth temperatures needed in our work to obtain films with high superconducting transition temperatures is consistent with the fact that in the experiments done, the main oxidizing agent is molecular oxygen. The results mentioned above for deposition techniques that use atomic oxygen sources suggest that the temperature dependence of the c-lattice expansion found on our films is related to the kinetics of dissociation of molecular oxygen on the "123" film surface during growth.

We propose that the c-axis lattice expansion is a consequence of a kinetic limitation in the incorporation of oxygen to the films during growth [Kittl et al., 1991b]. The rate limiting step in the incorporation of oxygen to films grown under molecular oxygen is the dissociation of the oxygen molecule in the surface of the film. This process is thermally activated, and has an activation energy $E^* = 2.1$ eV for c-axis oriented films [Yamamoto et al., 1990]. We assume that in the region of expanded c-lattice parameters, the expansion of the c-lattice parameter is a function of the availability of atomic oxygen during growth

$$\Delta C \equiv C - C_o = F\,[P_{O_2} \times \exp(-E^* / k_b T)]\ , \tag{4.5.1}$$

for films grown with molecular oxygen, were C is the c-axis lattice parameter of the film after low temperature oxygen treatment, Co is the bulk c-lattice parameter (~11.68 Å), k_b is the Boltzman constant, T is the substrate temperature during growth, and P_{O_2} the local partial pressure of oxygen at the substrate during growth. For films grown at a fixed substrate temperature, ΔC has approximately a linear dependence on the logarithm of the oxygen pressure, in the region of expanded lattice parameters [Roas et al., 1989; Matijasevic et al., 1991], with

$$\Delta C \cong \alpha\ \log_{10}(P_{O_2}/P_o) + \text{constant}\ , \tag{4.5.2}$$

were P_o is a reference pressure, and α is approximately 0.1 Å. The additive constant may be different for different deposition techniques. Using this functional form in (4.5.1), the dependence of the c-lattice parameter on deposition parameters (oxygen pressure and temperature) can be calculated.

The dependence of ΔC on oxygen pressure given by (4.5.2), seems to hold roughly for deposition techniques in which activated oxygen species are present [Roas et al., 1989], and techniques in which only molecular oxygen is present [Matijasevic et al., 1991]. As long as the data for molecular oxygen corresponds to a fixed substrate temperature, the type of dependence on oxygen pressure, and the value of α should be similar for both cases. Since we assumed that the lattice expansion was due to kinetic constraints in the incorporation of oxygen, the additive constant in (4.5.2) may depend on the deposition rate, as is suggested by recent results [Gupta and Hussey, 1991].

In Fig. 40, we show a plot of our data on the temperature dependence of the c-lattice parameter, together with the dependence obtained using (4.5.1) and the functional form (4.5.2). This was calculated for two partial pressures of oxygen, differing by one order of magnitude, corresponding to the one order of magnitude range of oxygen pressures of the experimental data. The additive constant in (4.5.2) was chosen to fit the experimental data, and determines the vertical position of one of the lines. The slope and relative position of the lines are independent of this constant. The agreement between calculations and experiment is remarkable, and strongly indicates the kinetics of oxygen dissociation as determining the temperature dependence of the c-lattice parameter. This analysis can be used to determine the region in the oxygen pressure-temperature diagram in which films with expanded lattice parameters are grown (Fig. 41). The larger c-lattice parameters obtained in the

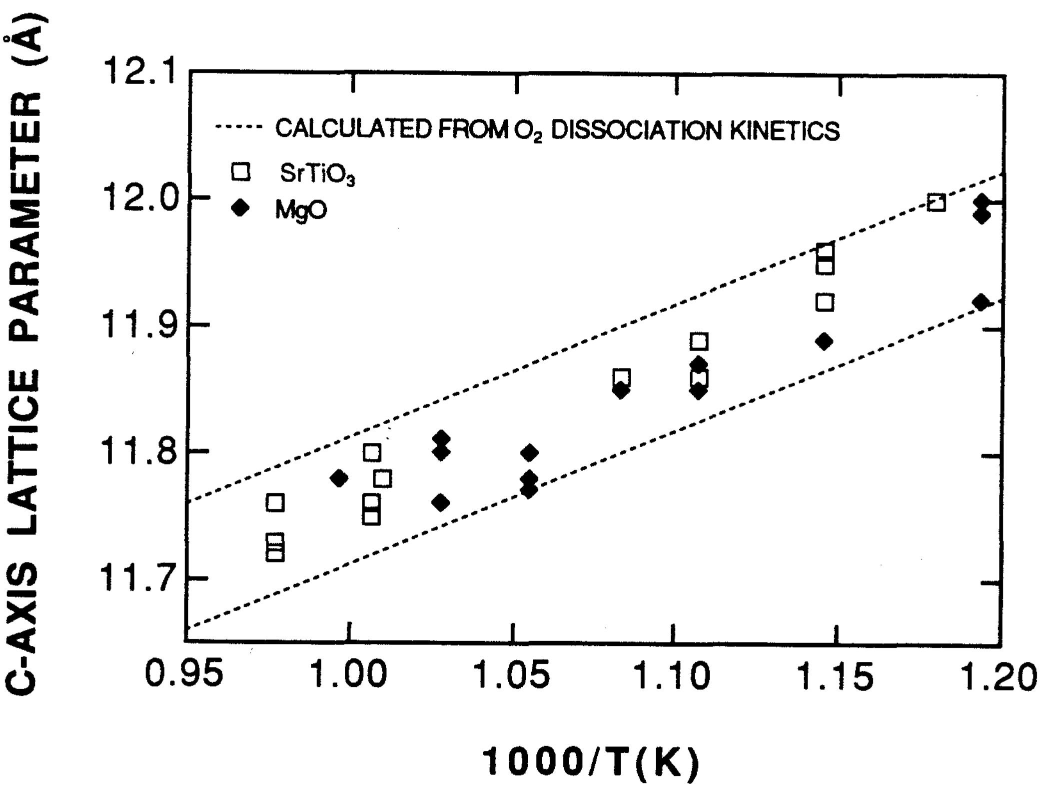

Fig. 40. Growth temperature dependence of the c-axis lattice parameter. The dotted lines correspond to calculations for two different oxygen pressures, based on the dissociation energy of O_2. The oxygen pressures differ from one line to the other by one order of magnitude.

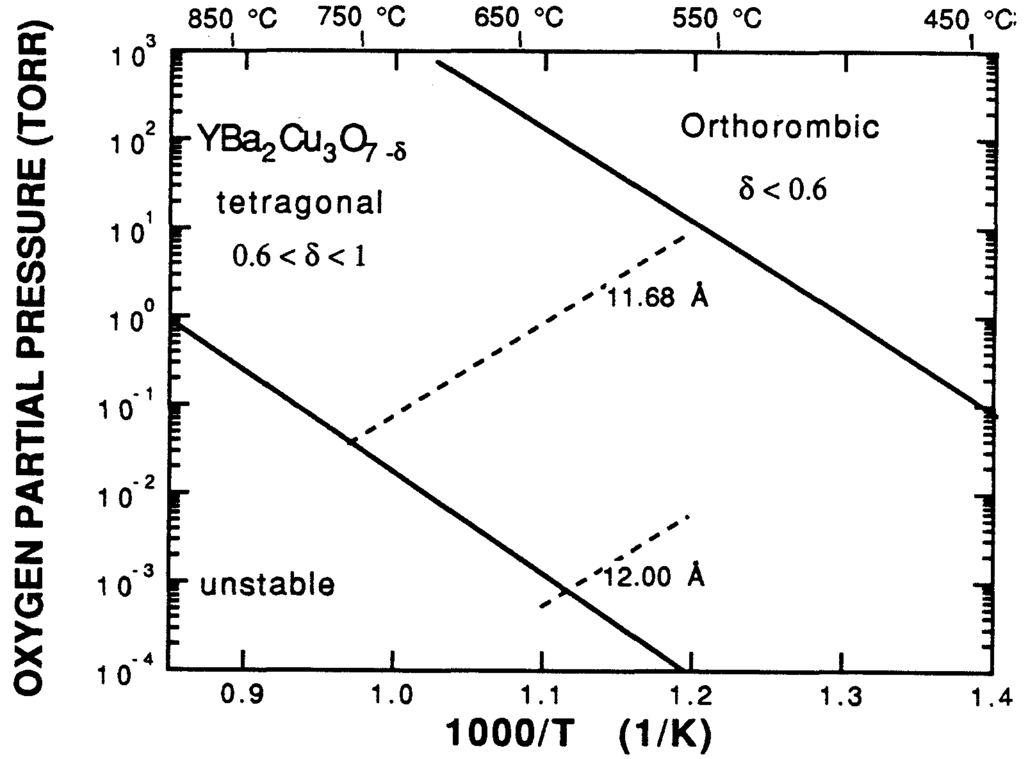

Fig. 41. Oxygen Pressure--Temperature phase diagram of $YBa_2Cu_3O_{7-\delta}$, showing the stability line [Beyers and Ahn, 1991] and the boundary between the orthorhombic and tetragonal phases [Jorgensen et al., 1990]. The dotted lines correspond to the deposition conditions for *in situ* growth of films with c-axis lattice parameters of 11.68 and 12.00 Å (measured at room temperature, after a low temperature oxygen anneal), calculated as described in the text.

experiments were ~12.00 Å, in films grown at ~560°C (sample holder temperature of 660°C, Fig. 39). Films grown at lower temperatures were amorphous. This could simply be a consequence of the kinetics of oxygen incorporation during growth. The growth of $YBa_2Cu_3O_{7-\delta}$ at lower temperatures was reported for techniques that provide a flux of excited oxygen species to the film during growth [Witanachchi et al., 1989].

4.7 Nature of the C-Axis Lattice Expansion

Although the expansion of the c-axis lattice parameter in *in situ* grown $YBa_2Cu_3O_{7-\delta}$ films is a well established phenomenon, there is still no unambiguous evidence of what is the defect structure that causes the expansion. The results presented in sections 4.5 and 4.6 suggest a relation between the oxygen availability during *in situ* growth of "123" films, the lattice expansion, and the degradation of Tc. The effect of anneals and the relation between the Tc and the c-axis lattice parameter in *in situ* grown films are different than in bulk samples [Jorgensen et al., 1990; Cava et al., 1990]. This indicates that the lattice expansion cannot be attributed to oxygen vacancies in the chain sites as in bulk samples, but may be due to other oxygen related defects. Another possible defect structure was proposed [Michikami et al., 1989] consisting of substitutional disorder between the Y and Ba sublattices. This type of defects, particularly Ba substitution on Y sites, could explain the c-lattice expansion and could be induced by low availability of oxygen during growth [Matijasevic et al., 1991]. Extended defects have to be considered as well. Stacking faults are common in high-Tc superconductors, and coherent precipitates are commonly found in *in situ* grown films.

The studies described in this section, required thicker films than the typical ones grown by sequential ion beam sputtering. For this reason, the studies were done on films grown *in situ* by magnetron sputtering from separate targets, at Hughes Research Laboratories [Nieh et al., 1991]. The films were grown on (001) $LaAlO_3$ substrates. The typical film thickness was ~3000 - 4000 Å. The films analyzed had expanded c-axis lattice parameters. As discussed in section 4.5, and considering the results presented in section 4.6, it is reasonable to assume that the same type of defects are present in expanded c-axis lattice parameter films grown by different *in situ* techniques, and that the cause of the c-lattice expansion in the different techniques is related to a low availability of oxygen during growth.

We investigated the oxygen content of films with different c-axis lattice parameters by Rutherford backscattering spectrometry. The Rutherford cross section for oxygen is low compared to that of other elements in the film and substrate, and the oxygen signal overlaps with the signal from the substrate. This results in a poor determination of the oxygen content of the films using conventional RBS. For this reason, we used a technique that enhances the sensitivity to oxygen, by taking advantage of the large resonant cross section of the ^{4}He - ^{16}O reaction at a ^{4}He incident energy of 3.05 MeV [Chu et al., 1978]. The ^{4}He incident beam energy was chosen so that the energy of the beam in the middle of the film (reduced by energy loss along the inward path) corresponded to the energy of the oxygen resonance. The relative oxygen content of several films was evaluated by comparing the ratios of the area of the oxygen resonance to the heights of the substrate signal (La) and the Ba signal. All the films were annealed in one atmosphere of oxygen for 1/2 hour at 450°C before the measurement. Several measurements were taken of each film, using different incident angles close to normal incidence. This allowed us to confirm that no channeling effects were present. The measurements were repeated in two areas for each film. The oxygen content of a film was compared to that on the same film after a high temperature oxygen anneal at 850°C followed by the low temperature 1/2 hour oxygen anneal. This allowed to compare the oxygen content of a film with an expanded c-axis lattice parameter to that of a film with near bulk value of the c-axis lattice parameter. The results obtained showed significant differences in the oxygen content of films with c-lattice constants of 11.66 Å and 12.00 Å. The oxygen content was lower in the film with the 12.00 Å c-lattice constant by 7 ± 2%. This is in qualitative agreement with the results that show that the c-axis lattice expansion is induced by low availability of oxygen during growth.

We also investigated the cation long range order by x-ray diffraction. In order to obtain the integrated intensities of the peaks of the (00*l*) series, rocking curve measurements were taken with a wide angle detector. To study the ordering in the Y and Ba sublattices, we compared the intensities of the direct diffractions ((003), (006), and (009)) to those of the superlattice diffractions ((002), (005), (007)). Preliminary measurements showed no evidence of chemical disorder in the Y-Ba sublattices, in films with expanded c-lattice parameters.

4.8 Conclusions

In conclusion, we have grown superconducting $YBa_2Cu_3O_{7-\delta}$ thin films *in situ* by sequential ion beam sputtering. We have investigated the correlations between the deposition parameters and the structural and electrical properties of the films. We found homogeneous and inhomogeneous lattice distortions along the c-direction, that affect the superconducting resistive transitions of the films. We investigated the dependence of these distortions on deposition parameters. We showed that an overall agreement of the results reported here and those obtained by other techniques can be obtained if one assumes that the c-axis lattice expansion is caused by kinetic limitations in the incorporation of oxygen to the films during growth. We investigated the microstructure and type of orientation relations found on films grown on $SrTiO_3$, MgO, and SiO_2/Si substrates. We found that the films grown on $SrTiO_3$ and MgO were epitaxial, c-axis oriented; and those grown on SiO_2/Si had a preferred c-axis orientation.

References

Adachi, H., K. Hirochi, K. Setsune, M. Kitabatake, and K. Wasa, Appl. Phys. Lett. **51**, 2263 (1987).

Balluffi, R.W., A. Brokman, and A.H. King, Acta Metall. **30**, 1453 (1982).

Bardeen, J., L.N. Cooper, and J.R. Schrieffer, Phys. Rev. **108**, 1175 (1957).

Behrisch, R. (ed), *Sputtering by Particle Bombardment* I, Topics in Applied Physics, (Springer-Verlag, Berlin, 1981).

Berdnorz, J.G. and K.A. Muller, Z. Phys. B **64**, 189 (1986).

Berkley, D.D., B.R. Johnson, N. Anand, K.M. Beauchamp, L.E. Conroy, A.M. Goldman, J. Maps, K. Mauersberger, M.L. Mecartney, J. Morton, M. Tuominen, and Y.J. Zhang, Appl. Phys. Lett. **53**, 1973 (1988).

Beyers, R. and B.T. Ahn, to be published in Annual Review of Mater. Sci. (1991).

Bishop, G.H. and B. Chalmers, Scripta Metall. **2**, 133 (1968).

Bormann, R. and J. Nolting, Appl. Phys. Lett. **54**, 2148 (1989).

Brown, R., V. Pendrick, D. Kalokitis, and B.H.T. Chai, Appl. Phys. Lett. **57**, 1351 (1990).

Cava, R.J., B. Batlogg, R.B. van Dover, and E.A. Rietman, Phys. Rev. Lett. **58**, 408 (1987a).

Cava, R.J., B. Batlogg, R.B. van Dover, D.W. Murphy, S. Sunshine, T. Siegrist, J.P. Remeika, E.A. Rietman, S. Zahurak, and G.P. Espinosa, Phys. Rev. Lett. **58**, 1676 (1987b).

Cava, R.J., A.W. Hewat, E.A. Hewat, B. Batlogg, M. Marezio, K.M. Rabe, J.J. Krajewski, W.F. Peck Jr. and L.W. Rupp Jr., Physica C **165**, 419 (1990).

Chang, C.C., X.D. Wu, A. Inam, D.M. Hwang, T. Venkatesan, P. Barboux, and J.M. Tarascon, Appl. Phys. Lett. **53**, 517 (1988).

Char, K., A.D. Kent, A. Kapitulnik, M.R. Beasley, and T.H. Geballe, Appl. Phys. Lett. **51**, 1370 (1987).

Chaudhari, P., R.H. Koch, R.B. Laibowitz, T.R. McGuire, and R.J. Gambino, Phys. Rev. Lett. **58**, 2684 (1987).

Chu, C.W., P.H. Hor, R.L. Meng, L. Gao, Z.J. Huang, and Y.Q. Wang, Phys. Rev. Lett. **58**, 405 (1987).

Chu, W-K, J.W. Mayer, M.A. Nicolet, *Backscattering Spectrometry*, (Academic Press, Orlando, Florida, 1978).

Clemens, B.M., C.W. Nieh, J.A. Kittl, W.L. Johnson, J.Y. Josefowicz, and A.T. Hunter, Appl. Phys. Lett. **53**, 1871 (1988).

Cox, D.E. and A.W. Sleight, in *Proceedings of the Conference on Neutron Scattering*, Volume 1 (National Technical Information Service, U.S. Department of Commerce, Springfield, Virginia, 1976), CONF-760601-P1, p. 45.

Dijkkamp, D., T. Venkatesan, X.D. Wu, S.A. Shaheen, N. Jisrawi, Y.H. Min-Lee, W.L. McLean, and M. Croft, Appl. Phys. Lett. **51**, 619 (1987).

Dimos, D., P. Chaudhari, J. Mannhart, and F. K. LeGoues, Phys. Rev. Lett. **61**, 219 (1988).

Dinger, T.R., T.K. Worthington, W.J. Gallagher, and P.L. Sandstrom, Phys. Rev. Lett. **58**, 2687 (1987).

Doherty, R.D., *Phase Transformations, Diffusive,* chapter 14 in *Physical Metallurgy* part II, edited by R.W. Cahn and P. Haasen, (Elsevier, Amsterdam, 1983).

Doyle, J.P., R.A. Roy, J.J. Cuomo, S.J. Whitehair, L. Mahoney and T.R. McGuire, in *High Tc Superconducting Thin Films: Processing, Characterization, and Applications,* edited by R.L. Stockbauer, S.V. Krishnaswamy, and R.L. Kurtz (American Institute of Physics, New York, 1990), AIP Conf. Proc. No. 200, p. 102.

Dregia, S.A., P. Wynblatt, and C.L. Bauer, in *Initial Stages of Epitaxial Growth,* edited by R. Hull, J. Murray Gibson, and David A. Smith (Materials Research Society, Pittsburgh, Pennsylvania, 1987), Materials Research Society Symposia Proceedings Vol. 94, p. 111.

Eliashberg, G.M., Zh. Eksperim. i Teor. Fiz. **38**, 966 (1960).

Eom, C.B., J.Z. Sun, K. Yamamoto, A.F. Marshall, K.E. Luther, T.H. Geballe, and S.S. Laderman, Appl. Phys. Lett. **55**, 595 (1989).

Eom, C.B., A.F. Marshall, S.S. Laderman, R.D. Jacowitz, and T.H. Geballe, Science **249**, 1549 (1990a).

Eom, C.B., J.Z. Sun, B. M. Lairson, S. K. Streiffer, A.F. Marshall, K. Yamamoto, S.M. Anlage, J.C. Bravman, T.H. Geballe, S.S. Laderman, R.C. Taber, and R.D. Jacowitz, Physica C **171**, 354 (1990b).

Fujita, J., T. Yoshitake, A. Kamijo, T. Satoh, and H. Igarashi, J. Appl. Phys. **64**, 1292 (1988).

Fujita, J., T. Tatsumi, T. Yoshitake, A. Kamijo, and H. Igarashi, Appl. Phys. Lett. **54**, 2364 (1989).

Geerk, J., G. Linker and O. Meyer, Materials Science Reports **4**, 193 (1989).

Ginzburg, V. L. and L.D. Landau, Zh. Eksperim. i Teor. Fiz. **20**, 1064 (1950).

Gleiter, H., *Microstructure*, chapter 10B in *Physical Metallurgy* part II, edited by R.W. Cahn and P. Haasen, (Elsevier, Amsterdam, 1983).

Gray, D.E., editor, *American Institute of Physics Handbook*, (McGraw Hill, New York, 1963).

Gross, R., P. Chaudhari, M. Kawasaki, M.B. Ketchen, and A. Gupta, Appl. Phys. Lett. **57**, 727 (1990).

Guarnieri, C.R., K.V. Ramanathan, D.S. Yee, J.J. Cuomo, J. Vac. Sci. and Technology A **6**, 2582 (1988).

Gupta, A., R. Jagannathan, E.I. Cooper, E.A. Giess, J.I. Landman, and B.W. Hussey, Appl. Phys. Lett. **52**, 2077 (1988).

Gupta, A., B.W. Hussey, A. Kussmaul, and A. Segmuller, Appl. Phys. Lett. **57**, 2365 (1990).

Gupta, A. and B.W. Hussey, to be published (1991).

Haasen, P., *Physical Metallurgy*, (Cambridge University Press, Cambridge, England, 1986).

Hammond, R.H., Physics Today **41** (1), S69 (1988).

Harper, J.M.E., M. Heiblum, J.L. Speidell, and J.J. Cuomo, J. Appl. Phys. 52, 4118 (1981).

Harper, J.M.E., J.J. Cuomo, and H.R. Kaufman, J. of Vac. Sci. and Technology **21**, 737 (1982).

Hellman, E.S., D.G. Schlom, A.F.Marshall, S.K.Streiffer, J.S.Harris, Jr., M.R. Beasley, J.C. Bravman, T.H.Geballe, J.N. Eckstein, and C. Webb, J. Mater. Res. **4**, 476 (1989).

Hilliard, J.E., in *Modulated Structures*, edited by J.M. Cowley, J.B. Cohen, M.B. Salamon, and B.J. Wuensch, AIP Conference Proceedings 53, p. 407 (American Institute of Physics, New York, 1979).

Hulm, J.K., C.K. Jones, R. Mazelsky, R.A. Hein, and J.W. Gibson, in *Proc. 9th Int. Conf. on Low Temp. Phys.*, edited by J.G. Daunt, D.O. Edwards, F.J. Milford, and M. Yaqub, p 600 (1965).

Hwang, D.M., T.S. Ravi, R. Ramesh, Siu Wai Chan, C.Y. Chen, L. Nazar, X.D. Wu, A. Inam, and T. Venkatesan, Appl. Phys. Lett. **57**, 1690 (1990).

Inam, A., C.T. Rogers, R. Ramesh, K. Remschnig, L. Farrow, D. Hart, T. Venkatesan, and B. Wilkens, Appl. Phys. Lett. **57**, 2484 (1990).

Jesser, W.A and J.H. van der Merwe, *The Prediction of Critical Misfit and Thickness in Epitaxy*, chapter 41 in *Dislocations in Solids*, edited by F.R.N. Nabarro, (Elsevier, Amsterdam, 1989).

Johnson, W.L., *Superconducting Materials*, chapter 27 in *Physical Metallurgy* part II, edited by R.W. Cahn and P. Haasen, (Elsevier, Amsterdam, 1983).

Johnston, D.C., H. Prakash, W.H. Zachariasen, and R. Viswanathan, Mater. Res. Bull. **8**, 777 (1973).

Jorgensen, J.D., M.A. Beno, D.G. Hinks, L. Soderholm, K.J. Volin, R.L. Hitterman, J.D. Grace, I.K. Schuller, C.U. Segre, K. Zhang, and M.S. Kleefisch, Phys. Rev. B **36**, 3608 (1987).

Jorgensen, J.D., B.W. Veal, A.P. Paulikas, L.J. Nowicki, G.W. Crabtree, H. Claus, and W.K. Kwok, Phys. Rev. B **41**, 1863 (1990).

Kaufman, H.R., *Technology of Ion Bombardment Ion Thrusters,* in *Advances in Electronics and Electron Physiscs,* Vol. **36**, edited by L. Marton, pp. 265-373 (Academic Press, New York, 1974).

Kaufman, H.R., J. Vac. Sci. and Technology **15**, 272 (1978).

Kaufman, H.R. and R.S. Robinson, AIAA J. **20**, 745 (1982a).

Kaufman, H.R., J.J. Cuomo, and J.M.E. Harper, J. of Vac. Sci. and Technology **21**, 725 (1982b).

Kaufman, H.R., *Fundamentals of Ion-Source Operation,* (Commonwealth Scientific Corporation, Alexandria, Virginia, 1984).

Kittl, J.A., C.W. Nieh, D.S. Lee, and W.L. Johnson, Mater. Lett. **9**, 336 (1990a).

Kittl, J.A., C.W. Nieh, D.S. Lee, and W.L. Johnson, Appl. Phys. Lett. **56**, 2468 (1990b).

Kittl, J.A., C.W. Nieh, and W.L. Johnson, to be published in J. Appl. Phys., (1991a).

Kittl, J.A., C.W. Nieh, and W.L. Johnson, to be published (1991b).

Klug, H.P. and L.E. Alexander, *X-Ray Diffraction Procedures,* (Wiley, New York, 1974).

Koren, G., A. Gupta, and R.J. Baseman, Appl. Phys. Lett. **54**, 1920 (1989).

Kurdjumov, G. and G. Sachs, Z. Phys. **64**, 325 (1930).

Kwo, J., M.Hong, R.M. Fleming, A.F. Hebard, M.L. Mandich, A.M. De Santolo, B.A. Davidson, P. Marsh, and N.D. Hobbins, Appl. Phys. Lett. **52**, 1625 (1988a).

Kwo, J., M.Hong, D.J. Trevor, R.M. Fleming, A.E. White, R.C. Farrow, A.R. Kortan, and K.T. Short, Appl. Phys. Lett. **53**, 2683 (1988b).

Levi, A.F.J., J.M. Vandenberg, C.E. Rice, A.P. Ramirez, K.W. Baldwin, M. Anzlowar, A.E. White, and K. Short, J. Cryst. Growth **91**, 386 (1988).

Li, H.C., G. Linker, F. Ratzel, R. Smithey, and J. Geerk, Appl. Phys. Lett. **52**, 1098 (1988).

Logan, M.A., The Bell System Technical Journal, 885 (May 1961).

Maissel, L., *Applications of Sputtering to the Deposition of Thin Films,* Chapter 4 in *Handbook of Thin Film Technology,* edited by L.I. Maissel and R. Glang, (Mc Graw Hill, New York, 1970).

Mankiewich, P.M., J.H. Scofield, W.L. Skocpol, R.E. Howard, A.H. Dayem, and E. Good, Appl. Phys. Lett. **51**, 1753 (1987).

Marshall, A.F., R.W. Barton, K. Char, A. Kapitulnik, B. Oh, R.H. Hammond, and S.S. Laderman, Phys. Rev. B **37**, 9353 (1988).

Matijasevic, V., P. Rosenthal, K. Shinohara, A.F. Marshall, R.H. Hammond, and M.R. Beasley, to be published in J. Mater. Res. **6**, 682 (1991).

McMillan, W.L. and J.M. Rowell, Phys. Rev. Lett. **14**, 108 (1965).

Michikami, O., M. Asahi and H. Asano, Jpn. J. Appl. Phys. **28**, L448 (1989).

Morse, P.M., *Thermal Physics,* (Benjamin, Reading, Massachusetts, 1969), p. 339.

Nieh, C.W., J.Y. Josefowicz, and A.T. Hunter, to be published, (1991).

Nishiyama, Z., Scient. Rep. Tohoku Univ. **23**, 638 (1934).

Oh, B., M. Naito, S. Arnason, P. Rosenthal, R. Barton, M.R. Beasley, T.H. Geballe, R.H. Hammond, and A. Kapitulnik, Appl. Phys. Lett. **51**, 852 (1987).

Onnes, H.K., Leiden Comm. 120b, 122b, and 124c, (1911).

Ramesh, R., C.C. Chang, T.S. Ravi, D.M. Hwang, A. Inam, X.X. Xi, Q. Li, X.D. Wu, and T. Venkatesan, Appl. Phys. Lett. **57**, 1065 (1990).

Ravi, T.S., D.M. Hwang, R. Ramesh, Siu Wai Chan, L. Nazar, C.Y. Chen, A. Inam, and T. Venkatesan, Phys. Rev. B **42**, 10141 (1990).

Roas, B., B. Hensel, G. Endres, L. Schultz, S. Klaumunzer, and G. Saemann-Ischenko, Physica C **162-164**, 135 (1989).

Schooley, J.J., W.R. Hosler, and M.L. Cohen, Phys. Rev. Lett. **12**, 474 (1964).

Schrieffer, J.R., *Theory of Superconductivity*, (Addison-Wesley, New York, 1964)

Sleight, A.W., J.L. Gillson, and P.E. Bierstedt, Solid State Commun. **17**, 27 (1975).

Tarascon, J.M., L.H. Green, W.R. McKinnon, G.W. Hull, and T.H. Geballe, Science **235**, 1373 (1987).

Terashima, T., K. Iijima, K. Yamamoto, Y. Bando, and H. Mazaki, Jpn. J. Appl. Phys. **27**, L91 (1988).

Thompson, C.V., J. Appl. Phys. **58**, 763 (1985).

Tinkham, M., *Introduction to Superconductivity*, (Mc Graw Hill, New York, 1975).

Triscone, J.M., M.G. Karkut, L. Antognazza, O. Brunner, and O. Fischer, Phys. Rev. Lett. **63**, 1016 (1989).

Uchida, S., H. Takagi, K. Kitazawa, and S. Tanaka, Jpn. J. Appl. Phys. **26**, L1 (1987).

Van der Merwe, J.H., Philos. Mag. A **45**, 145 (1982).

Wassermann, G., Arch. Eisenhuttenw. **16**, 647 (1933).

Wehner, G.K. and G.S. Anderson, *The Nature of Physical Sputtering,* Chapter 3 in *Handbook of Thin Film Technology,* edited by L.I. Maissel and R. Glang, (Mc Graw Hill, New York, 1970).

Webb, C., S-L. Weng, J.N. Eckstein, N. Missert, K. Char, D.G. Schlom, E.S. Hellman, M.R. Beasley, A. Kapitulnik, and J.S. Harris, Jr., Appl. Phys. Lett. **51**, 1191 (1987).

Witanachchi, S., H.S. Kwok, X.W. Wang, and D.T. Shaw, Appl. Phys. Lett. **53**, 234 (1988).

Witanachchi, S., S. Patel, H.S. Kwok, and D.T. Shaw, Appl. Phys. Lett. **54**, 578 (1989).

Wu, M.K., J.R. Ashburn, C.J. Torng, P.H. Hor, R.L. Meng, L. Gao, Z.J. Huang, Y.Q. Wang, and C.W. Chu, Phys. Rev. Lett. **58**, 908 (1987).

Yamamoto, K., B.M. Lairson, C.B. Eom, R.H. Hammond, J.C. Bravman, and T.H. Geballe, Appl. Phys. Lett. **57**, 1936 (1990).